Multiscale Biomechanical Modeling of Arterial Networks

By

Hamidreza Gharahi

A DISSERTATION

Submitted to
Michigan State University
in partial fulfillment of the requirements
for the degree of

Mechanical Engineering - Doctor of Philosophy

2019

ABSTRACT

MULTISCALE BIOMECHANICAL MODELING OF ARTERIAL NETWORKS

By

Hamidreza Gharahi

Cardiovascular diseases are the leading cause of death all around the world. With the expansion of our understanding in biomedical sciences, a variety of factors associated with the onset and progression of such diseases have been identified. In particular, mechanical stresses such as wall shear stress and circumferential stress have been proven to be primary factors for the mechanobilogy, and their homeostatic conditions are regarded as a bridge between biomechanics and cardiovascular biology. The study of vascular growth and remodeling (G&R) is a field that exploits computational modeling to study the changes in mechanical structure and function of blood vessels in response to altered stimuli. During the past decade, vascular G&R modeling has made significant contributions to the field of biomedical engineering through all areas of cardiovascular research. However, the previous modeling has mostly been devoted to arteries, and few studies developed vascular G&R models of the microvasculature. Additionally, other remaining tasks for the modeling include: 1) consolidation of different physical models and taking into account their interactions (e.g., fluid-solid-interactions, fluid-solid-growth) and multiscale levels in space and time and 2) realization of the modeling for the clinical practice.

To this end, we developed a novel computational framework that incorporates biofluid and biosolid mechanics of arterial networks in physiological conditions and expanded it to model different vascular adaptation processes. This framework integrated essential features from a constrained mixture model of G&R and blood circulation with an extension of Murray's law to construct a spatially multiscale vascular tree. We formulated the framework as a cost optimization problem where the design of the vasculature was governed by minimization of

the metabolic dissipation under mechanical equilibrium as a constraint. Subsequently, we presented two implementations of the model to study two multiscale problems: pulmonary arterial hypertension (PAH) and coronary flow regulation.

In the case of PAH, we used the framework to estimate the homeostatic characteristics of the arterial tree as well as their hemodynamics. The results showed good agreement with the available experimental data in the pulmonary arterial vasculature. Furthermore, we used Womersley's analytical solution combined with the theory of small-on-large in finite elasticity to simulate the pulsatile hemodynamics in the pulmonary arterial tree. This study lays the groundwork for further temporally multiscale studies of PAH where long-term G&R in the vasculature (days to weeks) are coupled with short-term hemodynamics (cardiac cycle) in a fluid-solid-growth modeling (FSG) framework.

In the case of coronary network, the baseline properties of two myocardial arterial trees distal to left anterior descending coronary artery were established using the presented method. Consequently, three different coronary flow regulation mechanisms (flow-induced, myogenic, and metabolic) were implemented using the constrained mixture models of small arteries and arterioles. The model was then calibrated against the experimental autoregulatory pressure-flow relations. Moreover, the prediction capability of the model was evaluated by simulations of exogenous adenosine infusion and inhibition of nitric oxide synthesis.

In closing, the developed framework exhibited great promise for applications in the study of vascular adaptations in physiological and pathophysiological conditions. Particularly, after the homeostatic baseline of an arterial tree is established, the kinetics of production and removal of constituents from stress-mediated G&R models can be used to simulate the short- and long-term evolution of vascular tissues in disease conditions. Furthermore, this research will set the cornerstone for much needed *in-silico* experiments on palliative or curative managements of vascular diseases.

To Maadar & Baba,
For their unconditional love and never-ending sacrifices.

ACKNOWLEDGMENTS

First and foremost, I would like to express my sincere gratitude to Professor Seungik Baek, my Ph.D. adviser and mentor, for his continuous support over the years. I have learned so much from Professor Baek because of his patience in discussions, his passion for solving difficult problems, and his integrity in conducting research.

I am also grateful to my committee members: Professor William Jackson, Professor Lik-Chuan Lee, and Professor Sara Roccabianca for serving on my committee and for their insightful recommendations.

Furthermore, I would like to acknowledge our collaborators from University of Michigan, Professor C. Alberto Figueroa and Dr. Vasilina Filonova, for their help during the last two years of my Ph.D studies. I am particularly thankful to Dr. Filonova for her help in conceptualizing and developing the computational model.

I would also like to acknowledge my colleagues, former and current students at Cardiovascular and Tissue Mechanics Laboratory: Dr. Byron Zambrano, Dr. Hailu Getachew, Zhenxiang Jiang, Josue Nataren, and others. Particularly, I am grateful to Dr. Byron Zambrano and Zhenxiang for their help during the years of my graduate studies.

Finally, I owe the greatest debt of gratitude to my family - my extended family, my in-laws, my parents, my brother, Alireza, and my wife, Atefeh - for their love and support throughout the years. My parents are my first teachers who taught me lessons in life and their selflessness has been always inspirational for me. Alireza is my very first scientific mentor and I keep learning from him everyday. And finally, Atefeh is my rock and her presence got me to the finish line.

TABLE OF CONTENTS

LIST OF TABLES

LIST OF FIGURES

Chapter 1

Introduction

1.1 Motivation

Cardiovascular diseases (CVDs) are the leading cause of death globally with an annual death rate of around 17.9 million [1] and they cost of almost $1 trillion in healthcare expenses [2]. Broadly, many CVDs are often characterized by chronic structural alterations, such as narrowing, thickening, and stiffening of the arteries. Consequently, the importance of vascular biomechanics in the progression of CVDs has been extensively studied over the last 50 years. Motivated by the biomechanical markers, vascular computational models have been employed as critical tools in enhancing our knowledge of the fundamental processes involved in the onset and progression of the disease.

An important advancement in such computational models was the introduction of a constrained mixture model of arterial growth and remodeling (G&R) [3]. The modeling framework of G&R, and its later extensions to include biochemomechanical [4] and fluid-solid-growth (FSG) models [5], provide a powerful tool to test various hypotheses in the cardiovascular disease research. The main focus of the previous applications of G&R has been

to study the vascular adaptations in large arteries. However, little attention has been paid to the modeling of G&R in arterial networks in the presence of hemodynamics. Since the formation and progression of many CVDs are traced to the initial malfunctions in the distal vasculature, there is a crucial need to expand the G&R framework to capture the multiscale arterial networks.

Motivated by this need, the ultimate goal of the current study is to provide a modeling framework that embeds the essential features of G&R coupled with the hemodynamics within an arterial network characterized by bifurcation rules (Fig 1.1). An accurate multiscale modeling of G&R requires the reconstruction of the arterial networks as well as mechanical considerations of individual vessels.

The cardiovascular system maintains a state of mechanical homeostasis in the physiological conditions. The concept of the mechanical homeostasis, via quantities such as stresses and/or strains, is essential in understanding the biomechanics of long-term responses (i.e., G&R). Alternatively, in the studies on the optimal design of vascular systems, initiated by Murray in 1926 [7], the *in-vivo* structure of an arterial tree has been attributed to a minimum energy dissipation hypothesis (i.e., Murray's law). Each of these theoretical ideas, G&R and Murray's law, may encapsulate inconsistent or even contradictory ramifications when compared to experimental observations. Therefore, there is a need to rigorously evaluate these concepts with respect to the available experimental data in the literature. We will briefly review the previous work on G&R and generalizations of Murray's law and highlight the shortcomings of the existing frameworks in Section 2.1.

In this dissertation, for the first time, a framework is presented that integrates features from G&R and Murray's law, and provides a theoretical model which can be used for multiscale modeling of arterial networks based on available experimental data. The presented framework can be further utilized for analysis of distal arterial structure where non-invasive assessment of the arteries is not readily available [8]. Moreover, a constrained mixture model

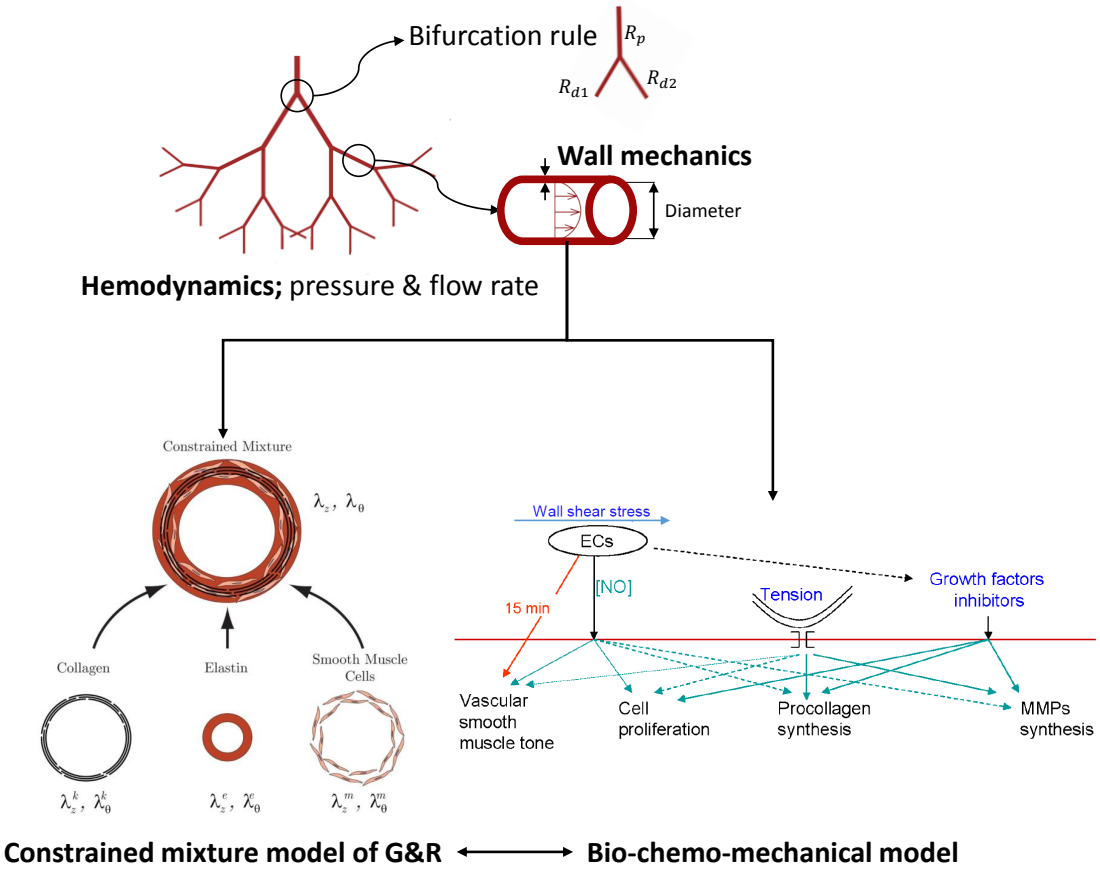

Figure 1.1: Schematic diagram of the modeling framework. The structure of the arterial tree is defined by a bifurcation rule. Every individual vessel is endowed with a constrained mixture model which is capable of extension to include the underlying biochemechanical processes of vascular adaptation. The insets are adapted from [5] and [6].

of the arterial segments facilitates the *in-silico* study of introducing therapeutic mediators into the vascular network. Therefore, we employ our model to study two prominently multiscale problems in cardiovascular research: pulmonary arterial hypertension and coronary flow regulation.

In the next sections of the introduction, we first review current literature on pulmonary arteries in normal and hypertensive states (Section 1.2.1). Next, a review of the existing publications on coronary arteries and their function in supplying blood to the myocardium is presented (Section 1.2.2). The structure of the dissertation and specific aims of this study are outlined at the of this chapter (Section 1.3).

1.2 Background

1.2.1 Pulmonary arterial hypertension

Pulmonary hypertension (PH) is a complex disorder associated with an elevated pulmonary arterial pressure (PAP). The prevalence of PH, which strikes women twice as frequently as men [9], is fairly rare with 15 incidents out of a million people [10]. Death rate of PH, however, have been steady and/or increasing between 1999 to 2008 with around 5.6 and 5.7 deaths per 100,000 population for men and women respectively [11]. Moreover, unlike the systemic hypertension, PH prognosis remains poor with >10% mortality within 1 year for for high risk patients [12]. In general, once PH patients are diagnosed, the progression of PH is not reversible. Primary PH patients are treated pharmacologically with vasodilators and inotropes [13]. The patient population is closely monitored using cardiac magnetic resonance imaging (CMR) and cardiac catheterization. Early detection of PH is however difficult because the standard diagnosis is based on using invasive catheterization, which might be already too late for clinical intervention.

In a healthy individual, the blood pressure in the pulmonary arteries is about 25/10 mmHg which is around six times less than that of the systemic arterial pressure. Based on clinical classifications, PH is present when the arterial pressure exceeds about 40/20 mmHg or the average pressure rises above 25 mmHg [14]. Pulmonary arterial hypertension (PAH), previously known as primary PH, is the first of the five PH groups according to the NICE clinical classification [15]. PAH includes idiopathic, heritable, drug-induced PH, or hypertension due to hypoxia in high altitude, in addition to other pathological conditions such as congenital heart disease. Moreover, PAH can be the cause to grave complications such as right-sided heart enlargement and heart failure (cor pulmonale), blood clots, arrhythmia, and bleeding. The usual cause of death in PAH is right ventricle (RV) failure [16] which is related to RV

hypertrophy due to chronic pressure overload where events during isovolumeic relaxation are disorganized [17]. Finally, right heart catheterization with the measurements of PAP, cardiac output (CO), and pulmonary arterial wedge pressure remain the gold standard for the diagnosis of PAH [14]. Besides the extreme invasiveness of this procedure, right heart catheterization yield possible risks and complications such as excessive bleeding due to vein puncture during catheter insertion, and infection.

1.2.1.1 Morphometry of pulmonary arteries

Pulmonary arteries enter the lung through the center of the lobe from the hilus and, accompanied by their paired airways (especially in smaller arteries [18]), navigate their way to the pleural surface [19]. The morphometry of the human pulmonary vasculature has been studied to provide more anatomical insight into the hemodynamics, geometry and branching of the pulmonary arterial tree. Singhal et al. [20] presented one of the earlier studies on the morphometric analysis of the human pulmonary vasculature. They used resin casts and injections of human vascular trees to measure the diameter, length, and order of all branches of blood vessels in the range of 13 μm to 3 cm for arterial vessels. They reported an arterial tree comprised of 17 branch orders with an estimated total number of 3×10^8 vessels of order one in Strahler's ordering system [21] with diameter of 13 μm. Moreover, they showed around a 60-fold increase in the total cross sectional area from the pulmonary trunk to the arteriolar level. Yen and Sobin [22] studied the elasticity and branching order of non-capillary pulmonary blood vessels of the size 1785 μm to less than 100 μm diameter. They observed a slight decrease in the compliance, expressed by percentage of change in diameter, of the arterioles as blood vessels become smaller. Using Strahler's ordering method, they observed that arteries of the same order (specifically between 4-8) have the same size (87 μm to 1785 μm), regardless of their location in the lung (upper, middle, or lower lobe).

Huang et al. [23] published an extensive study on the morphometry of the pulmonary arteries. They classified the pulmonary arterial network into 15 orders employing diameter-defined Strahler ordering system [24, 25]. Using silicone elastomer casting technique, they measured the diameter and length of the pulmonary arteries of two postmortem human subjects. They presented the connectivity matrix which expresses how blood vessels of one order are connected to vessels of another order. In this study, the diameters of order 1 have an average diameter of 20 μm increasing to an average of 1.4 cm (order 15). Several hemodynamic studies have used the work by Huang and colleagues as a baseline for generation of the downstream arterial tree [26, 27].

1.2.1.2 Structure of pulmonary arteries

The pulmonary arterial wall usually consists of three distinct layers of tunica intima, tunica media, and tunica adventitia. The intima is the innermost layer of the artery and consists of a layer of endothelial cells, a subendothelial layer of connective tissue, and the internal elastic lamina. The media, which is the middle layer, consists of concentrically arranged smooth muscle cells, collagen fibers and elastin. The adventitia, outermost layer, of pulmonary arteries is fairly disorganized [28] and is comprised of extra-cellular matrix (ECM), fibroblasts or other interstitial cells, nerves, elastin and collagen fiber bundles.

The composition of the vessel wall, however, significantly varies from the proximal pulmonary trunk to the smallest arterioles [28]. Hislop and Reid's [29] histological study on rats reported that the main pulmonary artery had a muscular media between internal and external elastic laminae with four concentric elastic lamina in between. However, while the medial structure of the left and right pulmonary arteries remained the same, fewer layers of elastic laminae were present relative to pulmonary trunk. The smaller the vessel in the pulmonary vasculature, the more media became clearly distinguishable by a single internal and external elastic

lamina. Moreover, in small distal pulmonary arteries, the internal elastic lamina started to fragment and eventually disappear which usually facilitates myo-endothelial communications [30]. As rat's arterial tree approached the alveolar level, the blood vessels became less muscular until the muscular coat was no longer seen in 80% of arteries larger than capillaries [29, 31]. Regardless, although muscular arteries in human adults extend as far as the alveolar level, below 1 mm diameter, arteries in rat and human are similar in structure, with the media having only internal and external elastic lamina [29].

Population based studies have shown the relationship between age and an elevated PAP [32]. The study of the pulmonary arterial wall with age can shed light on the structural basis of the arterial wall in PAH. Heath et al. [33] investigated the medial layer of the pulmonary trunk and aorta with age in human subjects. Figure 1.2 shows the evolution of the pulmonary trunk's medial layer against age for 71 human subjects without any cardiovascular disease.

Heath et al. [33] observed that the medial thickness and structural configuration the pulmonary trunk and the aorta are fairly similar for a fetal subject or a newborn. However, as humans age, the pulmonary trunk transitions to a more distinctive structure where elastic configuration is more open and loose. Furthermore, the medial thickness reduces between 40% and 70% that of aorta's medial thickness in 6 to 24 months. In adults' pulmonary trunk, the elastic laminae remained more irregular and sparser than the aorta.

MacKay et al. [34] studied the structural properties of the pulmonary vessels with age. Their results demonstrated that there was an almost steady decrease in the compliance of pulmonary artery with increasing age. The changes in the stiffness of the pulmonary arteries can be tracked qualitatively on histological images. Histology of a 7 year old male (Fig. 1.3-(a)) shows that the arterial elastin had nearly straight lamina. However, correspondingly to the histology images in [33], the structural configuration is different from that of aorta with more dispersed elastic fibers. Nevertheless, the elastic lamina becomes wavier and further apart (Fig. 1.3-(b)). In the older age, the elastic lamina continues to spread and be scant,

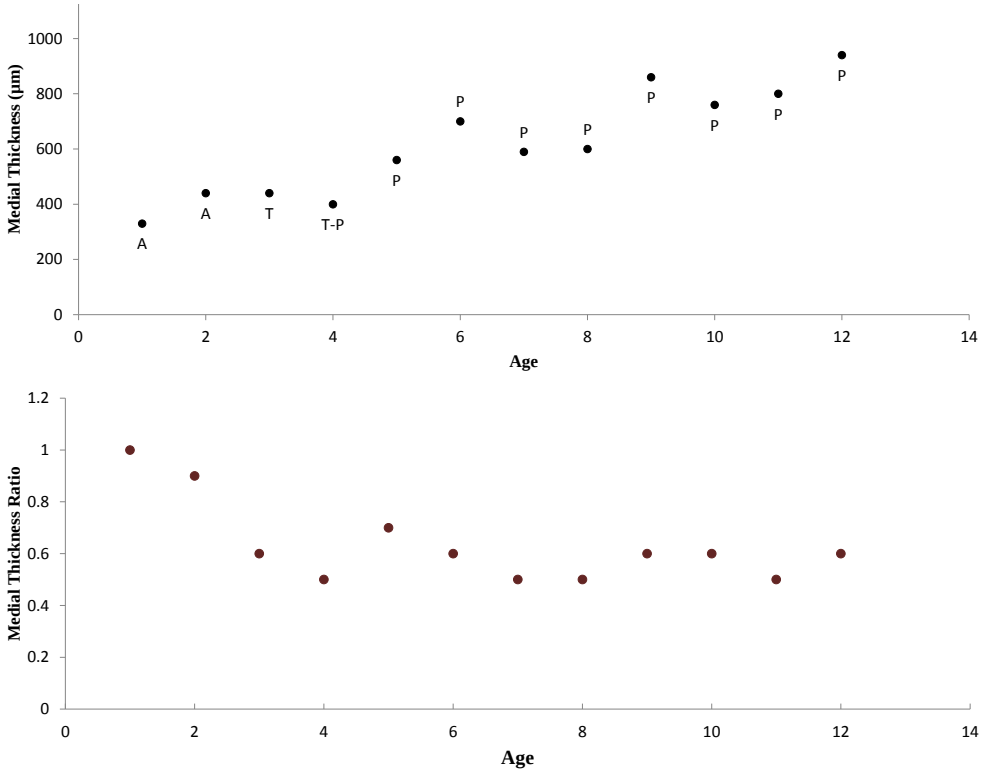

Figure 1.2: The medial thickness (above) and the ratio of pulmonary and aortic medial thickness (bottom) with age, reproduced from data available in [33]. The letters A, T, an P on the thickness plot represent the aortic, transitional, and pulmonary structural configuration of the trunk, respectively.

whereas the intima thickens and consists of a small amount of collagen fibrils.

While the elastic lamina serves the function of elastic recoil of the arterial wall, the adventitial network of collagen fibers prevents over-extension of the artery. To this point, MacKay et al. [34] studied 42 arterial specimens from humans aged 7 to 87 years, and showed a 1% per decade reduction in the amount of collagen as human get older.

1.2.1.3 Histopathology of PAH

PAH is associated with significant structural changes in the microstructure of the arteries. A study on 58 PAH patients [35] demonstrated some of the arterial histological abnormalities in PAH. While thrombotic lesions often a present pattern in PAH, complex plexiform

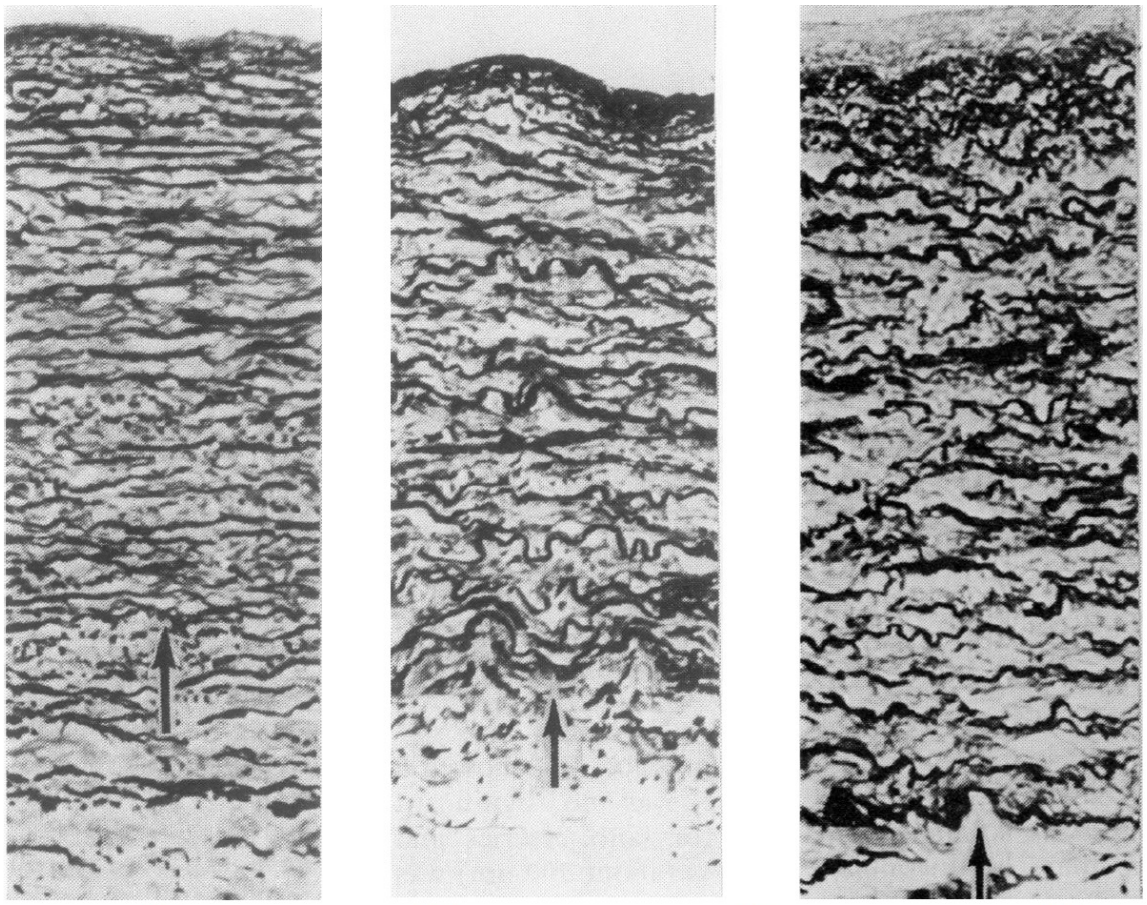

Figure 1.3: a) Male, 7 years old. b) Female, 47 years old. c) Male, 78 years old. Photographs at $\times 192$ magnification. Arrow heads show the limits of media and black area are elastin. Pictures adapted from [34].

lesions[1] and laminar intimal fibrosis were collectively present in almost half of the cases. Alternatively, laminar intimal fibrosis, while less common in PAH, leads unstable deposition and degradation of collagen and elastin [40].

Undoubtedly, several distinct histopathologic patterns of PAH exist. However, layer-wise remodeling seems to predominantly occur in diseased arteries. Chazova et al. [41] observed

[1]Plexiform lesions are one form of dilatation lesion which grow in the late stages of PAH [36]. They are usually associated with focal hypertrophy and proliferation of vascular smooth muscle, endothelial hyperplasia, and over-expression of matrix metalloproteinases (MMP) which lead to enzymatic degradation of ECM proteins [37–39].

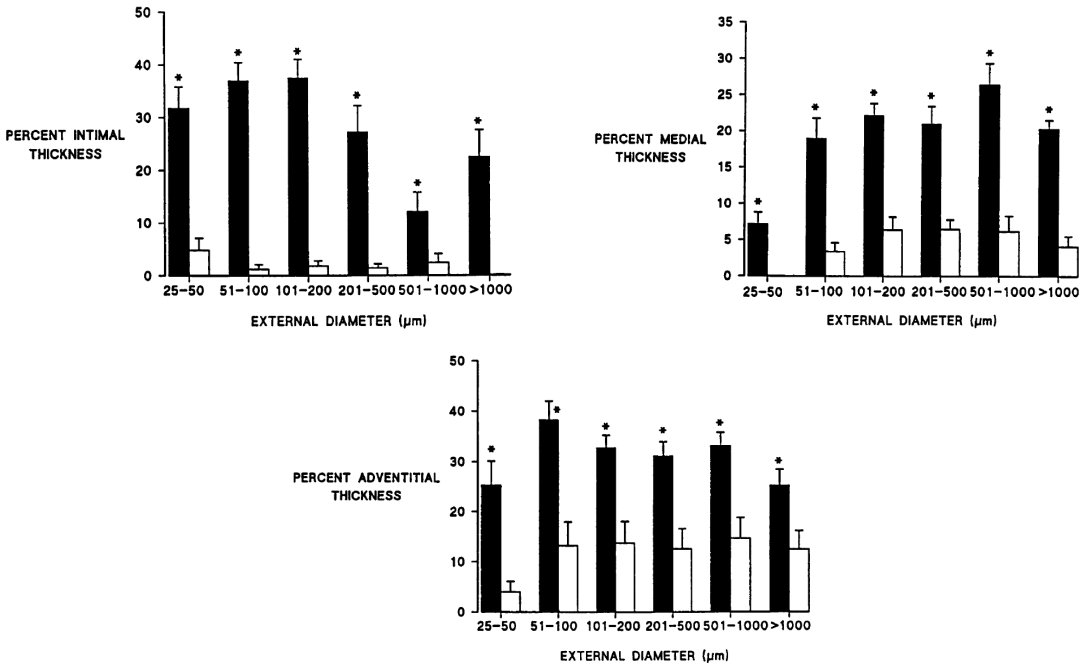

Figure 1.4: Intimal, medial, and adventitial thickness (percent of external diameter) of pulmonary arteries of vessels of various sizes. Solid bars represent PAH patients and open bars represent control subjects. Pictures adapted from [41].

that, in addition to intimal and medial thickening and remodeling, adventitial thickening and remodeling are consistent features of PAH vasculature (Fig. 1.4). Particularly, the increase in the adventitial thickness is attributed to the increased collagen deposition. Figure 1.5 reinforces this observation in hypoxia-induced PAH calves [42]. On the other hand, medial thickness is affected by smooth muscle cell hypertrophy that involves both muscular arteries (70-500 μm diameter) and smaller arterioles (smaller than 70 μm) [43].

The pulmonary vascular remodeling characteristics in PAH can be summarized as medial hypertrophy, intimal proliferation, arteriolar muscularization, and adventitial thickening [43, 44]. Nevertheless, the pathophysiology of PAH remains widely unclear [45, 46]. Although endothelial injury and excessive vasoconstriction which lead to a decrease in the internal diameter (i.e., increase in vascular resistance), seem to be important elements in pathogenesis of PAH [41,43,47,48], multiple studies hypothesized that increased elastolytic activity [37,49, 50] and collagen deposition [42,51] contribute to the pathogenesis of PAH through remodeling

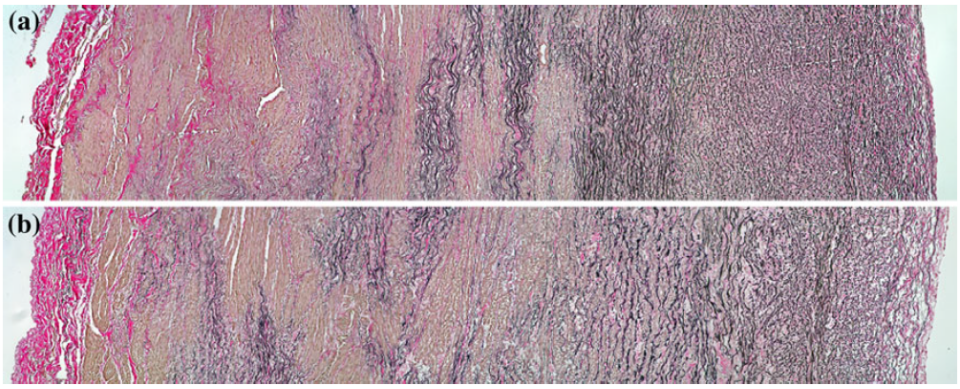

Figure 1.5: Optical microscopy images of pulmonary trunk (a) control and (b) hypertensive calves. Collagen and elastin appear red and black. Right to left direction is from intima to adventitia. Qualitatively, collagen deposition can be delineated in the adventitia. Additionally, fragmentation and dispersion of elastin is clear in the picture as the black areas of (a) are much more condensed and straight relative to (b). Pictures adapted from [42].

of the ECM (i.e., increased stiffness).

1.2.1.4 Significance of pulsatile hemodynamics

Although an elevated mean PAP is essential in diagnosis of PAH, the capability of mean PAP in prognosis of PAH has been relatively underperforming [52]. Animal models of PAH show that the distal vascular remodeling in PAH, results in "early return" of reflected pressure waves during RV contraction and consequently affects the RV systolic function [53]. Motivated by such analysis, several studies [54–56] have investigated the wave reflection in PA vasculature. Particularly, Hollander and colleagues [55] found a negative wave reflection in canine PA which facilitates the RV ejection in physiological condition. Quail and coworkers [56] observed congruent results in healthy human subjects. Conversely, they found that the increased stiffness, reduced vessel area, and persistent vasoconstiction created reflection sites with positive wave reflections which resulted in compressive reflections.

Furthermore, pulse pressure has been observed to act in concert with mean pressure and shear stress in modulating smooth muscle cells function [57]. Particularly, experimental studies of

cyclic stretch (∼10 Hz) applied to smooth muscle cells has shown increased collagen synthesis and decreased NO synthase expression which is a vasodilation mediator [58, 59]. Overall, a pathological pulse pressure may lead to increased collagen deposition, smooth muscle cells hypertrophy, endothelial dysfunction, etc. which result in stiffening, inflammation, and thickening of the blood vessels [60–66].

1.2.1.5 Modeling efforts

The significance of pulsatile hemodynamics in the pulmonary arterial networks compels multiscale computational modeling efforts to include the fluid-solid interactions (FSI) analysis. A significant portion of such efforts is focused on image-based 3D models coupled with Windkessel elements (0D) at the outlets [67]. Although such models are necessary for patient-specific studies, they cannot capture the salient features of the progression of PAH, for instance, proximal to distal wave propagation. Alternatively, full pulmonary arterial tree reconstructions can be used to model the pulmonary circulation [27, 68]. The main limitation of such simulations, however, is the computational cost which renders a fully detailed analysis impossible.

To circumvent limitations of the 3D computational modeling, one-dimensional (1D) models of the circulation have been developed and extensively used to study pressure and flow rate in different applications such as the whole systemic circulation [69], coronary arteries [70, 71], cerebral arteries [72], and pulmonary arteries [73–75]. An appropriate utilization of 1D hemodynamics theories in vascular networks, however, requires a physiologically realistic and complete tree morphometry of distal vasculature which is challenging due to data acquisition and modeling complexities. Therefore, studies by Olufsen and colleagues [73, 74] on pulmonary arterial networks have focused on the fractal structure of the arterial tree. The choice of a fractal structure, inspired by the airway structure [76], is particularly attractive since it provides a computationally inexpensive model of multiscale vascular networks.

Any 1D FSI modeling effort, however, has to be endowed with realistic estimation of size- and function-dependent mechanical properties of downstream vessels. Due to difficulties in measuring such properties of the vasculature in small blood vessels, there is a crucial need to utilize a unified framework that can facilitate the parameter estimation by exploiting all the available data.

1.2.2 Coronary flow regulation

Coronary artery disease (CAD) is the most common type of CVDs with causing more than 610,000 deaths annually in the United States [77]. CAD is primarily characterized by atherosclerosis in the epicardial coronary arteries which can lead to complications such as myocardial infarction. However, the prevalence of non-obstructive CAD has been reported to be up to 30% [78], where despite the absence of stenosis, patients experience adverse cardiovascular events [79]. Regardless, coronary microvascular abnormalities leading to ischemia and angina have been observed in both obstructive and non-obstructive CAD patients. Current clinical managements of CAD focus on the treatment of the atherosclerotic plaque in the major epicardial vessels [80], whereas myocardial blood is contingent on a range of factors in microvasculature besides the severity of the stenosis in major arteries. Therefore, one of the current challenges in treatment of CAD is understanding the functional significance of microvascular networks in myocardial perfusion. A crucial aspect of the research in CAD is a better understanding of the structure-function relations in the whole coronary circulation [81].

1.2.2.1 Anatomy, morphometry, and hemodynamics of coronary arteries

The coronary arteries are unique in that they are responsible for delivering oxygen and substrate, needed for oxidative myocyte metabolism, to the heart to supply the power required

for pumping the blood to the entire circulation system. Two main coronary arteries split from the aorta in the sinuses of Valsalva. The left main coronary artery is a short vessel that bifurcates into left anterior descending (LAD) and left circumflex (LCx) arteries. The LAD is mainly responsible for supplying the anterior side of left ventricle (LV) and left atrium (LA) and 2/3 of the septum [82]. Alternatively, the LCx courses horizontally around the heart and supplies the lateral side of the LV and LA. Right coronary artery (RCA) delivers blood the the RV and right atrium (RA) and the septum to a lesser extent [83]. These main vessels divide to conduit epicardial vessels over the surface of the heart into 17 regions after reaching a size of 1-3 mm [84]. During the course of these vessels, transmural branches at almost right angles penetrate the myocardium where they give rise to a network of vessels (i.e., myocardial vessels) which spread through the myocardium from subepicardial to subendocardial layers.

Morphometric analysis of swine coronary arteries has been extensively studied in the works of Kassab and colleagues [24, 25, 85–87]. They analyzed the main coronary branches separately, and showed 11, 11, and 10 orders of vessels (diameter-defined Strahler) for LAD, RCA, and LCx, respectively [24]. Specifically, the vessels in LAD network span from $\sim 3000\mu m$ to 9 μm. This data has been used extensively for hemodynamics analysis in the last two decades. We will present a summary of these contributions later in this chapter (Section 1.2.2.4).

The total flow in coronary arteries is directly proportional to coronary perfusion pressure and inversely proportional to the vascular resistance, which resides in blood vessels of smaller than $170\mu m$ [86]. However, a detailed description of the pulsatile nature of the coronary arterial hemodynamics (at rest) requires considerations of the other determinants such as vascular-myocardial interactions (extravascular compressive forces) and duration of diastolic time [88]. In this dissertation, we limit our analysis to the steady state hemodynamics in the coronary arteries. Instead, our study aims modeling the vascular adaptations in the coronary circulation which occur in a much larger timescale than that of a cardiac cycle (15

seconds-2 minutes) [89]. Henceforward, the coronary hemodynamics analysis in this study uses only to the average steady-state properties of blood flow.

1.2.2.2 Structure coronary artery

Similar to other arteries, coronary arteries are composed of three distinct layers including adventitia, media, and intima which consist of collagen fibers, elastin, and smooth muscle cells [90]. Chen and coworkers [91] showed that the ratio of collagen to elastin in the adventitial layer of LAD and RCA is 1.5 and 1.1, respectively, which is likely due to the size of the vessels and their different mechanical environment. However, medial layers of the coronary arteries are mechanically the most important layer at normal conditions. Most of the smooth muscle cells are concentrically arranged in the medial layer of the arterial wall within thick continuous sheets of elastin and collagen fibers [92]. It is worthy to mention that Chen et al. [93] observed that the alignment of smooth muscle cells are slightly deviated from the circumferential direction ($18.7^\circ \pm 10.9^\circ$). According to Zoumi et al. [92], the intimal layer of the coronary arteries in pigs is very thin and does not contribute to the mechanical properties of the arterial wall. In aged human coronary arteries, Holzapfel and coworkers [94] reported the relative thickness of adventitia, media, and intmia as 0.4, 0.36, and 0.27, respectively. Regardless, Most of the previous microstructural studies on coronary arteries were limited to the large epicardial vessels, while the mechanical structure of the coronary arteries and arterioles are major determinants of the severity of CAD and susceptibility of the patient to ischemia [95].

1.2.2.3 Physiology of coronary flow regulations

A normal functioning heart has a high metabolic demand and is rich in mitochondria which generate up to 90% of the energy needed for pumping blood via oxidative phosphorylation

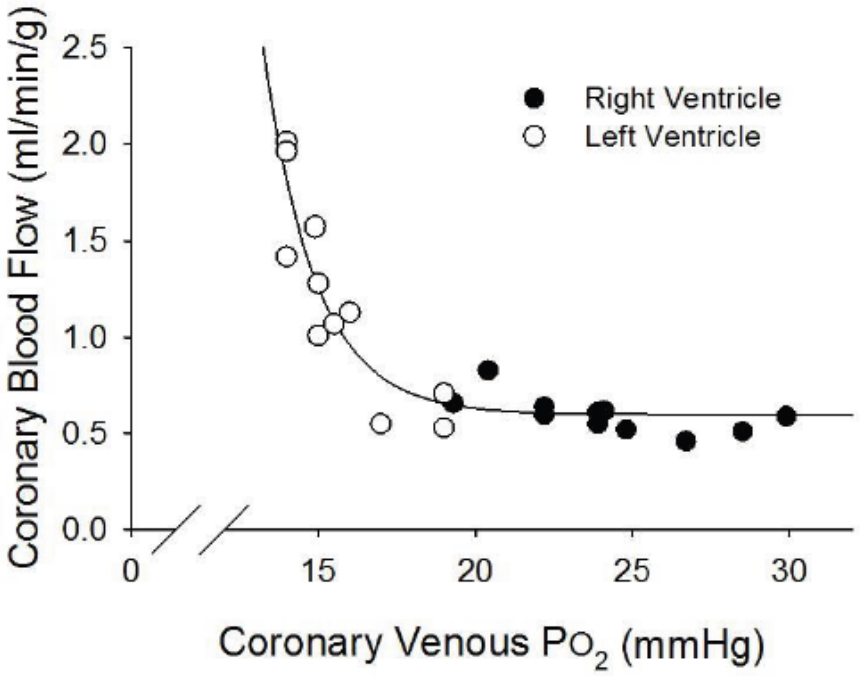

Figure 1.6: Normal relationship between coronary blood flow and coronary venous PO_2, which is an index of myocardial tissue oxygenation. Picture adapted from [82].

[96]. Because of this limited anaerobic capacity, any increase in cardiac activity (oxygen demand) is immediately met with an increase of available oxygen almost completely via an increase in blood flow [97].

An analysis of the oxygen demand in exercise shows that an augmented oxygen consumption rate (MVO_2) is in part the direct result of the heart beating faster. In addition, a rise in MVO_2 can be attributed to the elevation of contractility and ventricular work due to activation of the sympathetic signals [82,98]. Although, a precise delineation of each contribution is difficult, the relative role of the heart rate has been suggested to be between 40-60% [82,97]. On the oxygen supply side, the left ventricular oxygen extraction from arterial blood remains almost constant with 70-80% of the inflow of oxygen absorbed during rest and exercise [99]. This high level of utilization of oxygen extraction capacity by the myocardium necessitates the oxygen to be supplied by increased perfusion proportionally to MVO_2. Consistent with

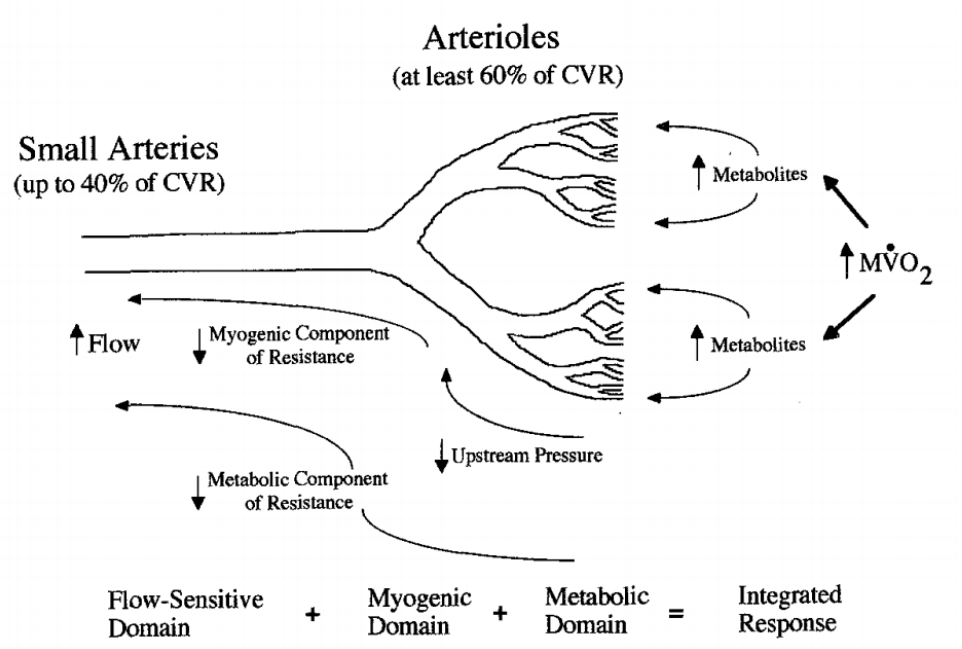

Figure 1.7: Schematic diagram of the heterogeneous regulatory response of vessels in response to pressure, shear-dependent, and metabolic mechanisms. Picture adapted from [104].

these observations, experiments on the coronary arterial responses to the changes in cardiac activity have shown 70% and 170% increases in the blood flow rate during pacing and exercise, respectively [82]. On the other hand, the right ventricular oxygen extraction is ∼45%, which means a moderate rise in MVO_2 is met with little increase in RCA flow and more contribution from oxygen extraction [100]. Figure 1.6 shows the coronary blood flow change in LV and RV. Henceforth, our analysis is focused on the coronary flow regulation in the LV.

To facilitate regulation of oxygen supply to myocytes, vasodilation (or vasoconstriction) occurs in the small artery and arteriolar level via extrinsic and intrinsic pathways [101]. Although a myriad of control mechanisms affect the coronary blood perfusion [81, 97], the primarily influential mechanisms are the metabolic, myogenic, and shear-dependent controls [102, 103]. Figure 1.7 shows the heterogeneous regulation of coronary vascular tone.

As a sympathetic response to an increase in MVO_2, β_1- and β_2-adrenergic receptors are stimulated eliciting a vasodilation in the arteries. Concurrently, at the onset of exercise (or stress)

α-adrenergic receptors on vascular smooth muscles are stimulated which result in a seemingly paradoxical vasoconstriction [105]. It is worthy to mention that in patients with coronary artery disease, blockade of α_1- and α_2-adrenoceptors has been proven beneficial for coronary blood flow and myocardial function [106]. Regardless, the net sympathetic stimulation in microvasculature is overridden by large β-adrenergic feedforward vasodilation. Furthermore, the feedforward metabolic regulation occur simultaneously with a feedback mechanism in which adenosine triphosphate (ATPs) and its metabolites[2] released from RBCs, act as vasodilators [107]. Specifically, as a response to desaturation of the oxyhemoglobin, ATP, ADP, and AMP activate purinergic receptors on capillary endothelial cells which initiate a conducted vasodilatory signal to the arterioles and small arteries ($<$150 μm) [81].

While the metabolic stimulus (i.e., increase in MVO_2) is essential in alteration of coronary perfusion, the flow rate is relatively unaffected by changes of arterial pressure in the range of 50-160 mmHg, demonstrating a significant autoregulatory response in myocardium [103]. Interestingly, this mechanism has been observed in other systemic circulations except for pulmonary circulation where the pressure and flow rate relation follows a monotonically increasing trend (Fig. 1.8).

Although the metabolic control is crucially effective in autoregulation, this mechanism is facilitated through an intrinsic myogenic tone in the vascular smooth muscle cells [109]. Briefly, studies have shown that increased transmural pressure leads to depolarization of smooth muscle cells and the opening of calcium channels responsible for increased intracellular calcium leading to the contraction of actin-myosin [110, 111]. The development and maintenance of a basal vascular tone via myogenic response is physiologically essential for vasodilators for regulation of blood flow and pressure [112]. Similar to the metabolic control, however, the myogenic tone varies in vessels with different diameter. The conduit coronary arteries do not exhibit a significant myogenic activity [81]. Unsurprisingly, the autoregula-

[2]adenosine diphosphate (ADP) and adenosine monophosphate (AMP).

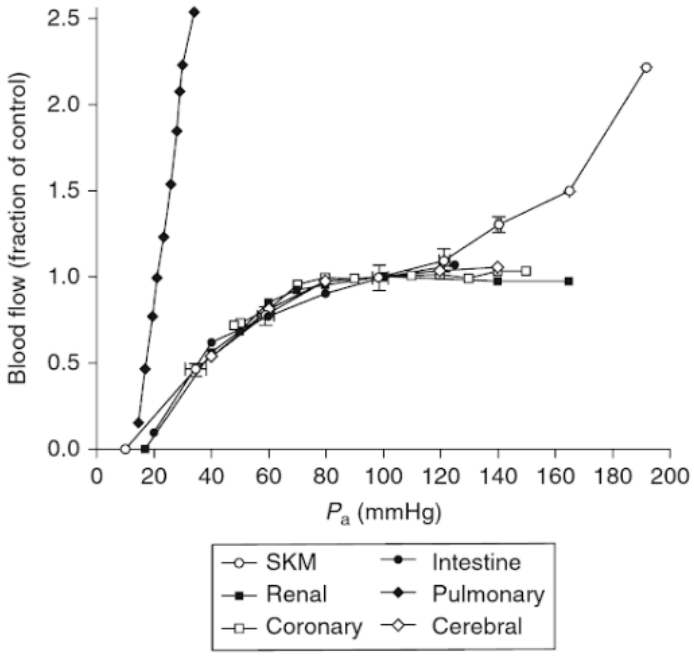

Figure 1.8: Whole organ pressure flow relationships. Picture adapted from [108].

tory response occurs primarily in the resistance vessels (<100-150 μm) [113, 114]. In addition, the myogenic activity of coronary arteries varies across the myocardium [103, 115, 116]. Kuo and colleagues [113] showed that at high pressure (70-100 mmHg) both subepicardial and subendocardial arterioles demonstrated myogenic activity, but subepicardial vessels exhibited greater constriction than subendocardial arterioles. In addition, Duncker and colleagues [115] determined that the lower autoregulatory pressure limit for subendocardial vessels (40 mmHg) is higher than that of subepicardial vessels (25 mmHg) indicating that vessels are maximally dilated for pressure below 40 mmHg and they are more prone to develop myocardial ischemia.

The third mechanism affecting the coronary blood flow is the wall shear stress dependent (i.e., shear- or flow-dependent) control. Shear-dependent dilation particularly has been observed in large coronary arteries from a variety of species [108]. This vasodilatory mechanism is the result of shear-induced production of the vasodilator NO by endothelial cells. The shear-dependent dilatory mechanisms in-vivo have been shown to be blunted in coronary micro-

circulation in comparison to conduit arteries [117, 118]. However, physical training has been shown to augment the shear-dependent vasodilation throughout the coronary circulation. In fact, studies on exercise-trained rats by Laughlin and colleagues [119, 120] have showed that this improved effectiveness is primarily a result of increased endothelial expression of nitric oxide synthase (NOS).

1.2.2.4 Modeling efforts

Arterial network studies - Since the direct measurements of the hemodynamics in the whole coronary network is difficult, data from morphometric studies has been used to construct the coronary arterial network for hemodynamics analysis. Beard and Bassingthwaighte [121] were the first to use an "avoidance" algorithm to present a three-dimensional model reconstruction of the LAD arterial network in an idealized model of the heart using statistical morphometric data. They used the reconstructed tree to analyze the fractal nature of spatial myocardial blood flow dispersion and temporal particle wash-out and were able to reproduce trends similar to experiments. Almost concurrently, Smith et al. [122] provided a similar algorithm that produced the network with the optimal bifurcating angles (based on [123]). However, due to computational limitations they were only able to generate a relatively smaller reconstructed network (largest six generations). Alternatively, Karch and coworkers [124] used a constrained constructive optimization method to generate the coronary arterial tree in a three-dimensional slab via successively adding new segments under a set of physiological constraints. Recently, Jaquet and colleagues [125] expanded this optimization to generate a patient specific coronary arterial network based on human cardiac CT image data. It is worthy to mention that two-dimensional network reconstruction attempts have been made using direct use of the statistical data [86].

Kaimovitz et al. [126, 127] provided a stochastic framework for modeling the entire coronary vasculature using a space-filling optimization process subject to morphological features

from [24]. These studies were later used as a basis for pulsatile hemodynamics analysis in the works of Algranati and colleagues [88] on the study of pulsatile hemodynamics of coronary vasculature coupled with vascular-myocardial interactions. Finally, Namani et al. [128] recently developed an algorithm to minimize the flow disparity in Kaimovitz's model of the coronary arterial network. They showed that a concurrent minimization of flow dispersion and diameter re-assignment in generation of coronary microvascular trees resulted in congruous results with the measured flow characteristics while following the measured morphometric data.

Flow regulation modeling - Flow and pressure regulation in the whole systemic circulation has been the subject of several studies over the last 50-60 years. The seminal works of Guyton and colleagues [129–131] used complex mathematical models, including several hundred equations, aiming to understand the regulation of blood pressure and cardiac output in closed-loop system. Alternatively, the mathematical models of local interaction between regulation mechanisms in microvasculature have been studied in different vasculature [109,132].

Coronary flow regulation has been under constant focus over the last 50 years [97]. However, important aspects of the coronary flow regulation and their diagnostic and prognostic capabilities remain greatly unknown [95]. Many such questions cannot be experimentally answered due to factors including failure to reach full dilation of vessels [133], difficulties in quantifying *in-vivo* hemodynamics [134], etc.

Previous studies have attempted to theoretically investigate the interaction and balance between the regulatory mechanisms in coronary circulation [102,135]. While these studies manage to incorporate the heterogeneity of the response into their model, the main limitations of their studies are crude classification of the arteries into 4 classes and ignoring the interactions of the vessels with the surrounding tissue. Alternatively, Pradhan et al. [99] presented a data-driven closed loop model of the coronary flow regulation which relied heavily on experimental data. Their model, however, only captures the total flow and pressure regulation

without any spatial information. More recently, Namani and colleagues [103, 116] revisited the computational modeling of coronary flow regulation and incorporated two networks of vessels in subendocardial and subepicardial layers of the cardiac wall. They reconstructed the arterial tree based on the morphometric data [24,126] and included the myocardial interactions in their model [88]. For the hemodynamic analysis, they used a 3-element Windkessel model which does not include the wave propagation and reflection in the arteries. Moreover, they used an empirical pressure-diameter relation to model the passive and active wall behavior.

1.3 Specific aims and organization of the dissertation

The specific aims of this dissertation are summarized as following:

Aim 1. To develop a computational framework of one-dimensional (1D) arterial network that captures essential features of vascular G&R and blood circulation using an extended Murray's law to establish the homeostatic baseline.

Aim 2. To construct a model of the pulmonary circulation.

1. Integrate the experimental data into the modeling framework to establish the homeostatic baseline of pulmonary arteries.
2. Apply the 1-D model for simulating the pulsatile hemodynamics and study the wave propagation phenomena in pulmonary circulation.

Aim 3. To develop a model of the coronary flow regulation.

1. Apply the modeling framework to construct the coronary arterial network with respect to the experimental data available in the literature.

2. Formulate and model coronary flow regulation mechanisms to understand their heterogeneous interactions and effectiveness.

The remainder of this dissertation is organized in the following manner: Chapter 2 presents a new computational framework of arterial network that generate and optimize 1D arterial geometry using an extended Murray's law and a constrained mixture model of arteries. Chapter 3 presents the application of the optimization on a pulmonary arterial tree to find the homeostatic characteristics of individual segments. Then, the result of application of a 1D theory to simulate the pulsatile hemodynamics in an arterial tree with physiologically realistic properties is presented. Chapter 4 presents the application of the optimization to the physiology of coronary arteries, specifically with regards to coronary flow regulation. The estimated basal arterial tree is endowed in flow regulation mechanisms to study the of vascular adaptation in the coronary arteries. Finally, Chapter 5 summarizes the simulation results and discusses about their significance, limitations, and future improvements.

Chapter 2

A Theoretical Framework for Estimating Homeostasis in Vascular Trees

2.1 Introduction

Theoretical studies on vascular G&R date back to the early 1980s [136, 137]. Theoretical and computational modeling of vascular G&R via constrained mixture models, however, only recently have been gaining attention. Originally proposed by seminal work of Humphrey and Rajagopal [3], several studies have adopted and developed G&R computational models to test multiple hypotheses based on experimental and clinical studies in applications such as aneurysms, cerebral vasospasm, and hypertension [138–141].

In essence, the G&R model includes constitutive relations for the mechanical response of the load bearing constituents and their time-varying masses. The latter accounts for the production and removal of cells and extracellular matrix during adaptation. The mediation

process of the adaptation is based on the existence of a mechanical homeostatic baseline, the deviation from which causes a change in the turnover rate or structure of each individual constituent.

In many applications of G&R modeling, the constituents of the arterial wall are specified to have individually prescribed mechanical behavior and homeostatic values. Vascular G&R models, therefore, have been developed to allow more insight into the component-wise mechanisms of G&R [4, 6, 142]. These models facilitate theoretical and numerical simulations of progressive collagenous stiffening, elastin damage/degradation, and flow- or pressure-induced vasoactive tone.

Previous extensive research of vascular adaptations has proposed mechanical homeostasis at multiple levels, tissue, cells, and subcellular structures that are mediated primarily by endothelial cells, vascular smooth muscle cells, and fibroblasts [142]. Therefore, processes of vascular adaptation have several intrinsic length and time scales. An iterative coupling of G&R and fluid-structure interaction (FSI), namely fluid-solid growth (FSG) modeling, has been proposed to deal with different time-scales in vascular adaptation using a linearization of the nonlinear behavior of the arterial wall over the cardiac cycle time scale [5, 143].

On the other hand, little attention has been paid to the spatially multiscale G&R applications in arterial adaptation. Particularly, while the principal concept of the stress-mediated G&R, as proposed by Humphrey and Rajagopal [3], is pivotal for predicting vascular adaptation and testing homeostatic hypotheses of individual constituents for the arteries, previous applications were limited to large arteries and the concept has not been extended to the whole arterial network. Furthermore, although not many experimental studies have reported circumferential stress and wall shear stress through the arterial network, it is not likely that the homeostatic values are constant. For instance, phenomenological studies on swine coronary arterial network [144, 145] evaluated the homeostatic stress and showed that the mean circumferential stress significantly reduces along the arterial tree. Similar trends have been

shown in the works of Pries and Secomb on rat's mesenteric microvasculature [146]. Therefore, an extension of the computational G&R framework to an arterial network requires a more general hypothesis for the whole arterial network that eventually takes account of meticulous considerations of the physiological data such as pressure, flow, thickness and radii.

As a matter of fact, the most successful theory to predict arterial network structure was based on metabolic energy consumption [7, 87, 147]. Based on the principle of minimum work, Murray [7] suggested the design of the blood vessels to be an optimization problem between the metabolic cost of maintaining the volume of blood and the power needed to overcome viscous forces. The optimization results in a cubic relationship between the diameter of a parent and its daughter vessels ($R_p^3 = R_{d_1}^3 + R_{d_2}^3$) which is called the Murray's law. Alternatively, studies by Zamir [123] and Kassab and Fung [85] have pursued the uniform shear hypothesis in the arterial networks. It is worthy to note that the uniform shear hypothesis is also an implication of Murray's work [85]. However, uniform shear hypothesis has has been challenged when it comes to microvasculature, similarly to the circumferential wall stress. While Kamiya et al. [148] observed a narrow variation in wall shear stress throughout the whole systemic circulation from the aorta to the precapillaries (1-2 Pa), other studies observed a 3- to 6-fold increase in wall shear stress from arteries ($>100\mu m$) to precapillary arterioles ($<100\mu m$) [118, 149].

Murray's law has been used extensively in studies for topology and reconstruction of *in-vivo* arterial network structures [27, 124, 125, 150]. Zhou and coworkers [87] proposed a generalized Murray's law for an entire coronary arterial tree and discovered new scaling laws that relate the diameter, length, and volume of the arterial tree. This generalization was later expanded to include the metabolic dissipation of wall constituents (e.g., active smooth muscle tone) in swine coronary arteries [147] and other vasculature [151]. These studies were able to successfully adapt the theoretical formulations, including the extension of Murray's

law, with the measured anatomical data and find the scaling laws. These scaling laws are particularly important for understanding the fractal nature and local hemodynamics of blood vessels in the homeostatic arterial tree. Murray's idea and its generalizations, however, were unable to provide information on the microstructure of the vessel wall. Inspired by the work of Taber [152], Lindström et al. [153] incorporated the conventional G&R into Murray's law as a unified modeling framework that studied vascular adaptation in a single vessel modeled using a constrained mixture model. Lastly, a study by Pries et al. [154] showed the influential role of metabolic responses in determining the wall shear stress and circumferential stress through the circulatory system.

Motivated by the incompleteness of our current understanding in the concept of homeostasis for arterial networks, the ultimate goal of this chapter is to establish a common framework for estimation of the homeostatic characteristics of the arterial trees. Inspired by the works of Pries et al. [154] and Lindström et al. [153], our framework constructs an arterial network that includes the essential features from G&R models with metabolic considerations (via an extended Murray's law approach). Moreover, the presented framework relies heavily on the reconciliation of available experimental data to predict pressure-flow relations in physiological conditions. Consequently, after we establish the homeostatic baseline, an application of the model to study multiscale adaptation of arterial networks will be unchallenging.

2.2 Methods

2.2.1 General workflow and initialization

By definition, mechanical homeostasis is the vascular adaptation of the arterial wall in the long term [155]. In other words, while a cardiac cycle typically is of the order of a second, the vessel wall adaptation takes place in a much slower time from a few minutes (in flow

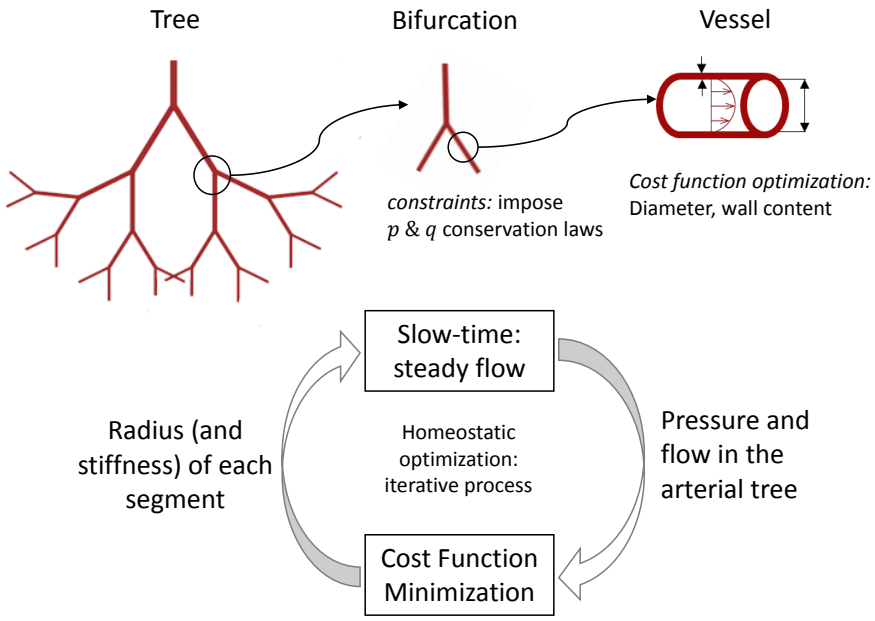

Figure 2.1: Information exchange for the homeostatic optimization applied for the tree in the nested manner: from the tree to bifurcation and then to individual vessels.

regulation) to weeks (in growth and remodeling). Therefore, the optimization process in this chapter must be considered in view of a slow-time scale. In a slow-time scale, the homeostatic condition of the artery is embedded into the strain energy function to describe the mechanical constitutive response and then incorporated into slow-time stress equilibrium, expressed via Laplace law (see Section 3.1 for more details on timescale considerations).

The general workflow of the presented model and its implementations begins from a construction of an initial arterial tree from bifurcation rules. Subsequently, an optimization procedure is applied to the tree which may alter initially defined diameters and bifurcation parameters. Finally, the optimization results are used in simulation of pulsatile hemodynamics (Chapter 3) and flow regulation (Chapter 4).

Arterial networks show characteristics of a fractal tree structure to some extent [156]. Inspired by this, we construct an initial self-similar arterial tree using bifurcation rules follow-

ing [69]. First, we assume a power law determines the radius change across a bifurcation

$$R_p^{\xi} = R_{d_1}^{\xi} + R_{d_2}^{\xi}, \tag{2.1}$$

where subscript p refers to the parent vessel, and subscripts d_1 and d_2 refer to the daughter vessels. To compute the radius of each vessel, we introduce two bifurcation parameters, area ratio (η) and asymmetry ratio (γ), defined as

$$\eta = \frac{R_{d_1}^2 + R_{d_2}^2}{R_p^2}, \quad \text{and} \quad \gamma = \frac{R_{d_1}^2}{R_{d_2}^2}, \tag{2.2}$$

where $\gamma = 1$ defines a symmetric tree. The parameters ξ, η, and γ are related by

$$\eta = \frac{1+\gamma}{(1+\gamma^{\xi/2})^{2/\xi}}. \tag{2.3}$$

Using these relations, we can define scaling parameters α and β as

$$\alpha = \frac{1}{(1+\gamma^{\xi/2})^{1/\xi}}, \quad \text{and} \quad \beta = \alpha\sqrt{\gamma}. \tag{2.4}$$

Finally, the radius of daughter vessels can be computed using the parent vessel using the scaling parameters as

$$R_{d_1} = \alpha R_p, \quad \text{and} \quad R_{d_2} = \beta R_p. \tag{2.5}$$

Equation 2.5 illustrate that the radii of vessels can be computed from their respective parent vessel. Therefore, if we specify a root radius R_0 and two bifurcation parameters (e.g., ξ and η), we can construct the whole arterial tree. Moreover, the length of each segment in the arterial tree must be specified. In each implementation of the model a length-diameter relation obtained from morphometric studies will be used (for more details see Chapters 3 and 4).

We present the homeostasis of an arterial tree as an optimization problem at individual vessel segments and then extend it to an entire arterial tree, which we call "homeostatic optimization" hereafter. The steady state hemodynamics and stress equilibrium are the constraints applied to the optimization problem. This framework will determine the optimal design of the arterial tree (i.e., changes the bifurcation rules above), hemodynamics (i.e., pressure-flow relations), and structure of arterial wall. Figure 2.1 shows schematic diagram of the homeostatic optimization from a tree outlook to individual vessels.

2.2.2 Arterial mechanics of a single segment

A single segment of the arterial tree is considered as a thin-walled cylindrical tube composed of three main load-bearing constituents: elastin, collagen, and smooth muscle cells. Each constituent is assumed to separately contribute to the strain energy density:

$$w = w^e + w^m + w^c \tag{2.6}$$

where subscripts e, m, and c represent elastin, smooth muscle, and collagen respectively. In addition, following Baek et al. [157], we assume distinct pre-stretch for each constituent mapping them from natural configuration to the overall loaded configuration. In particular, the pre-stretch mapping for elastin can be expressed as

$$\mathbf{G}^e = \begin{bmatrix} G_r^e & 0 & 0 \\ 0 & G_\theta^e & 0 \\ 0 & 0 & G_z^e \end{bmatrix} \tag{2.7}$$

where G_θ^e and G_z^e are pre-stretches associated with circumferential and axial directions, and $G_r^e = \frac{1}{G_\theta^e G_z^e}$.

Similarly, for collagen fibers and smooth muscle, $\mathbf{M}^i$, $i \in \{k, m\}$ is defined as the unit vector

in the direction of the collagen fiber (k) or smooth muscle cell. The pre-stretch mappings for collagen and smooth muscle cells are given as

$$\mathbf{G}^k = G_h^c \mathbf{M}^k \otimes \mathbf{M}^k, \quad \mathbf{G}^m = G_h^m \mathbf{M}^m \otimes \mathbf{M}^m. \tag{2.8}$$

where the pre-stretches G_h^c and G_h^m are identified as homeostatic stretches, which are the stretches of the constituents when they are produced [157]. We should note that in the previous applications of G&R, the pre-stretches were assumed to be constant. However, in our generalization of the framework to an arterial tree, we assume that the pre-stretches may vary across the arterial tree (for more details see Section 3.2.3). Nevertheless, the pre-stretch implies that the homeostatic state in an individual vessel is associated with a constant homeostatic stress for materials with a finite turnover in the vessel.

The orientation of collagen fibers and smooth muscles in their reference configuration, defined by angle γ^k, can be written as

$$\mathbf{M}^k = \cos\gamma^k \mathbf{e}_Z + \sin\gamma^k \mathbf{e}_\Theta, \quad \mathbf{M}^m = \mathbf{e}_\Theta. \tag{2.9}$$

For modeling and extension and inflation of a thin wall model, we consider a deformation gradient $\mathbf{F} = diag[\lambda_r, \lambda_\theta, \lambda_z]$. The incompressibility of the wall material is imposed by assuming an isochoric motion (i.e., $\det \mathbf{F} = 1$), therefore, $\lambda_r = \frac{1}{\lambda_\theta \lambda_z}$. Using membrane theory [158], the membrane Cauchy stress (force per deformed length) can be written as

$$\mathbf{T} = \frac{1}{J_{2D}} \mathbf{F} \frac{\partial w}{\partial \mathbf{F}^T}, \quad \Rightarrow \quad T_{\theta\theta} = \frac{1}{\lambda_z} \frac{\partial w}{\partial \lambda_\theta}, \quad \text{and} \quad T_{zz} = \frac{1}{\lambda_\theta} \frac{\partial w}{\partial \lambda_z}, \tag{2.10}$$

where $J_{2D} = \lambda_\theta \lambda_z$. The following strain energy density functions for the three materials are used as constitutive relations [159]

$$\Psi^e = \frac{c_1}{2}\Big((\lambda_\theta^e)^2 + (\lambda_z^e)^2 + \frac{1}{(\lambda_\theta^e)^2(\lambda_z^e)^2} - 3\Big), \tag{2.11}$$

$$\Psi^k = \frac{c_2}{4c_3}\Big(\exp\Big(c_3\big((\lambda^k)^2 - 1\big)^2\Big) - 1\Big), \tag{2.12}$$

$$\Psi^m = \frac{c_4}{4c_5}\Big(\exp\Big(c_5\big((\lambda^m)^2 - 1\big)^2\Big) - 1\Big). \tag{2.13}$$

The total strain energy per unit area can be written as

$$w = M_R^e \Psi^e + \sum_k M_R^k \Psi^k + M_R^m \Psi^m, \tag{2.14}$$

where M_R^i, $i \in \{e, k, m\}$ is the mass of each constituent per unit reference area. Moreover, λ^i, $i \in \{e, k, m\}$ is the stretch in each constituent, and can be expressed in terms of the pre-stretches using $\mathbf{F}^i = \mathbf{F}\mathbf{G}^i$

$$\lambda_\theta^e = G_\theta^e \lambda_\theta, \quad \lambda_z^e = G_z^e \lambda_z \quad \lambda^k = G_h^c \sqrt{\lambda_\theta^2 \sin^2\gamma^k + \lambda_z^2 \cos^2\gamma^k}, \quad \lambda^m = G_h^m \lambda_\theta \tag{2.15}$$

Therefore, the circumferential membrane Cauchy stress can be written as

$$T_{\theta\theta} = \frac{1}{\lambda_z}\Big(M_R^e \frac{\partial \Psi^e}{\partial \lambda_\theta} + \sum_k M_R^k \frac{\partial \Psi^k}{\partial \lambda_\theta} + M_R^m \frac{\partial \Psi^m}{\partial \lambda_\theta}\Big). \tag{2.16}$$

Substituting 2.15 into 2.16, and using chain rule, we can write

$$T_{\theta\theta} = \frac{1}{\lambda_z}\Big(M_R^e \frac{\partial \Psi^e}{\partial \lambda_\theta^e}\frac{d\lambda_\theta^e}{d\lambda_\theta} + \sum_k M_R^k \frac{d\Psi^k}{d(\lambda^k)^2}\frac{d(\lambda^k)^2}{d\lambda_\theta^2}\frac{d\lambda_\theta^2}{d\lambda_\theta} + M_R^m \frac{d\Psi^m}{d(\lambda^m)^2}\frac{d(\lambda^m)^2}{d\lambda_\theta^2}\frac{d\lambda_\theta^2}{d\lambda_\theta}\Big) \tag{2.17}$$

Equation above shows the passive tension response of the artery. To include the active tone of vascular smooth muscle, we use a potential function as given by [160]

$$\Psi^m_{act} = \frac{S}{\rho}\Big(\lambda_\theta + \frac{1}{3}\frac{(\lambda_M - \tilde{\lambda})^3}{(\lambda_M - \lambda_0)^2}\Big), \tag{2.18}$$

where λ_M and λ_0 are stretches at which the active force generation is maximum and zero, respectively, and S is the stress at the maximum contraction. Note that S is generally a function of wall shear stress, internal pressure, and metabolites but in a short time scale of a cardiac cycle the value of S is considered as constant (e.g., Chapter 3). In addition, $\tilde{\lambda}$ is an active stretch of the SMCs in the circumferential direction. Although the vasoactive response can change via remodeling of the SMCs, the current formulation is applied for the homeostatic states of the arteries. In the application of the model in next chapters, we consider only the homeostatic baseline, in contrast to those of the long-term adaptations (days to weeks) of the arteries. Therefore, we assume $\tilde{\lambda} = \lambda_\theta$. Finally, the total tension in the artery can be written as

$$T_{\theta\theta} = \underbrace{\frac{1}{\lambda_z} M^e_R \frac{d\Psi^e}{d\lambda^e_\theta}\frac{d\lambda^e_\theta}{d\lambda_\theta}}_{T^e_{\theta\theta}} + \sum_k \underbrace{\frac{1}{\lambda_z} M^k_R \frac{d\Psi^k}{d(\lambda^k)^2}\frac{d(\lambda^k)^2}{d\lambda^2_\theta}\frac{d\lambda^2_\theta}{d\lambda_\theta}}_{T^k_{\theta\theta}} + \underbrace{\frac{1}{\lambda_z}\Big(M^m_R \frac{d\Psi^m}{d(\lambda^m)^2}\frac{d(\lambda^m)^2}{d\lambda^2_\theta}\frac{d\lambda^2_\theta}{d\lambda_\theta} + M^m_R \frac{d\Psi^m_{act}}{d\lambda_\theta}\Big)}_{T^m_{\theta\theta}} \tag{2.19}$$

where $T^i_{\theta\theta}$, $i \in \{e, c, m\}$ is the tension in each constituent. Finally, for an inflated thin wall cylinder with pressure p^s, the force equilibrium in the circumferential direction gives

$$p^s R = T_{\theta\theta}, \tag{2.20}$$

where R is the deformed radius of the cylinder.

2.2.3 Metabolic cost of a single segment

As proposed by Murray [7] and later extended by [152] and [153], the blood vessel wall composition and geometry strive to optimize the energy cost that includes the metabolic cost of blood supply, power needed to overcome resistance, and the cost of maintaining the vessel wall materials. We assume that homeostatic state is governed by such an optimization rule that can be defined for each individual vessel separately.

We define three contribution terms for the extended Murray's law. First, the metabolic cost of arterial wall constituents per unit length is assumed to be

$$C_{wall} = (2\pi R/\rho_{solid}) \sum_i \vartheta^i M_R^i, \tag{2.21}$$

where M_R^i is mass per unit reference area of each constituent (as in the previous section); ϑ^i is the metabolic cost of constituent i per unit volume; and R is the vessel radius in homeostatic condition. Note that the metabolic cost of smooth muscle cells (SMC; $i = m$), ϑ^m, includes both the metabolic cost of maintenance ϑ^m_{maint} and active tension ϑ^m_{act}. Second, the metabolic power needed for blood supply is proportional to ϑ^b and the blood volume that needs to be sustained; hence, this metabolic power per unit length is

$$C_{blood} = \vartheta^b \pi R^2. \tag{2.22}$$

Third, the power per unit length needed to overcome the resistance of Poiseuille flow (viscous drag forces) is

$$C_{drag} = \frac{8\mu q^{s2}}{\pi \rho_{fluid} R^4}, \tag{2.23}$$

with average volumetric flow rate q^s. Thus, the total energy cost per unit length at individual

blood vessel is summarized as

$$\begin{aligned} C(M_R^i, R) &= C_{wall} + C_{blood} + C_{drag} \\ &= \big(\frac{2\pi}{\rho}\sum_i \vartheta^i M_R^i\big)R + \vartheta^b \pi R^2 + \frac{8\mu q^{s2}}{\pi \rho_{fluid} R^4}. \end{aligned} \tag{2.24}$$

Using the minimum metabolic energy principle, Eq. (2.24) is minimized subject to the constraint of the mechanical equilibrium (Eq. 2.20).

2.2.4 Cost optimization of a single segment in terms of radius

Next we incorporate mass content to the cost function to express minimization in terms of radius. To this aim, we define total mass as M_R^t and mass fractions of elastin, smooth muscle, and collagen as

$$\nu^e = \frac{M_R^e}{M_R^t}, \quad \nu^k = \frac{M_R^k}{M_R^t}, \quad \text{and} \quad \nu^m = \frac{M_R^m}{M_R^t}. \tag{2.25}$$

Introducing Eq. 2.25 into 2.19 gives

$$T_{\theta\theta} = \frac{M_R^t}{(1-\phi_f)\rho\lambda_\theta\lambda_z}\big(\sum_i \nu^i \sigma_{\theta\theta}^i\big), \tag{2.26}$$

where $\sigma_{\theta\theta}^i$ is acting part of the tensor $\boldsymbol{\sigma}^i$ in circumferential direction, defined as

$$\boldsymbol{\sigma}^i = \frac{1}{h^i}\mathbf{T}^i, \quad h^i = \frac{M_R^i}{(1-\phi_f)\rho_{solid}\lambda_\theta\lambda_z}, \quad i \in \{e, k, m\}. \tag{2.27}$$

The parameter ϕ^f is the volume fraction of the interstitial fluid. Then the minimization problem (Eq. 2.24) is constrained by stress equilibrium relation (Eq. 2.20) with membrane

stress component expressed in terms of $\sigma_{\theta\theta}$

$$p^s R = \frac{M_R^t}{(1-\phi)\rho_{solid}} \sum_i \nu^i \sigma_{\theta\theta}^i. \tag{2.28}$$

Rearranging Eq. 2.28 for M_R^t gives

$$M_R^t = \frac{(1-\phi_f)\rho_{solid} p^s R}{\sum_i \nu^i \sigma_{\theta\theta}^i}. \tag{2.29}$$

The metabolic cost for elastin can be neglected for adult subjects, $\vartheta^e = 0$, since it is mostly produced in early ages and owing to a long half-life, remains relatively constant over time. Finally, for a single vessel the metabolic cost function (Eq. 2.24), embedding stress equilibrium constraint 2.28, can be written in terms of radius for a given steady-state flow q^s and pressure at the middle of arterial segment $\bar{p}^s$

$$C(R; \bar{p}^s, q^s) = 2\pi(1-\phi)\bar{p}^s R^2 \frac{(\vartheta^c \nu^c + \vartheta^m \nu^m)}{\sum_i \nu^i \sigma_{\theta\theta}^i} + \vartheta^b \pi R^2 + \frac{8\mu q^{s2}}{\rho_{fluid} \pi R^4}. \tag{2.30}$$

Equation (2.30) expresses the optimization problem in terms of radius given $\bar{p}^s$ and q^s. The generalization of this optimization is discussed in the following section.

2.2.5 Iterative process of optimization

A bifurcating arterial tree is initialized based on the fractal rule for vessel radii (Section 2.2.1). To update the vessel radii over entire tree the cost function minimization has to be implemented together with global hemodynamics. Algorithmically, this implementation can be done sequentially for each bifurcation or globally for all vessels at once. Without loss of generality we proceed with the sequential minimization, which is iteratively solving the global hemodynamics relation between pressure and flow, and local minimization the cost function. The iterative process is illustrated in Fig. 2.1. The pseudo-code for the optimization

procedure is presented in Appendix 5. The information transfer in this optimization can be conceived as a coupling of a G&R model with hemodynamics, similar to what was presented in [5].

2.3 Summary and conclusion

In this chapter, we developed a numerical framework to estimate the homeostatic conditions in arterial networks. This framework relies on minimizing the metabolic cost to maintain the blood volume and constituents of the wall, with the local mechanics and global hemodynamics as constraints. The proposed framework can be applied to various vascular networks given that we have a specific dataset or rules that would serve to construct the structure of the tree (i.e., vessel connectivity, length, etc.). In Chapters 3 and 4 we test our framework on models of pulmonary and coronary arterial trees.

Chapter 3

Homeostatic Baseline and Hemodynamics in the Pulmonary Arterial Tree

3.1 Introduction

Pulmonary arterial hypertension (PAH) is a complex disorder associated with an elevated pulmonary arterial pressure. Progressive stiffening and narrowing of distal pulmonary vessels result in an increase in pulmonary arterial pressure in PAH, which can lead to fatal right heart failure. The pathology of PAH is connected to the long-term vascular remodeling with prominent features such as: smooth muscle hypertrophy, endothelial dysfunction, deposition of collagen and elastin, and increased elastolytic activities [45]. Alternatively, the short-term hemodynamic effects such as the magnitude of pulse pressure and wave propagation phenomena in the pulmonary arterial tree have been observed to be influential in development of PAH (for more details see Section 1.2.1.4).

The current understanding of G&R process in PAH is greatly limited due to paucity of detailed analyses on the manner in which the pulsatile nature of hemodynamics (in the short-term scale) induces pathological changes in the vasculature (in the long-term scales) [161]. This limitation necessitates an application of temporally multiscale computational models of the pulmonary arteries that include both timescales in vascular adaptations. As explained in Chapter 2, the G&R model corresponds to long-term changes in the structure of the pulmonary arteries where the arterial wall is modeled as a constrained mixture of the wall constituents endowed with the kinetics of their production and removal. Among the main driving factors in G&R models are the hemodynamics loads (wall shear stress, and circumferential stress) on the vascular wall. On the other hand, fluid-solid-interaction (FSI) models of the pulmonary arteries facilitate the simulation of the pulsatile hemodynamics in short-time scale [74]. Realistic consideration of deformable wall properties are integral part of the biomedical FSI problems. Therefore, exchanging information between the G&R and FSI models is pivotal in the study of the progression of PAH. This coupling has been previously proposed in fluid-solid-growth (FSG) modeling framework by Figueroa et al. [5]. In this study we present a snapshot of such coupling where the pulmonary arteries are in healthy condition.

The main goals of this chapter is to establish the homeostatic baseline and simulate the pulsatile hemodynamics in a pulmonary arterial network. To this end, the current chapter is organized as follows: First, we briefly explain the workflow for assimilation of the homeostatic optimization with a 1D FSI model. Second, we provide the formulation of FSI in a pulmonary arterial tree. Subsequently, the parameters used for the implementation of the homeostatic optimization (Chapter 2) and FSI in the distal pulmonary arterial tree are examined. Finally, we present and discuss the results of the optimization in symmetric and asymmetric trees.

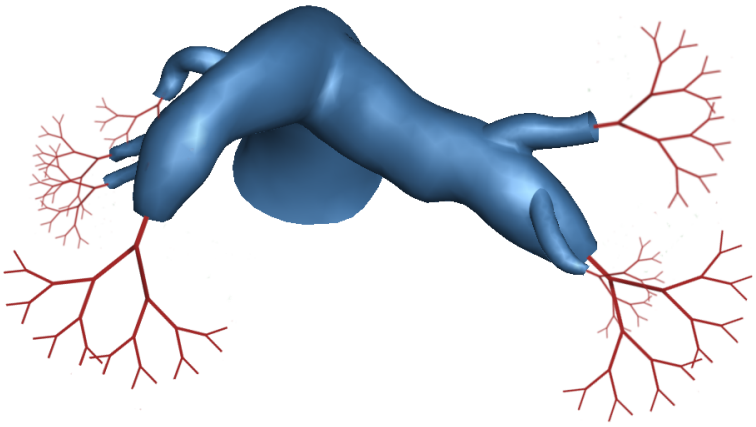

Figure 3.1: Schematic components of the pulmonary arterial tree and their corresponding data availability: large vessels (3D patients-specific anatomy, flow and pressure waveforms from clinical imaging and catheterization) and small vessels (limited morphometrical and biomechanical data).

3.2 Method

3.2.1 Fluid-solid-growth

Figueroa et al. [5] illustrated how the FSI analysis during one cardiac cycle can be coupled with an arterial G&R model through a FSG modeling framework. In our study, we extend the FSG framework to the distal pulmonary arterial tree (shown as red binary trees in Fig. 3.1). First, we established that the results of homeostatic optimization essentially construct an instant of G&R modeling where arteries are in healthy condition (Chapter 2). Second, we use small-on-large theory to compute the linearized mechanical response (i.e., Young's modulus) for the implementation of the constrained mixture model into the FSI model. We present a general formulation of the small-on-large in Appendix 5. Finally, we use a 1D FSI model (i.e., Womersley's theory) for the pulsatile hemodynamics of the pulmonary arterial tree where the vessel walls are considered linearly elastic (Section 3.2.2).

3.2.2 Pulsatile hemodynamics

Given the geometry of the tree, vessel wall stiffness, and steady-state pressure and flow from the homeostatic optimization, we proceed to obtain the pulsatile solutions and pulse wave velocity in a tree using Womersley's solutions (see Appendix 5). Note that within the homeostatic optimization formulation the fast-time hemodynamics (denoted by their Fourier domain representatives P and Q in this section) in a tree is decoupled from the slow-time problem, and thus it represents a post-processing operation after homeostatic optimization. In general, this procedure can be fully coupled with slow-time problem.

Womersley's solution to pulstatile flow in a deformable tube can be found in Appendix 5. In this section, we briefly explain the generalization to an arterial network. Each bifurcation is a reflection site for the traveling wave. Womersley's theory can be adapted to incorporate such reflections of traveling waves. Due to the system linearity the pressure and flow can be decomposed to the forward and backward waves

$$\begin{aligned} P = P_{forw} + P_{back}, \quad P_{forw} = H_{forw} e^{-i\omega z/c}, \quad P_{back} = H_{back} e^{i\omega z/c} \\ Q = Q_{forw} + Q_{back}, \quad Q_{forw} = \frac{H_{forw}}{Z^c} e^{-i\omega z/c}, \quad Q_{back} = -\frac{H_{back}}{Z^c} e^{i\omega z/c} \end{aligned} \tag{3.1}$$

with constant coefficients H_{forw} and H_{back} for individual harmonics. The characteristic impedance Z^c and velocity of the wave propagation c are the same for both forward and backward waves [162]: $Z^c = P_{forw}/Q_{forw} = P_{back}/Q_{back}$. We can define the reflection coefficient as [163, 164]

$$\Gamma = \frac{Z^T - Z^c}{Z^T + Z^c} = \left. \frac{P_{back}}{P_{forw}} \right|_{z=L}. \tag{3.2}$$

The reflection coefficient varies between -1 and 1. If $\Gamma = 0$, then no wave reflection is present, indicating that impedances match $Z^T = Z^c$. The so-called open-end type of reflection is

associated with $\Gamma = -1$, where $Z^T = 0$ or $P|_{z=L} = 0$. In this case, the reflected wave is negative [165], similar to a wave traveling in a string of fixed end. The so-called closed-end type of reflection is related to $\Gamma = 1$ for $Z^T = \infty$ or $P|_{z=L} = 0$, where the reflected wave is positive (as illustrated in analogy with wave traveling in a string of free end).

Using Γ and Z^c, total impedance at frequency ω can be obtained as a function of location along the vessel of length L.

$$Z(z,\omega) = \frac{P}{Q}(z,\omega) = Z^c \frac{1+\Gamma e^{-i\omega 2(z-L)/c}}{1-\Gamma e^{-i\omega 2(z-L)/c}}. \tag{3.3}$$

Combining equations 3.1 and 3.2, the pressure and flow along the vessel can be written as

$$\begin{aligned} P(z,\omega) &= H_{forw} e^{-i\omega z/c}(1+\Gamma e^{i\omega 2(z-L)/c}), \\ Q(z,\omega) &= \frac{H_{forw}}{Z^c} e^{-i\omega z/c}(1-\Gamma e^{i\omega 2(z-L)/c}). \end{aligned} \tag{3.4}$$

Moreover, the input impedance can be written as

$$Z^{inp} = Z^c \frac{1+\Gamma e^{-i\omega 2L/c}}{1-\Gamma e^{-i\omega 2L/c}}. \tag{3.5}$$

Considering conservation of the total pressure and flow at bifurcation and the input impedance at each daughter vessel $Z^{inp}_{d_1}$ and $Z^{inp}_{d_2}$, we obtain the terminal impedance in the parent vessels

$$Z^T_p = \left(\frac{1}{Z^{inp}_{d1}} + \frac{1}{Z^{inp}_{d2}} \right)^{-1}. \tag{3.6}$$

Given the root vessel flow q^s_p, Q_p, terminal pressure p^{sT}, and reflection coefficient Γ^T at the terminal vessels, we use bifurcation relations Eq. 3.6 to compute the input impedance eq. 3.5, recursively from the bottom-to-the top and then reconstruct the pressure and flow at each vessel of the fractal tree from the top-to-the-bottom, using Eq. 3.4.

Using wave-intensity analysis, Hollander and Colleagues [55] demonstrated that the normal

pulmonary arterial circulation (in dogs) is characterized by negative wave reflections (an open-end reflector). The primary factor for creating the open-end type of reflection in pulmonary arterial system is likely the large increase in cross-sectional area over a short distance. As discussed in [55], the magnitude of negative, open-end type reflection increases as daughter-to-parent ratio is $a_d/a_p > 1.2$.

3.2.3 Parameter selection

The parameters of the model are listed in Table 3.1. The focus of this study is on the intermediate-to-small region of the pulmonary tree, from the end of the right interlobar artery to the arterioles. For hemodynamics boundary condition at the inlet, we prescribe input flow waveform taken from human data at main pulmonary artery [67] and scaled to fourth generation downstream. The first nine harmonics are used to represent the waveform in frequency domain. The length-to-radius ratio is taken from Olufsen et al. [73] which approximates human data from a single pulmonary arterial tree cast reported in Huang et al. [23]. However, the length was scaled by a factor of half to better approximate the characteristics of the tree in the beginning of modeling tree. Terminal radius, similar to [73], defines the number of generations in a symmetric tree (this results in 19 generations). For the asymmetric case, first a full arterial tree is constructed, then the initial tree is pruned with a radius threshold of 0.18 cm which leads to different number of generations in different paths. Although the tree terminates at arteriolar level, we consider a mean terminal pressure close to the capillary pressure as the pressure drop is small between pulmonary arterioles and capillaries. The basal and active energy consumption rates for vascular smooth muscle cells are measured using the the flux of adenosine triphosphate (ATPs) in the extracellular space [166, 167]. Although the basal metabolic cost of vessel wall constituents may vary throughout the arterial tree, we chose the value 1500 W/m^3 for the entire pulmonary tree [147]. The metabolic cost of active tension in SMC, as measured in [166], is considered to be

0.00872 1/s and proportional to the active tension. Since the active tension is proportional to the mass of SMCs in the vessel wall, the metabolic cost can be written as proportional to SMC content (Eq. 2.30). Furthermore, the energy requirement for sustaining the blood in the arteries is adopted from [168] based on number of red blood cells, white blood cells, and platelets in a unit volume of blood and their oxygen consumption rate for a normal adult human subject.

The mechanical properties (Table 3.1) of the wall for the constrained mixture model are calibrated against experimental data obtained in five inflation tests of porcine right/left pulmonary arteries (conducted at Michigan State University [169]). The intrinsic material stiffness parameters are assumed to be constant for all the vessels in the arterial network. However, the pre-stretch of collagen and elastin is adjusted in each vessel downstream in order to match the thickness-to-diameter ratio reported in [170, 171]. The underlying assumption here is that in an arterial tree, the pre-stretch of the collagen and elastin are dependent on the homeostatic arterial pressure. This is inspired by the experimental observations showing wavier or even compressed collagen fibers and elastin sheets in the small arteries and arterioles with active tension [112]. The mass fractions of all constituents are estimated for the entire arterial tree: constant in Case 1 and variable in Case 2 (Table 3.1). To determine the composition of the arterial wall, the adventitial layer of arterial wall was assumed to have 95% of collagen and 5% of elastin in Case 1. The mass fractions were estimated using the relative layer thickness reported in [41] and medial layer mass fractions reported in [34]. However, the adult pulmonary arterial wall composition varies throughout the arterial tree. The variable composition of the wall is reflected in the model (Case 2) by changing the content of elastin and SMCs in the medial layer using data from [41]. Particularly, most of the arteries larger than 0.32 *cm* in diameter are elastic arteries endowed with multiple layers of elastic lamina. The arterial structure transitions from elastic to muscular type over a range of 0.32-0.2 *cm* where the elastic layers fragment and are replaced by SMC [172]. The arteries smaller than 0.2 *cm* have a muscular media with two distinctive internal and

Table 3.1: Model parameters for homeostatic optimization and pulsatile hemodynamics

Parameter description		**Ref.**
Initialization of the tree geometry		
Root vessel radius	0.55 cm (symm); 0.36 cm (asymm)	[73]
Root vessel wall thickness	0.42 cm	[170]
Terminal radius	0.005 cm (symm); 0.018 cm (asymm)	[73]
Radial exponent	2.72	
Daughter-to-parent area ratio	1.2	
Extended Murray's law		
Metabolic cost of collagen and SMC	1500 W/m^3	[147]
Metabolic cost of blood supply	51.7 W/m^3	[168]
Metabolic cost of active tension	0.00872 $1/s$	[166]
Vessel wall		
Wall density	1060 kg/m^3	
Case 1: Constant mass fractions (c/m/e)	77%/12%/11%	[34]
Case 2: Variable mass fractions	77-59% collagen, 12-39% SMCs, 11-2% elastin	[29]
Passive and active wall elasticity parameters	$c_1 = 28.83Pa/kg, G^e_\theta = G^e_z = 1.16 - 1.27$ $c_2 = 178.60Pa/kg, c3 = 1.05, G^k_h = 1.08 - 1.15$ $G^k_h = 1.15 - 1.08, \alpha^k = 0, \pm 45°, 90°$ $c_4 = 24.51Pa/kg, c_5 = 0.75, G^m_h = 1.21$ $S = 20kPa, \lambda_M = 1.2, \lambda_0 = 0.7$	
Hemodynamics		
Input flow waveform, scaled by 1/8	mean flow 11.65 ml/s	[67]
Length-to-radius relations, scaled by 1/2	$L = 6.2R^{1.1}mm$	[73]
Symmetric tree: mean terminal pressure	10 mmHg	[74]
Terminal reflection coefficient	-1	[55]
Blood density	1060 kg/m^3	
Dynamic viscosity	0.0035 Pa.s	

external elastic laminas [29]. While the arteries smaller than 0.01 cm are not included in this study, we note that the number of muscular arteries significantly drops when the arterial size approaches 0.01 cm and below so that the vessels become partially or fully non-muscular.

3.3 Results and discussion

3.3.1 Symmetric tree

An advantage of symmetric tree is that any vessel within a generation is representative of the whole generation, and thus the results can be evaluated with respect to generations rather than individual vessels.

3.3.1.1 Case 1: constant mass fractions

In this section we show the results of the homeostatic optimization related to the constant mass fractions Table 3.1. The study by Huang and colleagues [23] on the branching pattern and vascular geometry of the human pulmonary arterial trees found 15 orders in the pulmonary arteries using the Strahler ordering system. In their study, 1st and 15th orders correspond to the precapillary vessels and right/left pulmonary arteries, respectively. A comparison of results obtained in the current study to the results from Huang et al. [23] indicates an agreement between the diameter of our 1st generation and their 14th order pulmonary vessel corresponding to the Strahler ordering technique. Figure 3.2 compares the reported human data for right interlobar artery [73] and larger vessels [23]. The exponent ξ in daughter-to-parent radius relation along the tree (Fig. 3.2, right panel)) remains close to the cubic relation (Murray's law).

The wall thickness is obtained from the mass of the constituents resulting from the optimization. The resulting thickness-to-diameter ratios, by tuning the pre-streches, are shown in Fig. 3.3, top-left panel. Pressure in the middle of the arterial segments along the tree is shown in (Fig. 3.3, top-right). Pressure gradient becomes steeper towards the arteriolar level to meet the terminal pressure. Finally, homeostatic shear and circumferential stresses are obtained

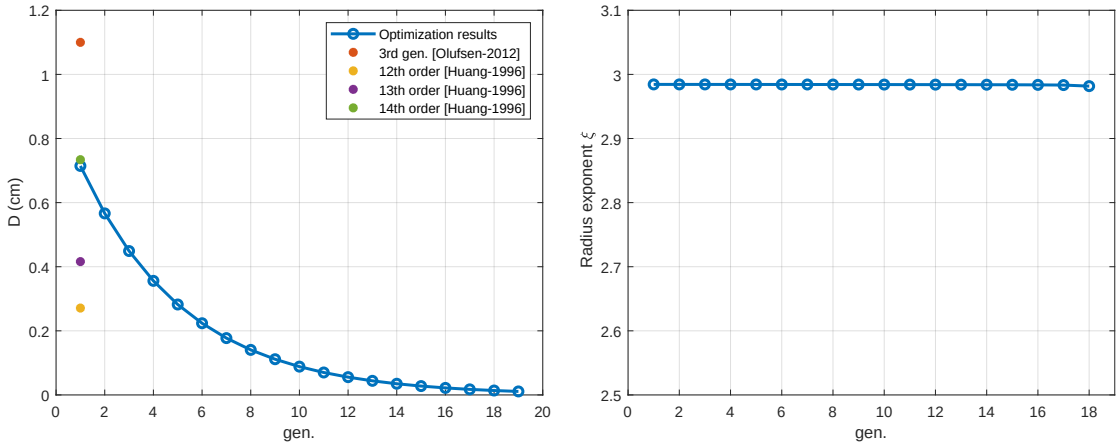

Figure 3.2: Symmetric tree – homeostatic optimization results plotted versus generation number: Left: diameter distribution compared to reported data of larger vessels; Right: radius exponent in daughter-to-parent radii relation;

(Fig. 3.3 bottom row). Although the original Murray's law implies that the wall shear stress is constant throughout the arterial tree [173], wall shear stress value increases in our model, which is consistent with the experimental studies for the systemic circulation [148,174]. The decreasing trend of circumferential stress value (Fig. 3.2, bottom-right) is consistent with observations in the coronary arterial network [144].

3.3.1.2 Case 2: variable mass fractions

Experimental studies by Hislop and Reid [29] showed that the composition of the pulmonary arteries varies across the arterial tree. This variability was taken into account by modifying mass fractions based on the composition in Table 3.1

Two distinct optimizations results for Case 2 are compared to Case 1 in Fig. 3.5. During the transition region (Fig. 3.4) elastin is replaced by two materials that require metabolic energy for maintenance (i.e., metabolically expensive materials). The optimization, however, prefers a smaller vessel with more percentage of collagen and SMCs to a large vessel with less

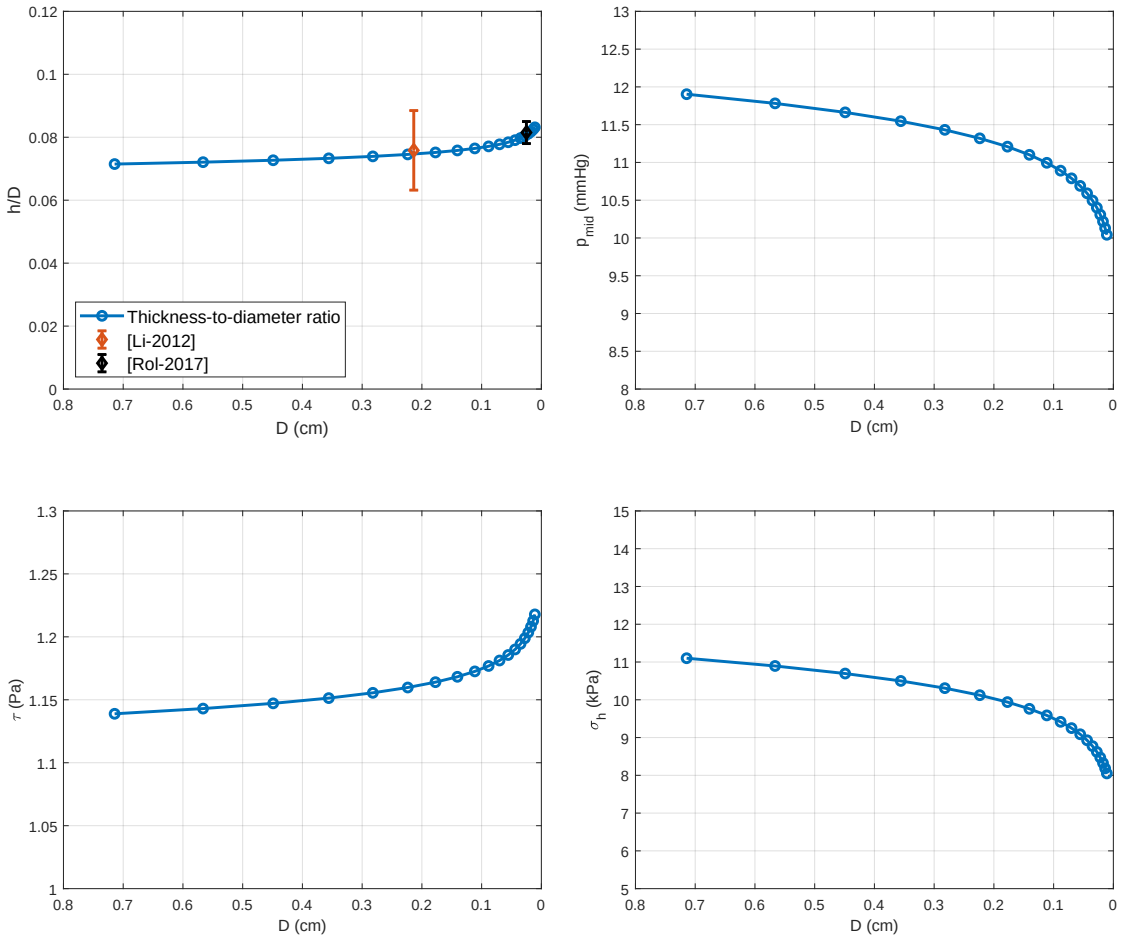

Figure 3.3: Symmetric tree – homeostatic optimization results plotted versus diameters: Top-left: wall thickness-to-diameter ratio (h: wall thickness); Top-right: mid-artery pressure; Bottom-left: homeostatic value of wall shear stress (τ); Bottom-right: homeostatic value of circumferential stress σ_h.

percentage of collagen and SMCs. This is reflected in a drop in the radius exponent (Fig. 3.5, left). The drop in results in a step-increase of the wall shear stress (Fig. 3.5, right). The stiffness results from the homeostatic optimization are obtained from a linearization of orthotropic elastic membrane properties in the p_{mid} of each artery (Appendix 5). The axial Young's modulus is markedly lower than those in systemic arteries [160, 175]; and both decrease across the generations (for both cases, Fig. 3.6, left). An increase of compliance distally is consistent with the reflections site of the open-end type which is imposed in the

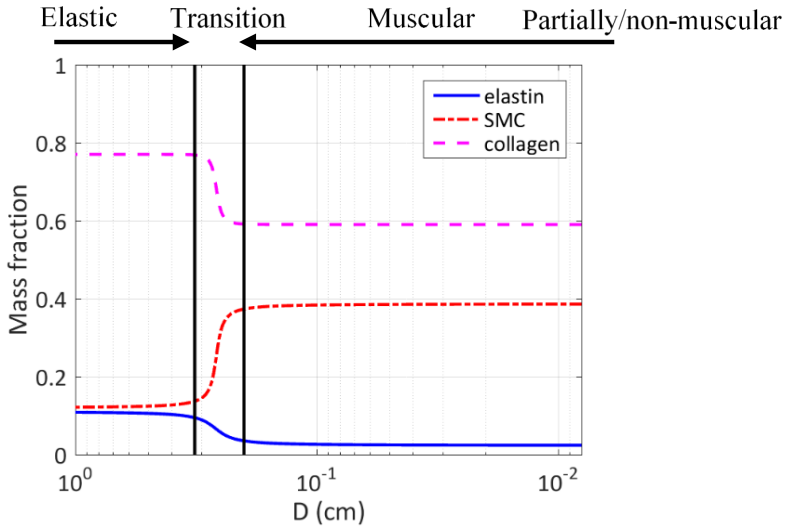

Figure 3.4: Prescribed variable mass fractions of the wall constituents: elastin, smooth muscle cells and collagen. The arrows on the top show the trend in arterial composition.

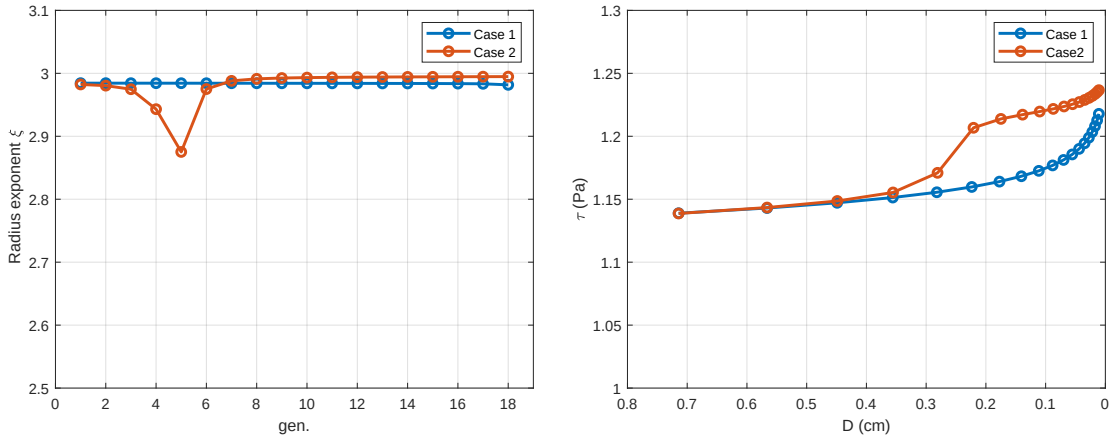

Figure 3.5: Symmetric tree – Left: radius exponent in daughter-to-parent radii relation; Right: homeostatic value of wall shear stress.

model [55]. Comparison between the two cases of modeling shows that the axial stiffness drops significantly in the muscular arteries. This result is expected since most the smooth muscle cells are oriented circumferentially in the vessel wall.

It is experimentally a challenge to estimate the *in-vivo* arterial stiffness of distal pulmonary tree. However, experimental studies have employed a distensibility parameter λ which be

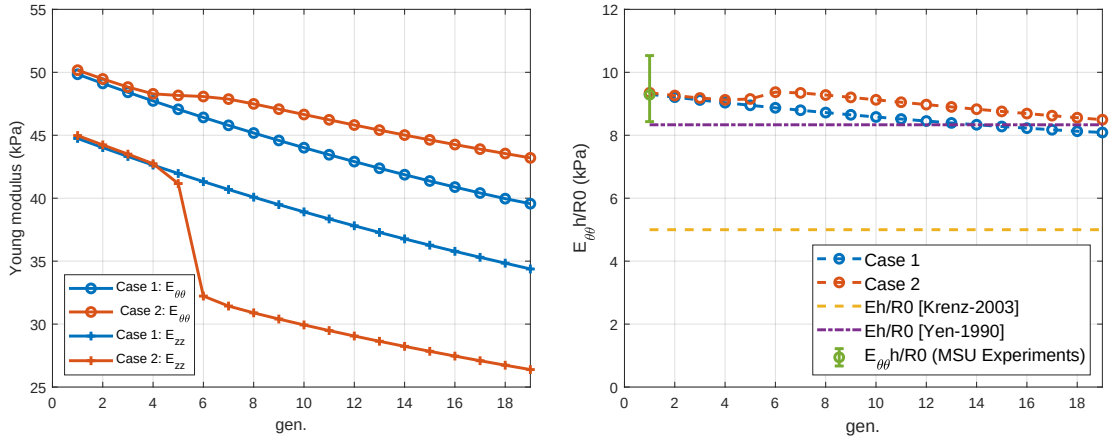

Figure 3.6: Symmetric tree – homeostatic optimization results for the wall stiffness versus generation number: Left: Young's modules in circumferential and longitudinal directions; Right: Structural stiffness normalized by the unstressed radius and compared to distensibility relations from data.

used to construct the relation $R/R_0 = 1 + \lambda p$ with transmural pressure p and radius at zero pressure R_0. For instance, Yen and colleagues [176] analyzed the mechanics of the arteries of different sizes dissected from human lung and concluded that the distensibility does not vary significantly with size (with $\lambda = 0.012$/mmHg). Alternatively, Krenz and Dawson [177] conducted a meta-analysis on different pulmonary arteries of various animals with different sizes and while they confirmed that the distensibility is almost constant, they reported a larger value of $\lambda = 0.02$/mmHg. To be able to compare our results to these studies, we use a normalized ratio of structural stiffness to the unstressed radius which can be expressed via distensibility parameter $Eh/R_0 = 3/(4\lambda)$ [74]. Right panel of Fig. 3.6 shows a near constant value for the normalized stiffness for the variable mass fraction simulation (Case 2) which is consistent with experimental studies. Moreover, the computed stiffness from the model is consistent with that of our experiments on pig's pulmonary artery (indicated for the first generation in Fig. 3.6, right panel). However, the optimization is predicting larger stiffness (smaller distensibility) compared to other experimental studies.

3.3.1.3 Pulsatile hemodynamics

Before discussing the results of the fast time hemodynamics, it is important to note that we used the optimization results of Case 2 for the following analysis since it captures the physiology of the downstream arteries more accurately. Furthermore, to validate the choice of $\Gamma = -1$ for the open-end wave reflection, Fig. 3.7 shows the duaghter-to-parent area ratio compared to bounds proposed by Hollander and colleagues in 2001 [55].

One of the most valuable outcomes from the modeling of pulsatile flow in the distal vasculature is estimation of the pulse wave velocity (c) across the tree (see Appendix 5). The pulse wave velocity (shown for two harmonics in Fig. 3.8, left) depends on the stiffness of the wall as well as Womersley's number $\alpha = R\sqrt{\omega\rho_{fluid}/\mu}$ (shown for two harmonics in Fig. 3.8, right). Particularly, the decrease in α indicates the dominance of viscous forces in small arteries (consistent with higher resistance) relative to transient inertial forces. The pulse wave velocity in the first generation shows excellent consistency with the experimental measurements of c in main pulmonary arteries [178, 179]. Moreover, heterogeneous stiffness of the arterial wall and α result in a steep decrease in c after the first few generations. The idealized Moens-Korteweg (MK) ($c^{MK} = \sqrt{Eh/2R\rho_{fluid}}$) pulse wave velocity is also plotted for the comparison. Clearly, the assumptions of MK equation, such as non-viscous fluid, are voided in smaller vessels.

To understand limitations of the model, we check the validity of the deformable wall Womersley's theory by computing the ratio of maximum lumen oscillatory velocity to the pulse wave speed, $\delta_{max} = \max_t v_z^f/c$, which must be significantly smaller than 1 for the long wave approximation to be valid. Figure 3.9 shows that at first several generations of the tree, there might be significant nonlinear contribution (nonlinear inertia term for fluid flow) which is neglected in the Womersley theory.

Total hemodynamics solution along the vascular bed is demonstrated in Fig. 3.10. The

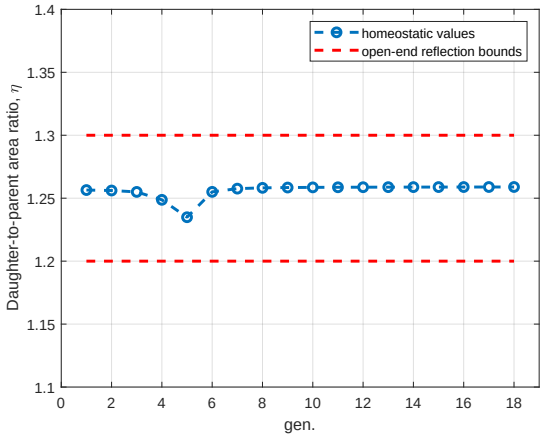

Figure 3.7: Symmetric tree – daughter-to-parent area ratio within the range of open-end type of reflections.

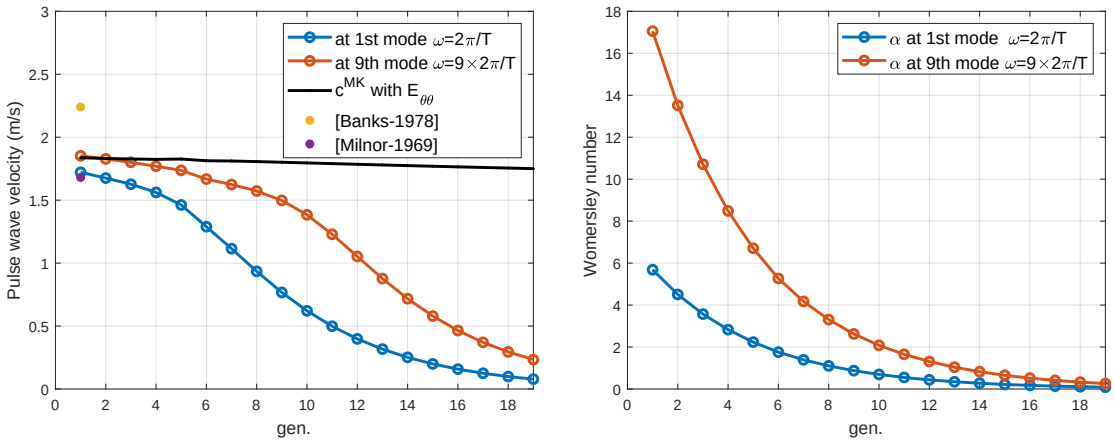

Figure 3.8: Symmetric tree – pulsatile hemodynamics results versus generation number: (a) pulse wave velocity for two harmonics, compared to data and MK velocity; (b) Womersley's number for two harmonics.

total input flow splits evenly at each generation. The total terminal pressure is within the physiological range 8-25 mmHg. The minimum extreme is located below the mean pressure that is consistent with negative reflections

The patient-specific models reconstructed from medical images of large pulmonary arteries can be connected to the distal vasculature model via an impedance boundary condition at

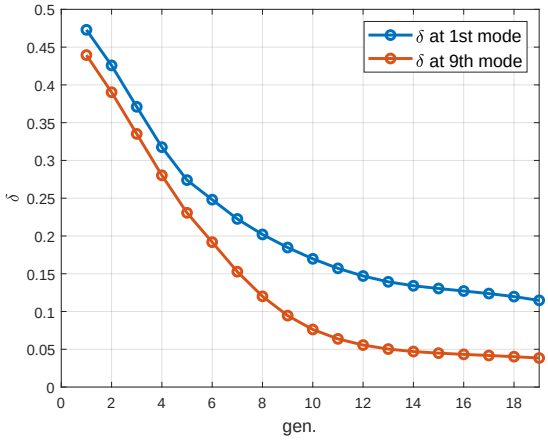

Figure 3.9: Symmetric tree – Womersley's solution validity check as function of generation number for two different harmonic modes.

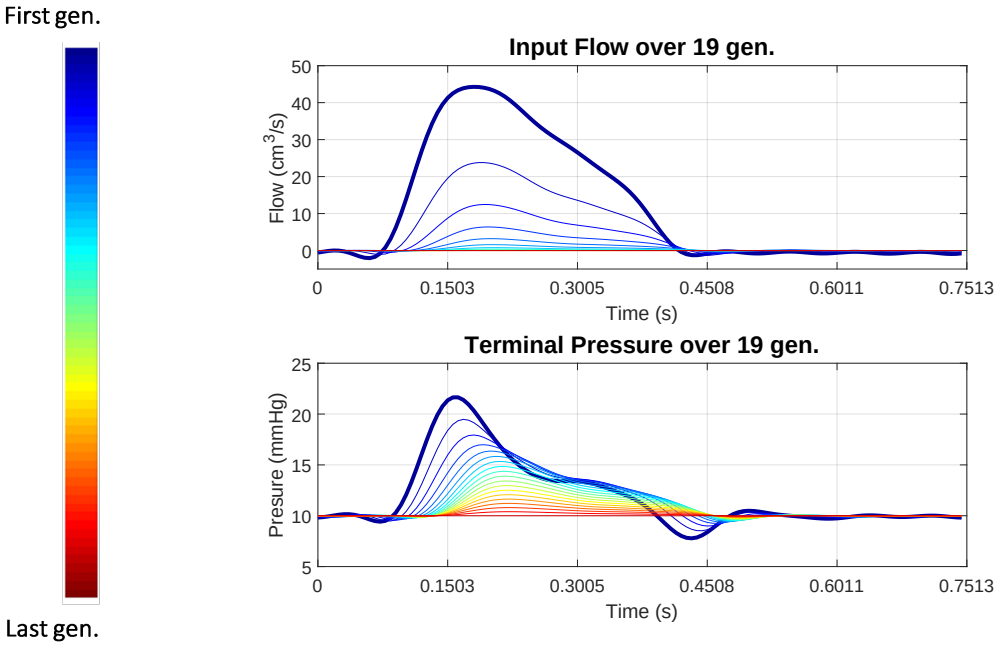

Figure 3.10: Symmetric tree: Total input flow (top) and terminal pressure (bottom) over the generations

the interface. The outflow impedance at the large vessel is equivalent to input impedance at following vascular tree. Finally, using the pulsatile hemodynamics at the root vessel we compute the input impedance for the arterial tree (Fig. 3.11). For comparison we plot

characteristic and terminal impedance at the root vessels.

3.3.2 Asymmetric tree

This section illustrates a asymmetric tree example for the homeostatic optimization and hemodynamics. Initially, an asymmetric tree is generated by the area ratio $\eta_0 = 1.2$ and radial exponent $\xi_0 = 2.72$ following [73]. Homeostatic optimization on such a tree leads to a symmetric tree as a result, since the symmetric structure is more energy efficient. To introduce asymmetry in the optimization, the initial arterial tree is pruned with a terminal radius of $R_{min} = 0.018\ cm$. For the steady state hemodynamics, the boundary conditions are switched to pressure at the inlet and flow at the outlets. Homogeneous distribution of the perfusion flow over all the outlets has been used in other attempts for anatomic reconstruction of arterial networks [124, 180]. Although the homeostatic optimization is capable of simulating a highly asymmetric tree, only a slightly asymmetric tree is considered in this study to ensure that the analytical solution is valid in the fast-time hemodynamic analysis. Therefore, an initial tree with 15 generation is constructed (32,767 vessels) and then pruned with respect to the terminal radius, which resulted in 4,233 individual segments in 14 generations. Without loss of generality, we identify a short and a long path (X) along the tree for presentation of results.

Figure 3.12 shows the results of the optimization, bounded by the shortest and longest paths, for the asymmetric case mass fractions are determined from Case 2. At the outlet vessels the flow is the same while terminal pressure is not (Fig. 3.12 top) as expected from the boundary conditions. The distribution of results within the bounds can be explained by dominance of the symmetric subtrees. The ratio of structural stiffness to unstressed radius is distributed around 9 kPa and varies more toward the outlets (Fig. 3.12 bottom-right). The wall shear stress, affected by variable mass fraction (Case 2) increases toward outlets

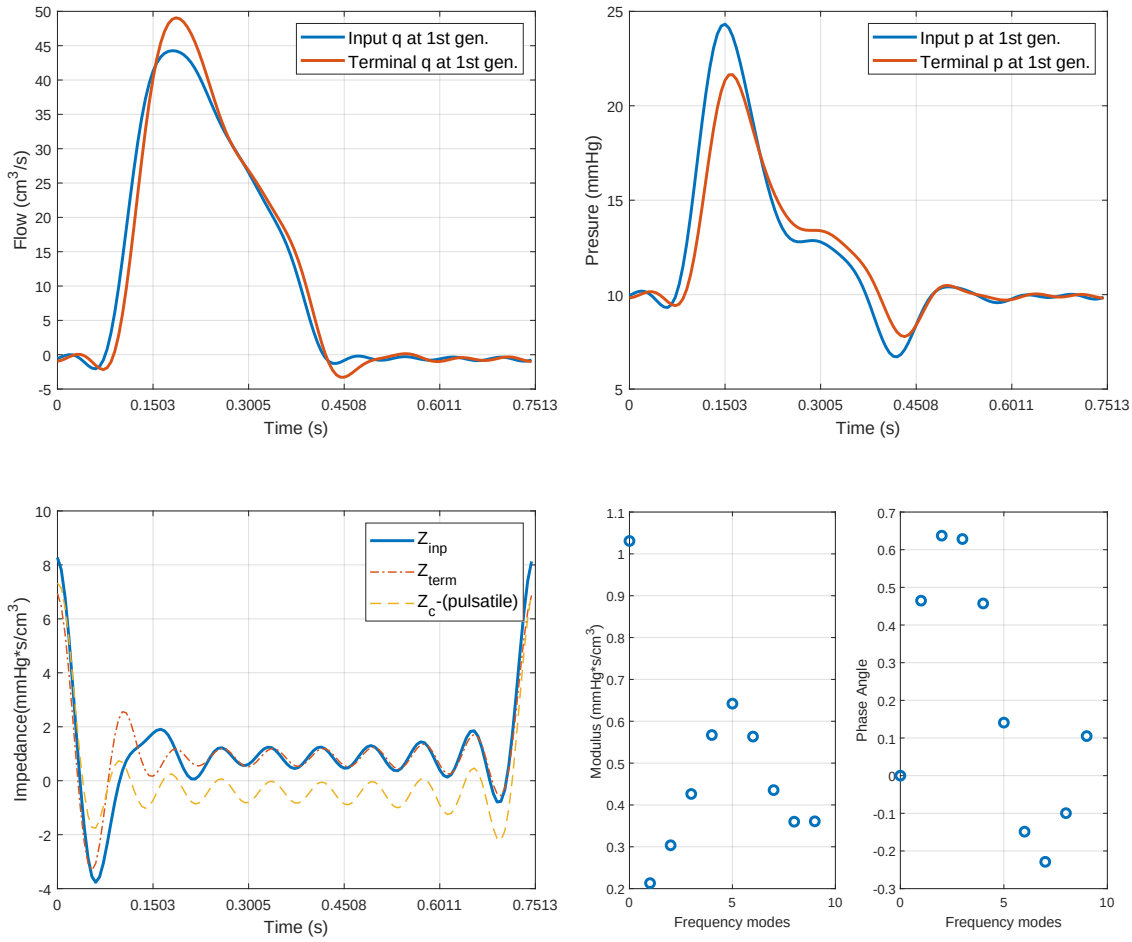

Figure 3.11: Symmetric tree – Top: total flow and pressure at the root vessel of the distal tree; Bottom-left: root vessel input impedance in time domain compared to terminal and characteristic impedance; Bottom-right: input impedance modulus and phase angles in the frequency domain.

(Fig. 3.12 bottom-left).

Left panel of Fig. 3.13 shows the δ parameter for the longest and shortest paths of the asymmetric tree. For number of generations smaller than 10 in the shortest path, the δ parameter becomes significantly larger than 0.5 which indicates that the Womresley theory is not valid in those branches (the simulation not shown). Furthermore, the right panel of Fig. 3.13 shows c for the longest and shortest paths. The speed of the wave propagation seems to be larger in the longer paths given the depth of the vessel segment in the arterial

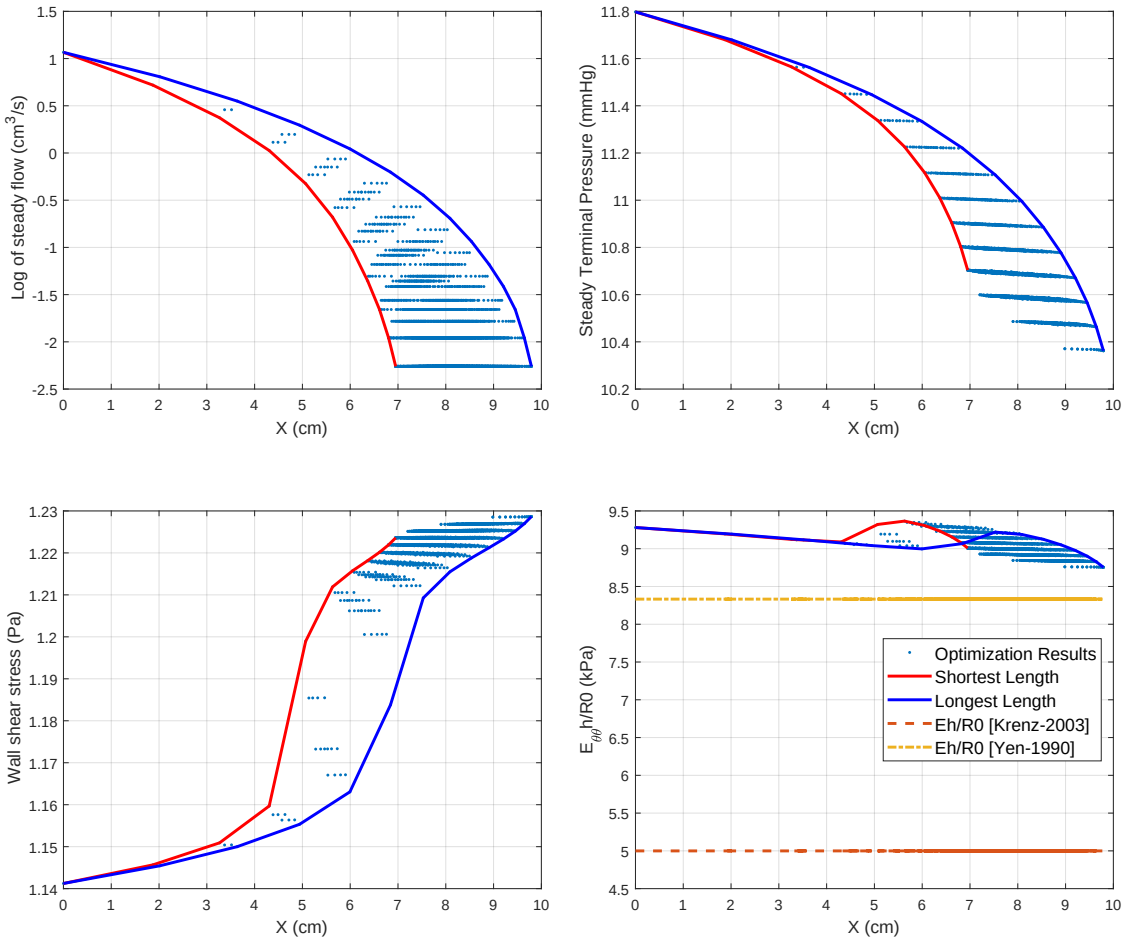

Figure 3.12: Asymmetric tree – homeostatic optimization results versus distance (from the root, along the branch pathway), dots represents optimization results for each vessel, red and blue lines indicate the short and long path, respectively: (a) log of steady-state flow rate; (b) terminal steady pressure; (c) ratio of structural stiffness to unstressed radius; (d) homeostatic value wall shear stress.

tree.

Finally, the pulsatile hemodynamics at the root of the arterial tree is computed and shown in Fig. 3.14. The asymmetric structure of the arterial tree significantly changes the impedance at the root of the artery. This is particularly crucial since this impedance can be used as an outlet boundary conditions in the patient-specific modeling. Therefore, an accurate analysis of the distal tree is crucial in performing realistic hemodynamics simulations.

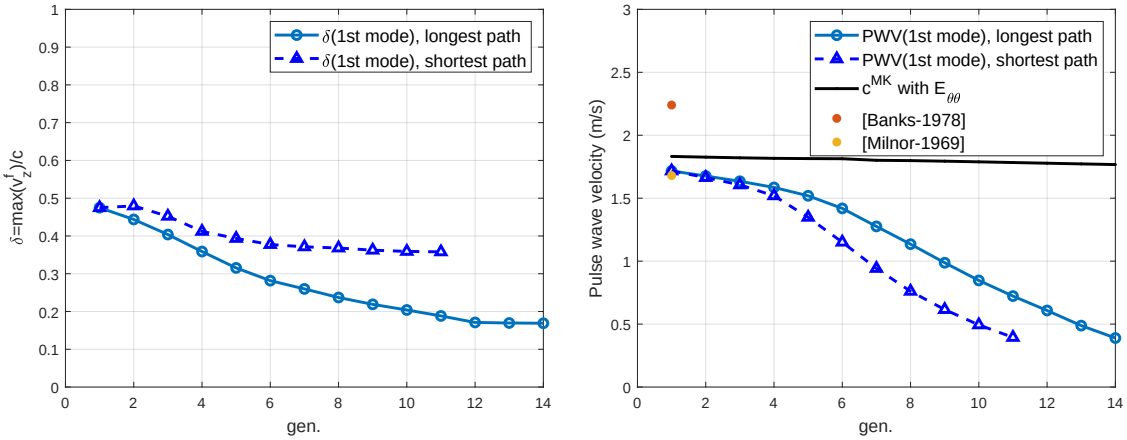

Figure 3.13: Asymmetric tree – delta parameter and pulse wave velocity for longest and shortest paths.

3.4 Summary and conclusion

We successfully implemented the homeostatic optimization method to estimate the baseline state of the distal pulmonary arterial tree. Our study included vascular tissue properties via a constrained mixture model (previously used for G&R) as well as the pulsatile hemodynamics using the metabolic demand considerations (Murray's law) and an analytical blood flow theory. Particularly, the vessel sizes and mechanical properties were estimated using an extension of Murray's law, and Womersley's theory was used for simulating the pulsatile blood flow in a network of elastic vessels. The material behavior of the vessel wall, presented by orthotropic membrane, was described by nonlinear constitutive law at slow time-scale, and then linearized at the steady pressure to obtain a pulsatile solution for cardiac cycle. The proposed method does not necessitate computational cost associated with nonlinear problem solvers, nested iterative optimizations, and complex tree morphometry. Instead, our framework is a computationally efficient tool that greatly simplifies the biomechanical analysis in vascular trees. Indeed, it allows focusing primarily on complex wall tissues processes and associated biomechanical/biochemical stimuli. We have illustrated the

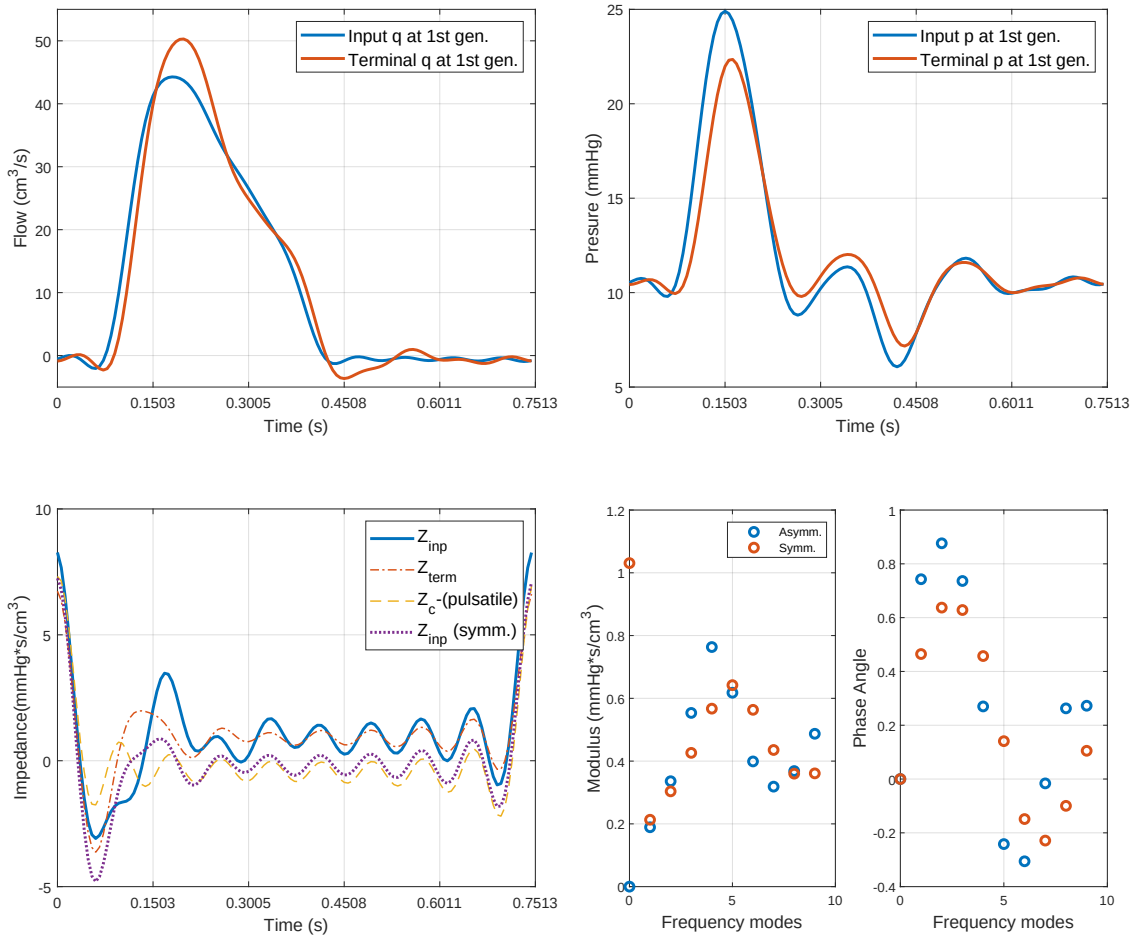

Figure 3.14: Symmetric tree – Top: total flow and pressure at the root vessel of the distal tree; Bottom-left: root vessel input impedance in time domain compared to terminal and characteristic impedance; Bottom-right: input impedance modulus and phase angles in the frequency domain.

framework functionality on examples of symmetric and asymmetric binary trees representing distal intermediate pulmonary arterial vasculature. The results show good agreement with the available experimental and clinical observations. The homeostatic optimization provided the wall composition content, vessel size, and structural stiffness giving valuable estimation of intrinsic wall properties that otherwise are not measurable (at the range of 14-19 generations after the large vessel). In addition, the hemodynamics solution gave the total pressure and flow distribution along the tree revealing the evolution of arterial pressure which is a

crucial marker for pulmonary arterial hypertension. While in our examples we considered healthy subjects, the proposed framework can be applied to pulmonary hypertension subjects once more clinical and experimental data are available. Another not measurable distally but valuable characteristic is the pulse wave velocity distribution along the tree. Our results demonstrated the decrease of pulse wave velocity over the generations as a consequence of wall stiffness and Womersley number changes. Furthermore, the low computational cost of our model renders it immensely useful for parametric studies, as illustrated by considering cases of constant and variable mass fractions of wall constituents. The proposed framework is also useful for obtaining the impedance outflow boundary conditions essential for coupling distal vasculature with large vessel 3D simulations in the patient-specific models. We reported such input impedance obtained for the symmetrical and asymmetric trees. In this study, we used constant blood viscosity which is justified for the intermediate range of vessel size. However, constant viscosity is not a requirement of the formulation though it greatly simplifies fluid dynamics. For microvasculature closer to capillaries, the apparent viscosity can be considered as a function of vessel diameter and hematocrit level [181]. In this case, the total hemodynamics has to be generalized to accommodate viscosity updates. Additional data and work are needed to improve the pulmonary arterial tree model. In presented examples, the tree is described by a fractal structure based on a bifurcating radial rule. In future, the tree structure has to be reconstructed from a comprehensive morphometry of the pulmonary arterial tree. Ideally, such morphometry has to be statistically representative for human subjects, specific for age group, healthy or affected by pulmonary hypertension – these are data and tasks that are currently unavailable, limited, and/or challenging. Similarly, in the current examples, the wall parameters and constituent content was estimated from limited open-literature resources and internal experiments. Thus, to improve and validate the arterial wall modeling there is a need of more experimental data on pulmonary arterial wall tissue mechanics for humans.

Chapter 4

Baseline Characteristics and Adaptations in Coronary Flow Regulation

4.1 Introduction

Coronary arteries are responsible for supplying blood to the myocardium. The coronary arterial network is inherently different from other circulatory systems in the body in two major aspects. First, since the heart has limited anaerobic capacity, energy production in myocytes is highly dependent on oxidative phosphorylation [82]. Therefore, a continuous supply of oxygen to the cardiac myocytes is necessary for normal function and without sufficient oxygen delivery, their contractile function declines within seconds of the ischemic insult. The continuous supplement of oxygen to myocytes is a burden on the coronary vasculature, i.e., a tight regulation of coronary vascular functions is necessary for maintaining the blood circulation in the heart and eventually the whole cardiovascular system (for more

details see Section 1.2.2).

Second, myocardial arteries are under significant compressive forces from the myocardium during the systolic phase. The interaction of compressive forces and vascular wall (namely myocardial-vascular interactions) are hypothesized to be primarily dependent on the cavity-induced extracellular (interstitial) pressure (p_{CEP}), muscle shortening-induced pressure (p_{SIP}), and changes of myocardial stiffness (i.e., varying elastance) [88]. Dependence on p_{CEP} implies that the compressive forces are larger in the inner layers of the left ventricle (LV) than those in the outer (epicardial) layers [182]. It has been long established that this variation in pressure affects the flow distribution and structure of the arteries in different layers [183].

Determination of the spatially differential baseline characteristics of the coronary arteries is crucial for the analysis of the coronary flow regulation, since the active response of the vessels to changes in biomechanical and/or biochemical stimuli varies with their size and location in the cardiac wall. Most of the flow regulation occurs in the networks of tree-like branching arteries in the different layers of the myocardium (subepicardial, mid-wall, and subendocardial) [81, 82]. Similarly, the resistance arterties in the coronary arterial network are less than 100 μm in size and reside in the myocardial layers of the cardiac wall [184]. These vessels are main regulators of the flow control mechanism by intrinsic and/or extrinsic modifications in diameter via vasoreactivity of smooth muscle cells (SMCs).

In this chapter, we aim to first apply the homeostatic optimization framework to establish the baseline characteristics of two coronary arterial trees in subendocardial and subepicardial layers. Next, we use the defined baseline to study coronary flow regulation. Particularly, differential analysis of the pressure-flow autoregulation will be performed. Finally, we test the capability of the model in capturing the effects of drug administrations, such as adenosine infusion and inhibition of NO synthesis.

4.2 Methods

4.2.1 Baseline construction of coronary arterial tree

The general workflow of arterial tree construction is described in Chapter 2. In this chapter, the optimization workflow is implemented to construct a coronary microvascular tree model embedded in different layers of the myocardium with specific scale factors. First, two symmetric trees (subendocardial and subepicardial) with 12 generations of vessels are generated with the initial radial exponent $\xi = 2.55$ based on Arts and Reneman [182] and Karch et al. [124]. This choice of ξ is motivated the experimentally observed fractal nature of the vasculature [121]. The length-to-diameter ratio is prescribed using the morphometric swine data from Kassab et al. [24]. The subendocardial and subepicardial trees are assumed to be located in 5/6 and 1/6 of the myocardium, respectively.

For modeling, we consider the slow-time conditions (average over minutes to hours), and a mean intramyocardial pressure is imposed on the individual vessel depending on its location. Specifically, the mechanical equilibrium is written as

$$p_{tm} r = T_{\theta\theta}, \tag{4.1}$$

where p_{tm} is the transmural pressure of the blood vessels located within the myocardium, $T_{\theta\theta}$ is given by equation (2.19), and r is the inner radius of the segment. The transmural pressure can be written as

$$p_{tm} = p - p_{im}, \tag{4.2}$$

where p is the luminal pressure as presented by previous chapters and p_{im} is the intramyocardial pressure. Following the analysis by Algranati et al. [88] on myocardium-coronary

vessel interaction, p_{im} is assumed as

$$p_{im} = p_{CEP} + p_{SIP}. \tag{4.3}$$

For the free wall of the LV, p_{CEP} varies linearly from endocardium (LV pressure, p_{LV}) to pericardium, where the pericardial pressure is assumed to be negligible. Therefore, for the subendocardial and subepicardial trees in this chapter, the average p_{CEP} values are 5/6 and 1/6 of p_{LV}, which is consistent with their respective relative myocardial depth. The pressure p_{SIP} was chosen so that the p_{im} in the subendocardium is 20% larger than the p_{LV} [71]. The boundary conditions of the baseline optimization in both subepicardial and subendocardial trees are the inlet and outlet pressures. In addition, the layer-wise total flow in the arterial tree is considered as an extra constraint.

4.2.2 Coronary flow regulation

Coronary blood flow is tightly regulated as a response to changes in perfusion pressure and/or imbalance between myocardial oxygen demand and supply. The reactivity of the vessel wall to changes in stimuli is dominated by the SMCs. From the constrained mixture model in Chapter 2, the active stress T_{act} in the smooth muscle is

$$T_{act} = \frac{S}{\rho}\Big(1 - \Big(\frac{\lambda_M - \tilde{\lambda}}{\lambda_M - \lambda_0}\Big)^2\Big), \tag{4.4}$$

where λ_M and λ_0 are stretches at which the active force generation is maximum and zero, respectively, and S is the stress at the basal vasoactive tone. Moreover, $\tilde{\lambda}$ is an active stretch which can evolve by SMC remodeling. Since we model the short timescale adaptations (minutes to hours), SMC remodeling is not considered which results in $\tilde{\lambda} = \lambda_{\theta.}$. The parameter S, the basal active tone, is a function of transmural pressure, and shear stress from their

homeostatic values, and the cardiac activity (MVO_2), which gives

$$S = A(p_{tm} - p_h, \tau - \tau_h, \mathrm{MVO}_2) S_{max}(p_{tm}). \tag{4.5}$$

The activation, A, determines the activation level from fully dilated to fully constricted. The maximum active stress, S_{max}, is a function of transmural pressure as was observed in [102] and shown in Fig. 4.3. Following the work of Cornelissen and colleagues [135], we assume that the maximum active tone has a sigmoidal shape, described with a hill curve

$$S_{max}(p_{tm}) = S_0 \frac{p_{tm}^{\beta}}{p_0^{\beta} + p_{tm}^{\beta}}, \tag{4.6}$$

where β is the slope of the curve, S_0 is the maximum tone, and p_0 is the a parameter that offsets the center of the curve. Three primary mechanisms that predominantly regulate the vascular reactivity are myogenic (pressure), shear stress, and metabolic controls. The flow regulation is essentially a dynamic process involving activation of each of these mechanisms with their respective time response. In this study, however, we focus on the steady state of the vasculature, which is reached within 2 minutes after the perturbation form the homeostatic value [89, 116, 132]. This time-scale is large enough for our analysis to be valid with respect to the discussion in Section 3.1.

Myogenic control is the SMC contraction in response changes in the local wall stress determined by the transmural pressure. The deviation from the basal (homeostatic) pressure (p_h) leads to a constrictive stimulus. This stimulus in each vessel can be written as

$$s_p = a_p\left(\frac{p_{tm} - p_h}{p_h}\right). \tag{4.7}$$

Contrary to myogenic tone, an increase in wall shear stress, induces relaxation of the SMCs facilitated by an increase the NO production of the endothelial cells. This vasodilation

stimulus can be written as

$$s_\tau = -a_\tau(\frac{\tau - \tau_h}{\tau_h}). \tag{4.8}$$

Finally, experimental studies have shown that during an increased MVO_2 (e.g., exercise), while the oxygen extraction capacity of the cardiomyocytes does not change [99]. Therefore, an increase in MVO_2 must be met with a proportional increase in flow rate. Although the measurement of MVO_2 is not directly used, the flow can be conceived as the representative of metabolic demand [116]. Therefore, the metabolic mechanism of flow regulation can be written as

$$s_m = -a_m(\frac{\hat{q}(\mathrm{MVO_2}) - q_{term}}{q_{term}}), \tag{4.9}$$

where $\hat{q}(\mathrm{MVO_2})$ is the target flow as a function of the myocardial oxygen consumption, and q_{term} is the flow rate at the terminal arterioles.

To write the integrated stimuli from the mechanisms, two following factors are considered. First, the effectiveness of the mechanisms is different for arteries at different sizes. In particular, the myogenic reactivity is the highest in blood vessels with 100 μm diameter [102, 135] while the shear-dependent vasodilation becomes mostly blunted vessels smaller than 100 μm [118]. Meanwhile, the signal for metabolic response from different signaling pathways (oxygen imbalance and/or adrenergic) is originated in capillaries and is conducted upstream to precapillary arterioles [132]. The conducted response, however, decays exponentially so that it mostly affects the arterioles. Second, the above-mentioned phenomenological equations only describe the stimuli when a deviation from homeostasis is occurred (i.e., stress condition). However, smooth muscle cells maintain a basal tone under resting conditions [185]. This smooth muscle tone is expressed as a basal stimuli mediated by the control mechanisms.

Considering these factors, we can express the total stimuli as

$$s_{total} = \phi_p(r)(s_p + s_{0p}) + \phi_\tau(r)(s_\tau - s_{0\tau}) + \phi_m(r)(s_m - s_{0m}), \tag{4.10}$$

where s_{0p}, $s_{0\tau}$ and s_{0m} set the basal tone in SMCs at rest ($s_0 = \phi_p(r)s_{0p} + \phi_\tau(r)s_{0\tau} + \phi_m(r)s_{0m}$). Furthermore, ϕ_p, ϕ_τ, and ϕ_m are the weights representing the effectiveness of each mechanism in the total stimulation (Fig. 4.1). These stimuli dictate the activation in the SMC tone where full activation ($A = 1$) represents maximal constriction and zero activation ($A = 0$) represent the full dilation. Following [132], a sigmoidal function is used to convert the stimuli to the activation level

$$A = \frac{1}{1 + \exp(-s_{total})}. \tag{4.11}$$

The modeling framework for the flow regulation starts with introducing a stimulus for autoregulation (change in pressure) or exercise (change in MVO_2), and the simulations are conducted in two nested loops. The inner loop determines the diameters (i.e., resistances) and the outer loops computes the hemodynamics using Poiseuille flow and updates the activation levels. The procedure is continued until convergence in flow and pressure (Fig. 4.2).

4.2.3 Model parameters

Hemodynamics - In this study, we perform the homeostatic optimization on two arterial trees located downstream of the LAD, and inside the free wall of LV. Assuming that the pressure drop in epicardial arteries is small, the inlet pressure is considered to be the same as the aortic pressure 100 mmHg. Moreover, the outlet pressure at the terminal arterioles is considered 55 mmHg [186]. The total ratio of subendocardial to subepicardial flow rates

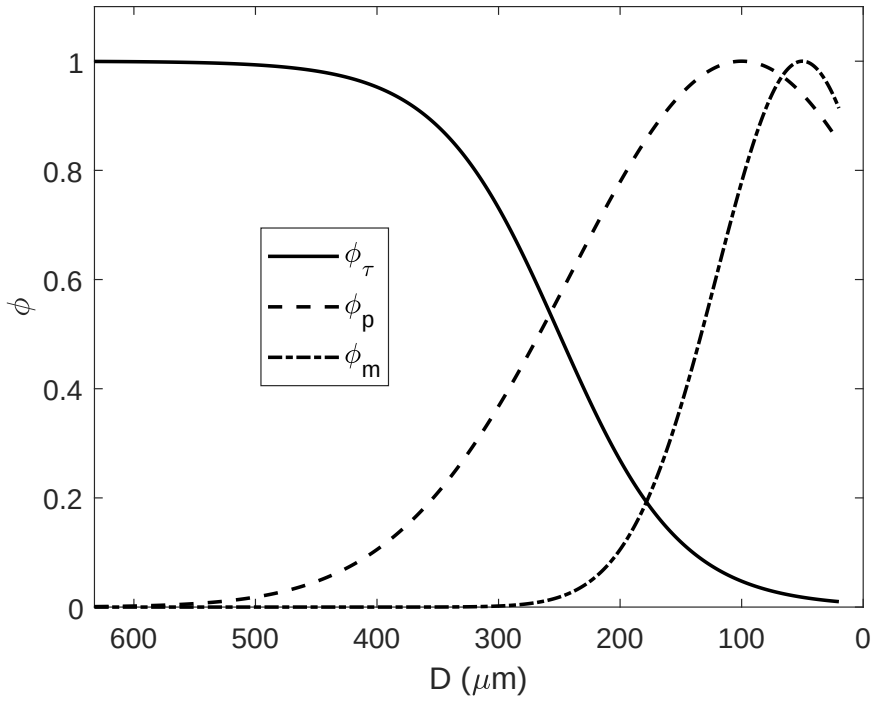

Figure 4.1: The effectiveness of each regulation mechanisms, based on the analyses of [113, 114, 117, 118, 135].

(ENDO/EPI) is assumed to be ∼1.25 [97]. The prescribed intramyocardial pressures (p_{im}) are 47 and 13 mmHg imposed on subendocardial and subepicardial vessels, respectively.

Viscosity - Pries and colleagues [149] observed that the viscosity in the systemic vasculature is dependent on the size of the vessel and the hematocrit level (H_D). Particularly, the variation of viscosity is more pronounced as the arteries and arterioles become smaller. In our study, we prescribe the viscosity using the following *in-vivo* viscosity law given in [149]

$$C = \big(0.8 + \exp(-0.07D)\big)\big(-1 + \frac{1}{1+10^{-11}D^{12}}\big) + \frac{1}{1+10^{-11}D^{12}}, \tag{4.12}$$

$$h_f = \frac{(1-H_D)^C - 1}{(1-0.45)^C - 1}, \tag{4.13}$$

$$\mu_{0.45} = 6\exp(-0.085D) + 3.2 - 2.44\exp(-0.06D^{0.645}), \tag{4.14}$$

$$\mu_{vivo} = \mu_0\big(1 + h_f(\mu_{0.45}-1)(\frac{D}{(D-1.1)})^2\big)(\frac{D}{(D-1.1)})^2, \tag{4.15}$$

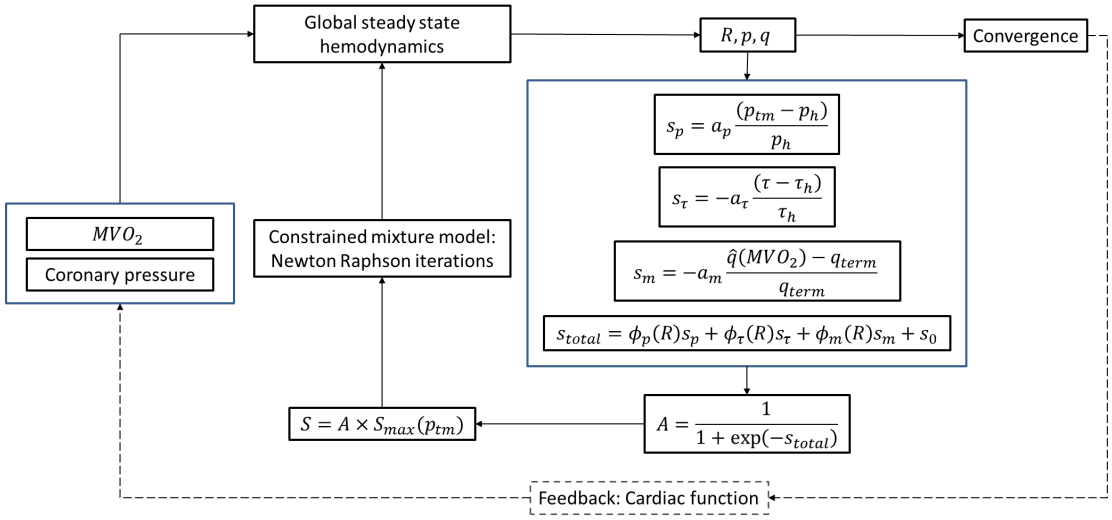

Figure 4.2: Schematic diagram illustrating the workflow of the simulations, with possible extension to a closed-loop model. The inputs are the coronary pressure (p_{in}) and MVO_2. The convergence defines the equilibrium state of the flow regulation. The feedback mechanism (not included in the current study) relates the local flow regulation in coronaries to the cardiac function; heart rate, cardiac output, etc.

Table 4.1: Model parameters for the homeostatic optimization

Parameter description		**Reference**
Extended Murray's law		
Metabolic cost of collagen and SMC	1070 W/m^3	[167]
Metabolic cost of blood supply	51.7 W/m^3	[168]
Metabolic cost of active tension	0.00872 $1/s$	[166]
Wall density	1060 kg/m^3	
Hemodynamics and geometry		
Flow at the outlet arterioles (subendocardium)	0.002 mm^3/s	[116, 187]
Inlet pressure	100 mmHg	[86]
Pressure at the outlet arterioles	55 mmHg	[186]
Hematocrit level (H_D)	0.45	[135]
Blood density	1060 kg/m^3	
Plasma dynamic viscosity μ_0	0.001 Pa.s	[149]
Length-to-radius relation (LAD)	$L = 0.145D + 20$ μm	[24, 86]

where D is the anatomical diameter in micron, and μ_0 is the viscosity of the blood plasma.

Vascular wall properties - Similar to Chapter 3, the basal and tension dependent metabolic cost of SMCs are adapted from energetic considerations of the vascular smooth muscle in swine coronary arteries [167]. To estimate the constitutive parameters for each constituent in the arterial wall, the vessel segments in the myocardial arterial trees are subdivided into four classes: small arteries ($D \geq 190\ \mu m$), large arterioles ($100 \leq D < 190\ \mu m$), intermediate arterioles ($50 \leq D < 100\ \mu m$), and small arterioles ($D \leq 50\ \mu m$), based on the classifications in [102, 135]. In the biomechanical study of the microvasculature, two factors must be considered; First, under physiological condition, the extracellular matrix components in the arteriolar wall are in a state of compression whereas SMCs are contracted to exert tone [112]. Moreover, a microscopic analysis of the mechanical structure of rabbit's arterioles has shown that the amount of SMCs gradually decrease from arterioles of $100\mu m$ to $30\mu m$ [188]. Therefore, the intrinsic passive and active mechanical properties of the constituents (i.e., collagen fibers, elastin, and SMCs) are assumed to be constant across all four classes in the current study. Consequently, we estimate the mechanical properties, prestreches and mass fractions using the pressure-diameter relationships in [102, 135]. Figure 4.3 shows the diameter-pressure relationship for passive and fully-constricted representative vessels in the myocardial layers. Furthermore, the mass fractions are estimated, as shown in Fig. 4.4. The mechanical parameters are kept constant in the homeostatic optimization. However, the basal activation level of the muscle tone (via parameter s_0) is considered as a variable which is used to match the vessel thickness-to-diameter ratio from the optimization results with those reported in the literature [144].

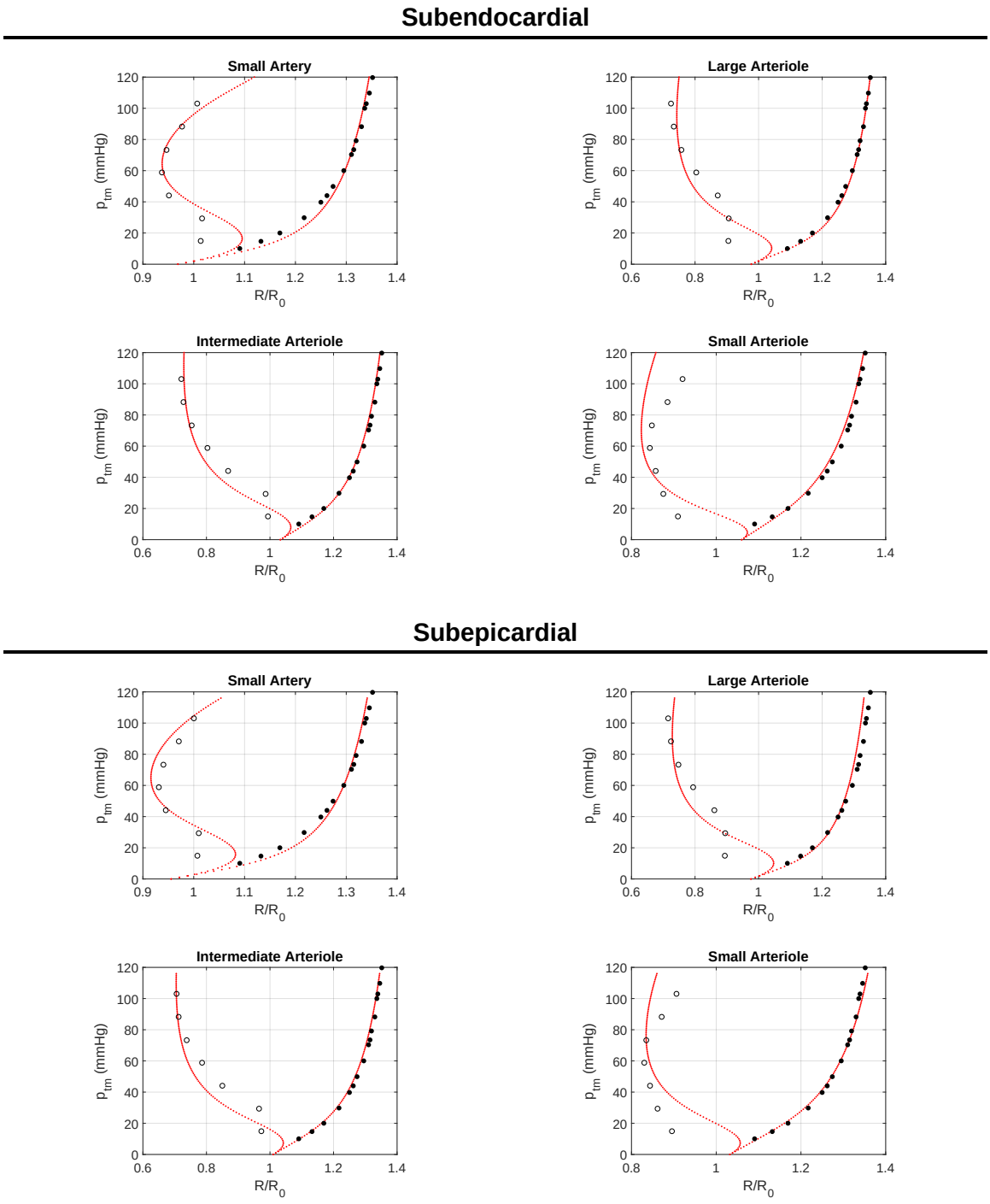

Figure 4.3: Solid circles show the passive behavior of the vessels, digitized from data in [135]. Open circles show the fully activated response of the arteries. Red dots are the estimated response from fitted parameters. (R_0: the radius at zero pressure)

Table 4.2: Estimated constitutive parameters for the constrained mixture model of the arteries

Parameter description	
Passive material parameters	$c_1 = 113.60$ Pa/kg, $c_2 = 333.70$ Pa/kg, $c_3 = 4.64$, $\alpha^k = 0, \pm 45°, 90°$ $c_4 = 78.02$ Pa/kg, $c_5 = 0.47$
Active material parameters	$S_0 = 2.45$ Mpa, $p_0 = 70$ mmHg, $\beta = 2.1$ $\lambda_0 = 0.5$, $\lambda_M = 1.7$
Subendocardium pre-stretches (A,LA,IA,SA)*	$G^e_\theta = G^e_z = (1.15, 1.12, 1.00, 0.96)$ $G^k_h = (1.02, 0.99, 0.94, 0.9)$ $G^m_h = (1.05, 1.05, 1.05, 1.02)$
Subepicardium pre-stretches (A,LA,IA,SA)*	$G^e_\theta = G^e_z = (1.22, 1.12, 1.06, 1.06)$ $G^k_h = (1.05, 1.04, 0.97, 0.92)$ $G^m_h = (1.05, 1.05, 1.05, 1.05)$

*A: Arteries, LA: Large, IA: Intermediate, SA: Small arterioles.

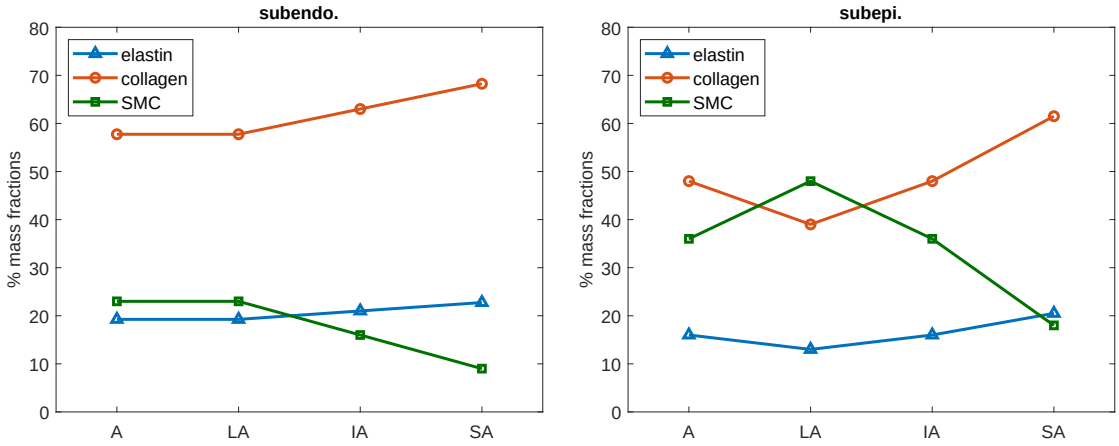

Figure 4.4: Estimated mass fractions for the arteries and arterioles of different layers. (A: Small arteries, LA: Large, IA: Intermediate, SA: Small arterioles.)

4.3 Results and discussion

4.3.1 Baseline optimization

Figure 4.5 shows the diameter and radius exponent as results of the optimization. Subendocardial blood vessels appear to be larger than their subepicardial counterparts. This dif-

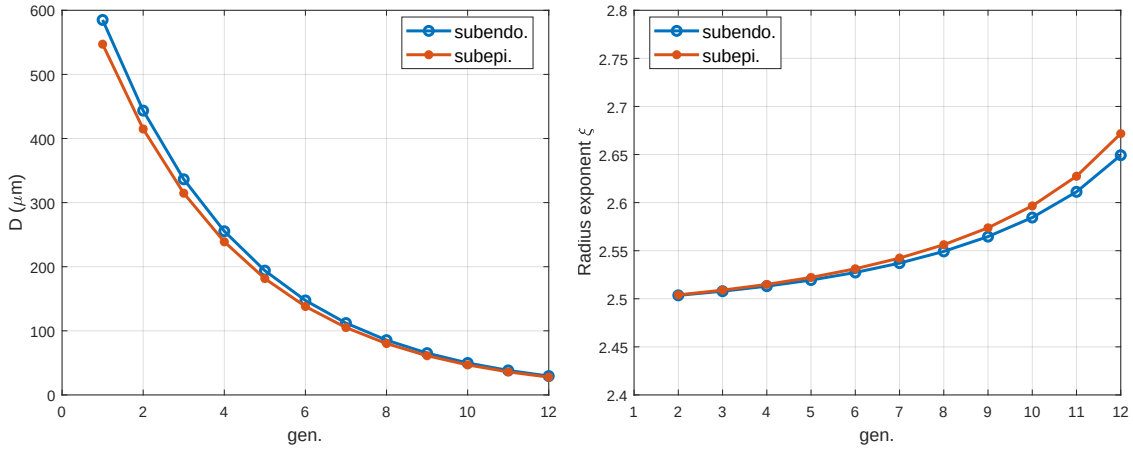

Figure 4.5: The baseline optimization results plotted along with the generation number: Left: diameter distribution; Right: radius exponent in daughter-to-parent radii relation ($R_p^\xi = R_{d1}^\xi + R_{d2}^\xi$).

ference, consistent with experimental and simulation results from [88, 133], is due to higher blood perfusion in the subendocardial layer. Furthermore, the optimization results in increasing radius exponent ξ (2.5-2.7) with the generation number, for the blood vessels from 600 μm to 25 μm. The original Murray's law predicted a cubic radius exponent. However, several experimental studies on the morphometry of vascular trees have shown varying ξ between 2 in larger vessels to near 3 in precapillary level [85, 86, 189, 189, 190]. Arts and Reneman [182] studied the the scaling laws in dog's coronary vasculature and showed an exponent of 2.55 for the vessel distal segments with 400 μm diameter. Suwa and coworkers [190] showed an exponent of 2.7 by analyzing different vasculature in several organs in human body. Nevertheless, the radial exponent from our optimization result is consistent with those experimental studies.

Figure 4.6 shows the structural and hemodynamics results of the optimization. The optimization framework is able to capture the experimental thickness-to-diameter ratio ([144]) by slight modification of the basal active tone (within 10% of the estimated activation). Top left panel of Fig. 4.6 shows the performance of the optimization in this regard. Most of the

coronary vascular resistance is located in arterioles of smaller than 100 μm. This range seems to be the constant across different organs and different species (Fig. 4.6). Similarly, Van-Bavel and Spaan [191] showed that the pressure in the coronary microvasculature drops from 90 to 30 mmHg in the small vessels of 10-μm order. On the other hand, the wall shear stress increases almost 4-fold in the arterioles, consistent with experimental studies. In particular, Stepp and colleagues [118] analyzed τ in canine coronary microvasculature and observed that arterioles of <160 μm have an elevated level of shear stress. In summary, the hemodynamics results, wall shear stress and pressure, fit the available data on the microcirculatory system in a quantitative and qualitative manner.

Furthermore, the bottom-right panel of Fig. 4.6 shows homeostatic circumferential stress, which is computed from Laplace's law ($\sigma_h = \frac{p_{tm}R}{H}$) where H is the *in-vivo* thickness. Therefore, since the intramyocardial pressure is lower towards the epicardium (higher transmural pressure), the subepicardial homeostatic stress is larger. Guo and Kassab [194] analyzed the circumferential stress in the swine coronary arterial tree and reported the circumferential stress in the range of 9.4-159 kPa for arteries of 9.8-3097 μm. Although we captured the same trend, the values from our simulation do not completely match with those of their study. This discrepancy may be attributed to the fact that their hemodynamics analysis was conducted in an arrested heart where the vascular transmural is equal to the luminal pressure (i.e., no intramyocardial pressure). In a more recent study, Choy and Kassab [145] evaluated the medial and intimal thickness in coronary arterial trees and observed that the thickness in subendocardial layer is lower than the thickness in subepicardial layer, which leads to a higher diastolic circumferential stress ($p_{im} = 0$). It is worth noting that the aforementioned studies were conducted on vessels without a significant SMC tone.

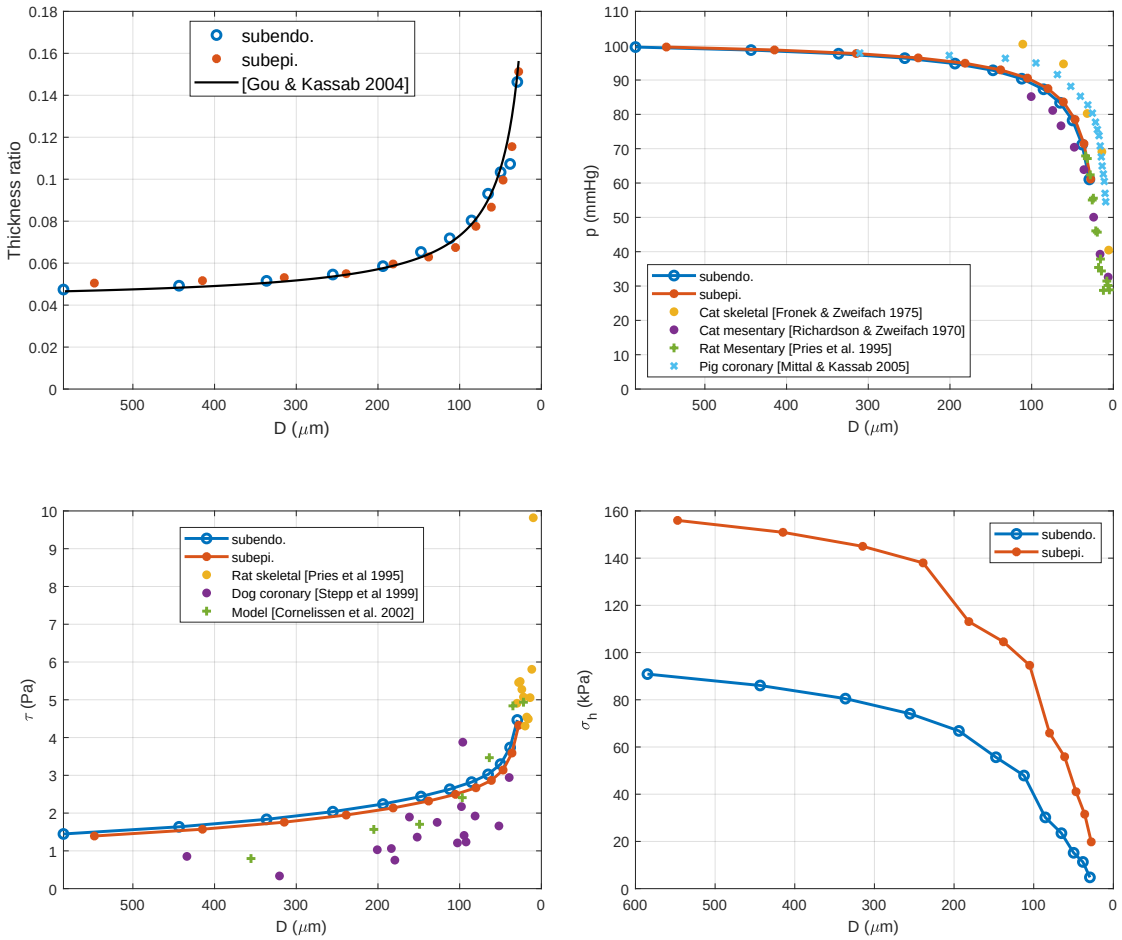

Figure 4.6: Homeostatic optimization results plotted against diameters: Top-left: wall thickness-to-diameter ratio in unloaded configuration [144]; Top-right: mid-artery pressure [86, 186, 192, 193]; Bottom-left: homeostatic value of wall shear stress (τ) [118, 135, 186]; Bottom-right: homeostatic value of circumferential stress σ_h.

4.3.2 Autoregulation

Before presenting the results for the coronary flow regulation, it should be noted that the outlet pressure prescribed in the homeostatic optimization is at the precapillary arterioles. To enhance the fitting for the range of coronary flow in the arterial tree, we add lumped parameters with constant resistance at the end of each arterial tree segment and prescribe the venous pressure 20 mmHg as the outlet pressure boundary condition of the tree. To calibrate

Table 4.3: Estimated control parameters for the autoregulatory response.

Parameter	Subendocardial	Subepicardial
a_p	0.32	0.23
a_τ	1.30	1.10
a_m	0.50	1.5

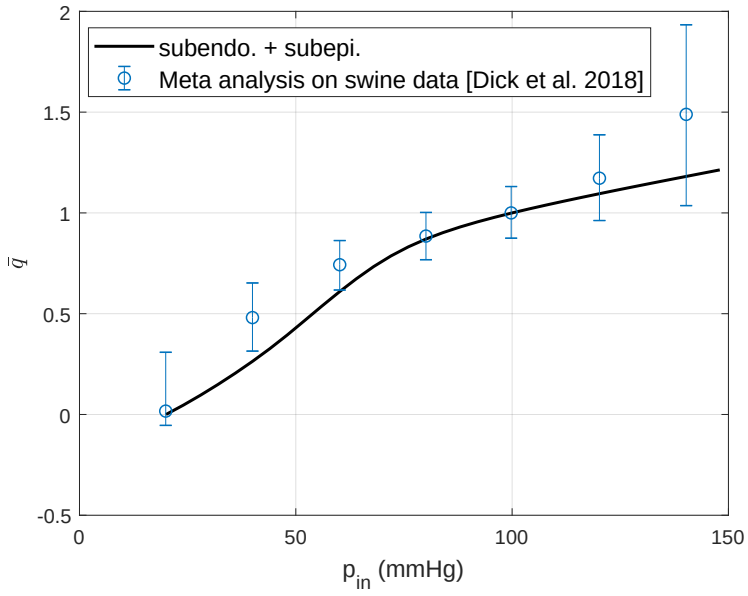

Figure 4.7: Pressure-flow autoregulation in the combined trees compared to the collected experimental data in [103]. The flow is normalized ($\bar{q}$) against the flow at $p_{in} = 100$ mmHg.

the controlling parameters, a_p, a_τ, and a_m, we used the pressure-flow autoregulation data collected in [103]. The estimated controlling parameters are presented in Table 4.3.

Figure 4.7 shows the estimated autoregulatory response of the coronary vasculature as the average of the response in subendocardial and subepicardial layers. Our model fits the experimental observations capturing the essential features of the autoregulation in range of inlet coronary pressures 70-140 mmHg. However, in the lower inlet pressures (20-50 mmHg) the flow rate predictions are on average 20% lower than the experimental measurements. In this range, the model predictions of pressure-flow curve is bounded by the fully dilated (passive) response of the arteries. Thus, the scarcity in the range and number of available

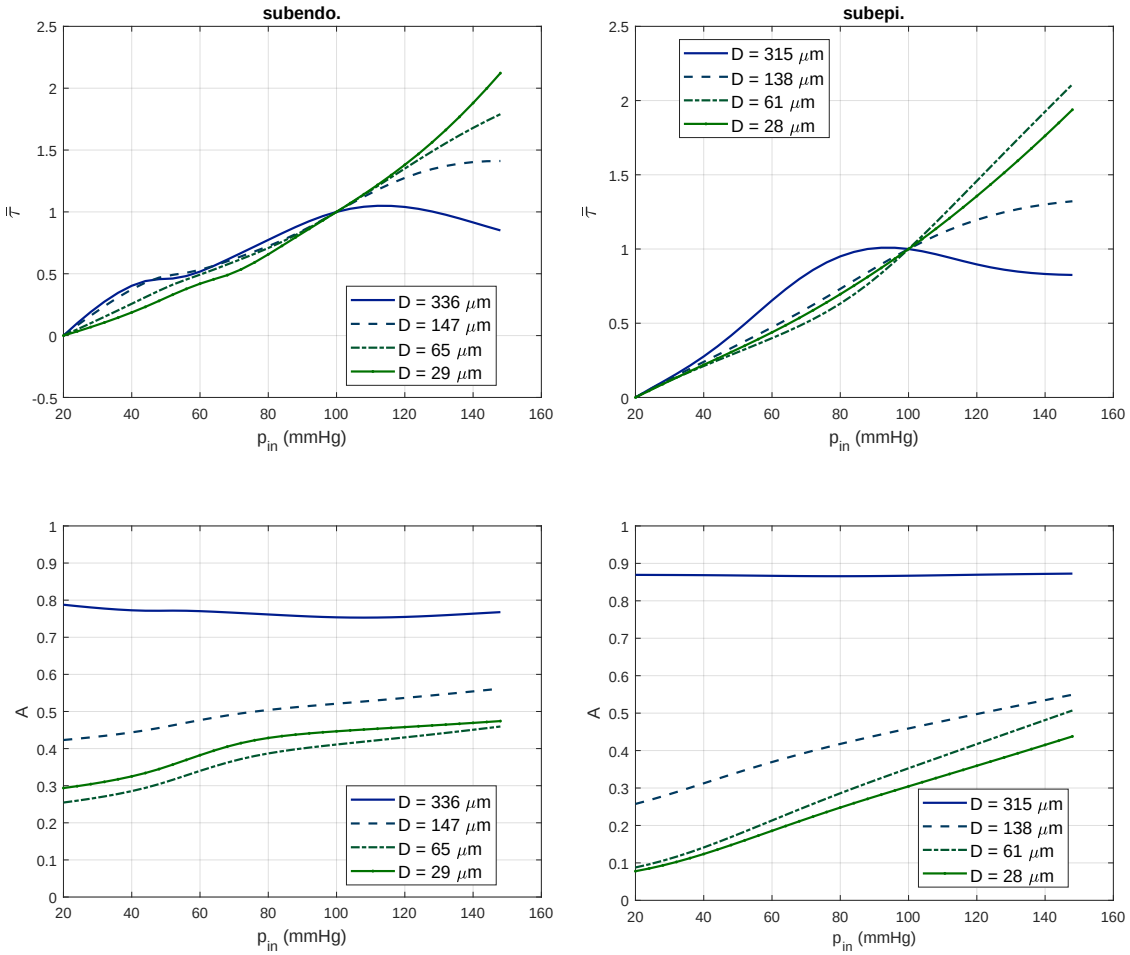

Figure 4.8: The predicted dependence of wall shear stress and activation on the mean inlet pressure. Wall shear stress in each vessel is normalized ($\bar{\tau}$) against its value at $p_{in} = 100$ mmHg.

data on pressure-diameter relationships could be a contributing factor in this discrepancy.

A detailed analysis of the hemodynamics of the arterial trees is necessary in understanding the heterogeneous interaction between different mechanisms in the coronary flow autoregulation. Figure 4.8 shows the normalized wall shear stress ($\bar{\tau}$) and the activation level for four vessels in the layers of the myocardium. Clearly, since the mechanism controlling the shear is almost fully ineffective in the smallest vessels, wall shear stress does not show any significant regulation in the small and intermediate arterioles [118]. The arteries, however,

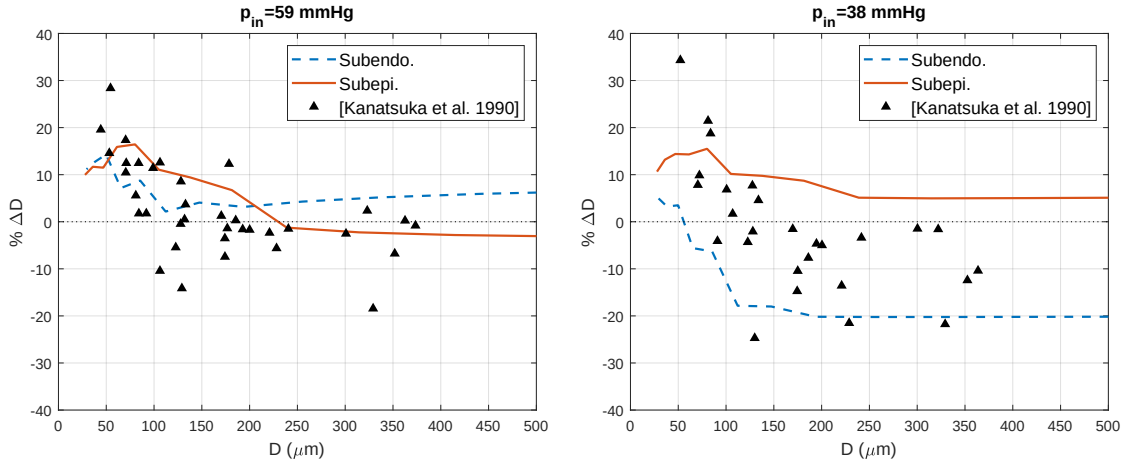

Figure 4.9: The effects of pressure reduction on coronary arterial microvessels compared to the experimental observations on epicardial microvasculature in dogs [114].

exhibit notable of regulation of wall shear stress around the baseline pressure.

Activation levels (a marker of vasoconstriction) in the arterioles monotonically increase from low to high inlet pressures. This is expected, since the myogenic and metabolic mechanisms simultaneously play dominant roles in autoregulation [195, 196]. Furthermore, the arterioles of the subepicardial layer seem to be more sensitive to changes in pressure and show a greater variability in the activation level. Alternatively, the activation level in large vessels remains almost constant, exhibiting no significant response to changes in the coronary pressure.

To identify the location of the autoregulation in swine coronary arteries, two cases of pressure reduction are considered. When the coronary pressure was mildly reduced, the vessels smaller than 150 μm were dilated whereas the large vessels almost remained in their homeostatic value. Moreover, the magnitude of dilation was intensified with severely reducing the inlet pressure, $p_{in} = 38$ mmHg, while the larger vessels showed some degree of constriction. Similar results was observed in a study by Kanatsuka et al. [114] on the epicardial coronaries of dogs. However, a direct quantitative comparison might not be accurate due to the interspecies differences in the coronary physiology.

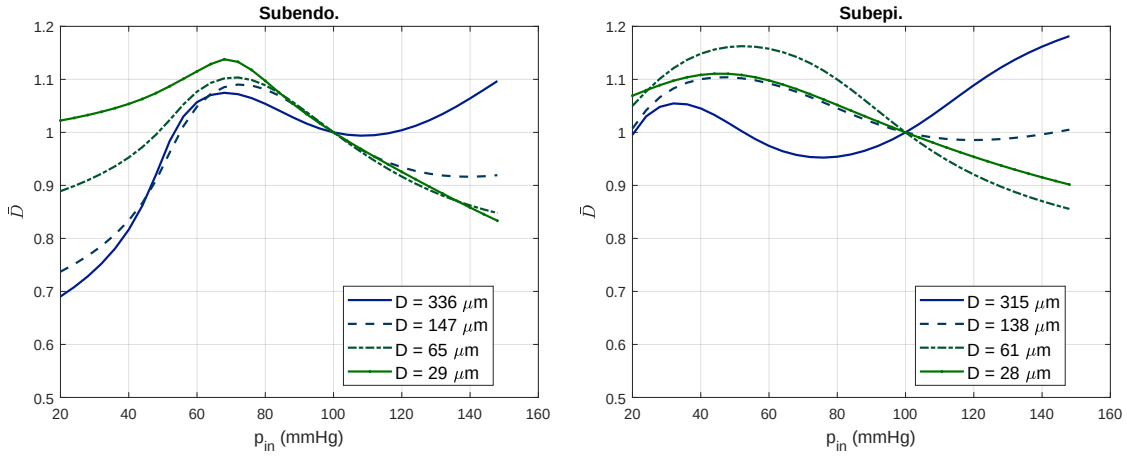

Figure 4.10: Diameters as functions of p_{in} for different vessels of subendocardial and subepicardial layers.

It is worthy to note that the extravascular pressures acting on vessels embedded in the layers of myocardium are significantly different (13-47 mmHg). Particularly, the subendocardial p_{tm} is negative in large parts of the arterial tree when p_{in} is low. Consequently, the subendocardial activation of the SMCs is delayed compared to the subepicardial layer. This discrepancy between location of dilated diameters leads to an increase of ENDO/EPI in $p_{in} = 75$ mmHg. A dilation of the arterioles followed by a constriction has been observed in autoregulation of other circulatory systems [109].

Alternatively, differential autoregulatory response of the arteries to a change in pressure are analyzed in terms of ENDO/EPI (Fig. 4.11). Normal ENDO/EPI blood flow ratios have been reported between 1.09 to 1.49 across different species [97]. The model, however, shows that with a severe reduction of pressure (p_{in} <60 mmHg), the ENDO/EPI ratio reduces to below one. The inset in Fig. 4.11 shows a similar trend observed in the transmural analysis of autoregulation in canine coronary circulation [197]. Similarly, the experiments by Ball and Bache [198] showed a 50%-60% decrease in the ENDO/EPI ratio in canine LV as a result of mild-severe obstructions in large coronary arteries.

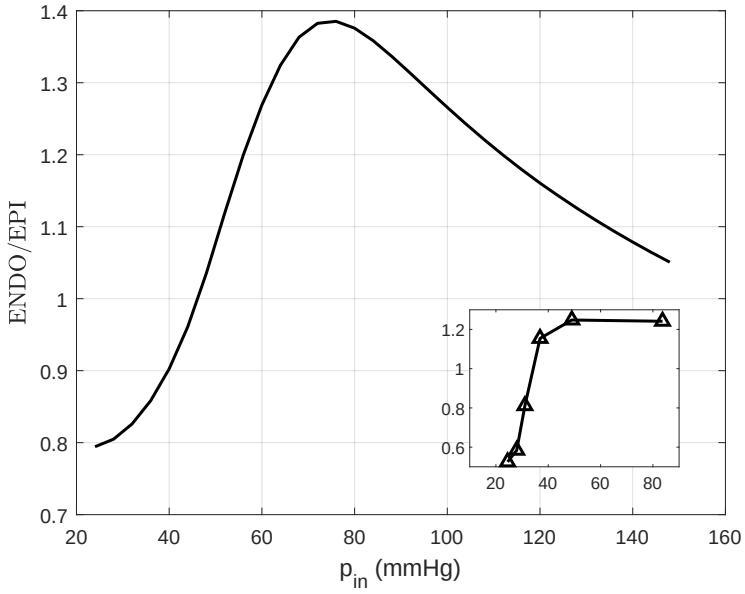

Figure 4.11: The predicted transmural distribution of the flow during pressure-flow autoregulation. The inset shows the observations in dogs, from [197].

4.3.3 Effects of adenosine and NO inhibitors

To evaluate the prediction capabilities of the model, administration of adenosine and inhibition of NO production are parameterically modeled in this section (Fig. 4.12). Adenosine is a metabolic vasodilator which mostly affects the downstream coronary microvessels [102]. The adenosine administration is modeled by setting the arteriolar activation to zero ($A = 0$). Alternatively, the inhibition of NO is modeled via 1) almost full constriction of small arteries, due to inhibition of shear-dependent vasodilation, and 2) utilization of the full vasodilatory capacity in the arterioles. The former is justified by considering the fact that in the small arteries, τ is the only mediator of vasodilation. The absence of this dependency (via inhibition of NO) leads to full SMC tone in small arteries. The latter, however, is justified by the experimental observation in epicardial coronaries of dogs, in the work of Jones et al. [199]. In fact, they observed that an inhibition of NO synthesis obstructs further dilation as a result of

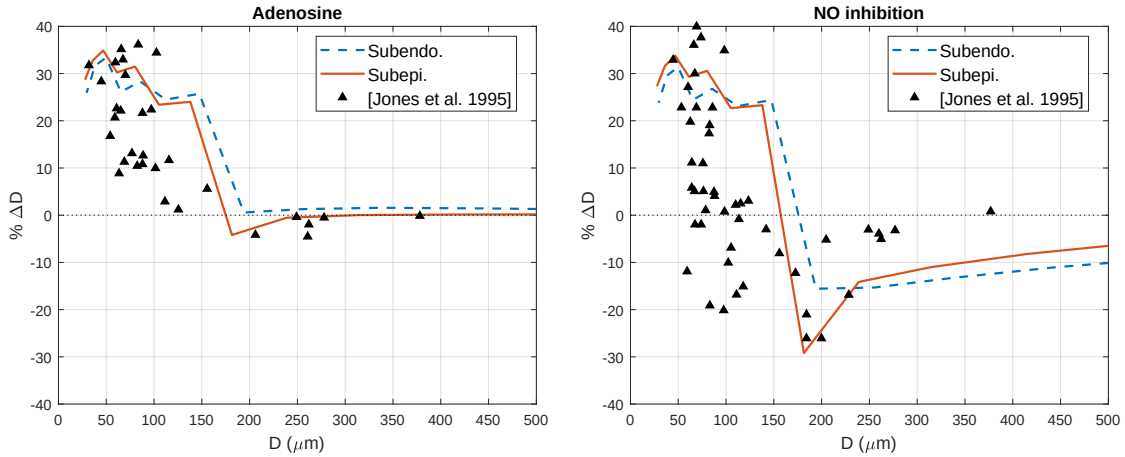

Figure 4.12: The effects of adenosine infusion and NO inhibition on coronary arterial microvessels compared to the experimental observations on epicardial microvasculature in dogs [199].

adenosine administration. It is worthy to mention that infusion of such exogenous agents did not significantly change the coronary pressure. Figure 4.12 shows a fair agreement between our simulation results and the experimental observations. However, it should be noted that our model relies on the data from swine myocardial vessels while the observations are from canine epicardium.

4.4 Summary and conclusion

In this chapter, the homeostatic optimization framework of Chapter 2 was employed to estimate the baseline characteristics of coronary arterial tree. Diverse experimental data of swine coronaries were integrated to construct two arterial trees located in subendocardial and subepicardial layers of the myocardium. Consequently, the estimated homeostatic state of the arterial trees was used to construct a constrained mixture model for the coronary flow regulation.

The implemented mechanical model was calibrated against pressure-diameter available data

in the literature. Our parameter estimation indicated that upon the *in-vivo* level of SMC tone, the collagen fibers and elastin are virtually in a compressed state in the coronary arterioles. Moreover, the estimated mass fractions of the SMCs justify the heterogeneity of the active response across the arterial tree. In addition, the relative myocardial depth of blood vessels seems to be a contributing factor in establishing their baseline mechanical properties.

Our computational predictions showed excellent congruity compared to the data from observations in the microcirculatory networks, both quantitatively and qualitatively. Previous modeling efforts in coronary flow regulation were based on the *ex-vivo* observations of the active responses of the arteries. The physiological flow regulation in the coronary vasculature, however, greatly relies on the deviations from basal quantities such as pressure and wall shear stress. Therefore, one of the contributions of our model is estimating the basal conditions for the flow control mechanisms.

The constructed arterial trees were used to study the flow regulation, specifically pressure-flow autoregulation in distal coronary arterial network. To the author's knowledge, this is the first implementation of a constrained mixture model to coronary arterial trees. This implementation enhances the prediction capability for coronary flow regulation as well as arterial function and vascular adaptation. This study illustrated that the model was capable of capturing the essential flow-pressure relationship in the autoregulation of coronary arteries. Furthermore, we were able to perform an differential analysis of the size-dependent and transmural heterogeneity of the autoregulatory response. The model highlighted that the autoregulation occurs mostly in the level of coronary arterioles whereas shear regulation is dominant only at the level of arteries. In addition, we observed that the range of dilation and constriction of vessels is a function of their relative depth within the myocardium. Furthermore, we used computational simulations of adenosine infusion and inhibition of NO production and compared the results with available experimental data.

The present study has several limitations. First, the computational model is not yet fully validated by well-controlled animal experiments. Particularly, the information on the pressure-diameter relationship of vessels inside the myocardium is still scarce. In this study, we used the relationships from epicardial and subepicardial vessels for parameter estimations of the mechanical model. Moreover, the available pressure-diameter data extend to the vessels of around 50 μm, while a great portion of the coronary vascular resistance resides in smaller vessels (terminal arterioles). More data on arterioles smaller than 50 μm will enhance the prediction capability of the model. In addition, we did not include the tethering of the arterioles to the myocardium in our model. Although as proposed by Young et al. [200], the small arterioles can freely constrict, the dilation of vessels might be limited by their tethering to myocardium. Regardless, the two-way tethering of the myocardium and coronary arteries is not fully understood, yet. Furthermore, our analysis is limited to the averaged steady state of the vasculature, while the hemodynamics of the coronary arteries is highly dependent on the systolic and diastolic phases. As a matter of fact, most of the subendocardial flow has been shown to occur during the diastolic phase where the myocardial pressure vanishes. While our analysis showed that an application of an analytical 1D theory (see Chapter 3) to coronary hemodynamics is not physically realistic, the current model can be endowed with a non-linear finite element model of the arterial tree to overcome this limitation. Lastly, an open loop analysis of the metabolic regulation, as was done in this chapter, may obstruct clear interpretation of the interaction of the mechanisms. Therefore, extending the regulation model to include the closed-loop aspects of metabolic vasodilation will improve the capabilities of the model and facilitate the physiological interpretations.

Chapter 5

Conclusion and Future Work

5.1 Conclusion

In this dissertation, we described a novel computational framework for multiscale biomechanical modeling of vascular adaptations in arterial networks. The principle of minimum metabolic energy consumption with local important mechanical homeostatic values was successfully implemented in modeling the architecture of vascular networks. Such a model provides the general workflow of G&R in an arterial network and establishes a baseline which is substantial in the G&R studies of the onset and progression of many vascular diseases.

The model developed in this dissertation constructs arterial trees via an extension of Murray's law which provides a tight coupling of the hemodynamics and the arterial wall mechanics. Furthermore, each individual vessel in the network is endowed with a constrained mixture model which paves the way for multiscale modeling of stress-mediated mass production and removal during growth and remodeling of arterial trees. Our model relies heavily on available data from the literature and provides a uniform framework in which data from different studies (i.e., hemodynamics, morphometric, structural, etc.) are integrated in a

biomechanically consistent manner. Moreover, since most the available data are recorded in external environment, another novelty of our model is in predicting the *in-vivo* geometry and properties of the vasculature which is difficult, if not impossible, to measure.

We have shown implementations of the framework to study mutliscale vascular phenomena. The first application was to estimate the homeostatic baseline characteristics of pulmonary arterial trees. The framework produced an estimation of important properties of the distal vasculature such as homeostatic mass fractions, constituent-wise stresses, and steady state hemodynamics. Such properties are essential in the study of stress-mediated growth and remodeling of the distal vasculature, which is a prominent feature of the early stages of PAH. We also illustrated the capability of the model in FSG simulation via a one-way coupling of the results of homeostatic optimization with pulsatile hemodynamics. The equivalent input impedance was also computed for the distal vessels which can be used for patient-specific modelings of pulmonary arterial hemodynamics.

Second, we highlighted the versatility of the model by an implementation of the model to study the of coronary flow regulation. We used two myocardial arterial sub-trees, distally located to the LAD and inside the left ventricle. The myocardial-vascular interactions were included in our model via consideration of average interstitial fluid pressure and myocyte shortening. Furthermore, we utilized the passive and active pressure-diameter relations from the literature to estimate the mechanical properties, mass fractions of constituents, the basal activation level of smooth muscle cells, and baseline hemodynamics in coronary microvasculature. The results of the baseline optimization demonstrated excellent consistency with the data from the experimental studies. Furthermore, we used the established basal properties to study the pressure-flow autoregulation of coronary arteries. Our model, consistent with experimental data on dogs, showed that the autoregulation mostly occurs in smaller arterioles. Moreover, subendocardial vessels seem to reach full dilation in a larger inlet pressure when compared to the subepicardial vessels. These analyses, coupled with experimental data, are

crucial in identification of the myocardial ischemic susceptibility. We also illustrated the capability of the model in simulating the microvascular response to the introduction of dilatory or constrictive agents.

Although specific limitations of the developed framework in pulmonary and coronary implementations has been already documented in Section 3.4 and 4.4, it is worthy to highlight a few remarks on general limitations in the computational method that can be considered for further investigation. First, the current study of optimization was operated using previous references of smooth muscle cell metabolic costs, which did not take into account of the other constituents. Therefore, a systematic parameter sensitivity study needs to be conducted to distinguish the main sources of uncertainties in the modeling framework. Such analysis will be crucial in calibration and validation of the model against experimental observations. Second, the structure of the tree in this study is based on generations and bifurcations (inspired by fractal tree idea in [69]) whereas experimental studies describe the morphometry of arterial networks based on ordering methods (e.g., Strahler ordering method). This disparity may hinder a global comparison of the morphometry of the generated tree with the experimental studies. Our modeling framework, however, can be applied to the pre-constructed arterial networks for diameter assignment and hemodynamics as indicated in the next section.

5.2 Future work

Additional experimental data on the structure of the proximal and distal vessels (i.e., thickness and mass fractions of constituents), morphometry of the arterial trees, energetic considerations of the vascular wall, etc. are required for validation and/or calibration of the model. With more availability in human data, the framework can be implemented on arterial networks which are representatives for human subjects, healthy or affected by disease.

Morphometric studies on the structure of arterial networks were conducted on dissected vasculature where the properties of the arterial tissue might have altered (e.g., no vasoactive tone). Therefore, the main limitation of such studies was their inability to predict the *in-vivo* diameters of vessel segments whereas the presented framework is capable of model-based diameter re-calibration in such analyses. This will greatly improve the current knowledge of the microvascular networks and enhance the accuracy of modeling studies. Alternatively, endowing our model with "volume-filling" or "avoidance" algorithms are other possible extension of the model that may be explored.

Womersley's solution is capable of simulating the pulsatile hemodynamics in a physiologically realistic manner. The main advantage of implementation of this theory is the computational and algorithmic simplicity. Nonlinear finite element models, however, can enhance the mechanical analysis by including biomechanical complexities such as nonlinearity of the vascular wall and/or extravascular forces (e.g., intramyocardial pressure). The results of the proposed framework can be directly used in a non-linear 1D finite element model for detailed analysis of pulsatile hemodynamics and extensions to FSG.

We established the homeostatic baseline for the pulmonary arterial network in Chapter 3. Consequently, our model enables us to study long-term pathological conditions in PAH such as inflammation and proliferation of SMCs, remodeling of extracellular matrix etc. Furthermore, the model facilitates *in-silico* experiments on introduction external stimuli such as vasodilation (via NO inhalation [201]), elastase inhibition (via elafin [202]). Similarly, the distal pathological conditions of the microvasculature in obstructive and non-obstructive CAD can be studied. Alternatively, the model can be employed to study cardiac allograft vasculopathy (CAV) where the distal remodeling is pronounced by endothelial dysfunction, inflammation, and intimal thickening.

In closing, the main goal of this dissertation, to develop a framework to embed the G&R in multiscale arterial networks, has been achieved. We anticipate that our framework paves the

way for future studies of vascular G&R in characteristically multiscale problems. Utilization of such computational models is substantial in understanding the onset and progression of diseases and advancing new therapies for their management.

APPENDICES

APPENDIX A: Formulation of small on large theory

The theory of small deformations superimposed on large (namely 'theory of small on large' (SoL)) has been well formulated in 1950-60s [203–205]. Only recently, however, the SoL was reformulated to link model the pulsatile deformations *in vivo* [5, 160]. This theoretical tool hence serves as a useful tool to obtain a linearized response of wall during the cardiac cycle without compromising important mechanical characteristics such as anisotropy and smooth muscle tone. However, the prior formulation of SoL was still not fully understood in order to provide a solid theoretical foundation in vascular mechanics. Particularly, the prior SoL formulation adopted a Lagrange multiplier approach as many studies have regularly done for biological continuum-mechanics problems. However, Baek and Srinivasa [206] illustrated that constraints prescribed by the Lagrange multiplier could obscure the physical interpretation of mathematical operations, for instance, when taking the second derivatives of the energy functions for deriving bulk modulus and specific heat. Likewise, this Lagrange multiplier approach may impede a clear physical interpretation of SoL application on vascular mechanics [207].

Preliminaries

Let the motion of a solid-like body $\mathcal{B}$ be represented by mappings χ of a particle from a reference configuration $\kappa_R(\mathcal{B})$ at time t,

$$\mathbf{x} = \chi(\mathbf{X}, t), \tag{A.1}$$

where $\mathbf{X}$ and $\mathbf{x}$ are position vectors with respect to the reference and current configurations. Furthermore, we consider the body occupies a configuration $\kappa_0(\mathcal{B})$ with the position vector $\mathbf{x}_0 = \chi(\mathbf{X}, t_0)$ which is characterized by a large deformation measured from the reference

configuration. Thus, the deformations of the body consist of two consecutive parts: a small displacement, $\mathbf{u} = \mathbf{u}(\mathbf{x}_0, t)$, superimposed upon the large deformation. Therefore, the current position of a particle can be written as

$$\mathbf{x} = \mathbf{x}_0 + \mathbf{u}(\mathbf{x}_0, t). \tag{A.2}$$

Therefore, deformation gradients associated with mappings from the reference configuration to the intermediate and current configurations are

$$\mathbf{F}^o = \frac{\partial \chi(\mathbf{X}, t_0)}{\partial \mathbf{X}}, \quad \mathbf{F} = \frac{\partial \chi(\mathbf{X}, t)}{\partial \mathbf{X}}. \tag{A.3}$$

Similarly, for the small deformations we can define

$$\mathbf{F}^* = \frac{\partial \mathbf{x}}{\partial \mathbf{x}_0} = \mathbf{I} + \mathbf{H}, \quad \mathbf{H} = \frac{\partial \mathbf{u}}{\partial \mathbf{x}_0}, \tag{A.4}$$

where

$$\mathbf{F} = \mathbf{F}^* \mathbf{F}^{\mathbf{o}}. \tag{A.5}$$

In linear elasticity, the symmetric and skew-symmetric parts of $\mathbf{H}$ can be expressed as

$$\epsilon^* = \frac{1}{2}\big(\mathbf{H} + \mathbf{H}^T\big), \tag{A.6}$$

$$\mathbf{\Omega}^* = \frac{1}{2}\big(\mathbf{H} - \mathbf{H}^T\big), \tag{A.7}$$

where ϵ and $\mathbf{\Omega}^*$ are the infinitesimal strain and infinitesimal rotation, respectively. The Cauchy stress can be written in terms of the deformation gradient and the second Piola-

Kirchhoff stress $\mathbf{S}$ with respect to the reference configuration

$$\mathbf{T} = J^{-1}\mathbf{F}\mathbf{S}\mathbf{F}^T, \quad \mathbf{S} = 2\frac{\partial W}{\partial \mathbf{C}}, \tag{A.8}$$

where $J = \det(\mathbf{F})$, and W is the stored strain energy function as a function of $\mathbf{C} = \mathbf{F}^T\mathbf{F}$. The second Piola-Kirchhoff stress $\mathbf{S}^*$ with respect to the intermediate configuration $\kappa_0(\mathcal{B})$ can be expressed as

$$\mathbf{S}^* = J^{o-1}\mathbf{F}^o\mathbf{S}\mathbf{F}^{oT}, \tag{A.9}$$

where $J^o = \det(\mathbf{F}^o)$. Using a push forward operation, the Cauchy stress can be written as

$$\mathbf{T} = J^{*-1}\mathbf{F}^*\mathbf{S}^*\mathbf{F}^{*T}, \tag{A.10}$$

where $J^* = \det(\mathbf{F}^*)$.

Let Cauchy stress in any convenient intermediate configuration be represented by $\mathbf{T}^o$ whereas that in any current configuration be denoted as $\mathbf{T}$. We can write the incremental stress as $\Delta\mathbf{T} = \mathbf{T} - \mathbf{T}^o$. Therefore, we are seeking an elasticity tensor connecting $\Delta\mathbf{T}$ and the ϵ^*.

To derive an expression for the incremental stress response in the small deformation, we use equations A.4 and A.10 to get the relation

$$\mathbf{T} = \frac{1}{J^o}\{\det(\mathbf{I}+\mathbf{H})\}^{-1}(\mathbf{I}+\mathbf{H})\mathbf{F}^o\big(\mathbf{S}^o + \frac{\partial \mathbf{S}}{\partial \mathbf{C}}\Big|_{\mathbf{C}^o}\mathbf{C}^*\big)\mathbf{F}^{oT}(\mathbf{I}+\mathbf{H})^T, \tag{A.11}$$

where the right Cauchy-Green tensor $\mathbf{C}^*$ is defined as

$$\mathbf{C}^* = 2\mathbf{F}^{oT}\epsilon^*\mathbf{F}^o \tag{A.12}$$

Using the approximation $\{\det(\mathbf{I}+\mathbf{H})\}^{-1} \approx 1 - \mathrm{tr}(\mathbf{H})$ for small $\mathbf{H}$ and neglecting the higher order terms will give

$$\Delta\mathbf{T} = -\mathrm{tr}(\mathbf{H})\mathbf{T}^o + \mathbf{H}\mathbf{T}^o + \mathbf{T}^o\mathbf{H}^T + \mathbf{F}^o \frac{\partial \mathbf{S}}{\partial \mathbf{C}}\Big|_{\mathbf{C}^o} \mathbf{C}^* \mathbf{F}^{oT} \tag{A.13}$$

$$= -\mathrm{tr}(\mathbf{H})\mathbf{T}^o + \mathbf{H}\mathbf{T}^o + \mathbf{T}^o\mathbf{H}^T + 2\mathbf{F}^o \frac{\partial \mathbf{S}}{\partial \mathbf{C}}\Big|_{\mathbf{C}^o} \mathbf{F}^{oT}\epsilon^* \mathbf{F}^o \mathbf{F}^{oT} \tag{A.14}$$

Writing the last term in index notation gives

$$\Delta T_{ij} = -H_{kk}T^o_{ij} + H_{ik}T^o_{kj} + T^o_{ik}H_{jk} + \frac{2}{J^o} F^o_{i\alpha}F^o_{j\beta}F^o_{lp}F^o_{mq} \frac{\partial S_{\alpha\beta}}{\partial C_{pq}}\Big|_{\mathbf{C}=\mathbf{C}^o} \epsilon^*_{lm}. \tag{A.15}$$

Inserting the second Piola-Kirchhoff from equation (A.8) gives

$$\Delta T_{ij} = -H_{kk}T^o_{ij} + H_{ik}T^o_{kj} + T^o_{ik}H_{jk} + \frac{4}{J^o} F^o_{i\alpha}F^o_{j\beta}F^o_{lp}F^o_{mq} \frac{\partial^2 W}{\partial C_{\alpha\beta}\partial C_{pq}}\Big|_{\mathbf{C}=\mathbf{C}^o} \epsilon^*_{lm}. \tag{A.16}$$

Using the decomposition in equations A.6 and A.7, the linearized stress response can be written as

$$\Delta T_{ij} = \mathcal{C}_{ijkl}\epsilon^*_{kl} + \mathcal{D}_{ijkl}\Omega^*_{kl}, \tag{A.17}$$

where

$$\mathcal{C}_{ijkl} = -\delta_{kl}T^o_{ij} + \delta_{ik}\delta_{ml}T^o_{mj} + \delta_{jk}\delta_{ml}T^o_{im} + \frac{4}{J^o} F^o_{i\alpha}F^o_{j\beta}F^o_{lp}F^o_{mq} \frac{\partial^2 W}{\partial C_{\alpha\beta}\partial C_{pq}}\Big|_{\mathbf{C}=\mathbf{C}^o}, \tag{A.18}$$

$$\mathcal{D}_{ijkl} = \delta_{ik}\delta_{ml}T^o_{mj} + \delta_{jk}\delta_{ml}T^o_{im}, \tag{A.19}$$

Finite deformation mechanics of an artery

We assume the arterial wall to be compressible at first, and then incompressiblity is considered as a limit. To this aim, a compressibility term $k(J-1)$ is added to the strain energy

of the artery given in (2.2.2). However, before re-introducing the constitutive relations, let us expand the motion of the artery from a reference configuration to an intermediate configuration as

$$\mathbf{F}^o = \begin{bmatrix} \lambda_r & 0 & 0 \\ 0 & \lambda_\theta & 0 \\ 0 & 0 & \lambda_z \end{bmatrix} \quad \Rightarrow \quad \mathbf{C}^o = \begin{bmatrix} \lambda_r^2 & 0 & 0 \\ 0 & \lambda_\theta^2 & 0 \\ 0 & 0 & \lambda_z^2 \end{bmatrix}. \tag{A.20}$$

We can re-write the strain energy per unit area as

$$w = M_R^e \Psi^e + \sum_k M_R^k \Psi^k + M_R^m (\Psi^m + \Psi_{act}^m) + k(J-1)^2, \tag{A.21}$$

where $J = \det(\mathbf{F})$. Following the formulation in 2.2.2, the deformation gradient mapping each constituent form its natural configuration to the intermediate configuration can be written as

$$\mathbf{F}^{eo} = \mathbf{F}^o \mathbf{G}^e, \quad \mathbf{F}^{k^o} = \mathbf{F}^o \mathbf{G}^k, \quad \mathbf{F}^{mo} = \mathbf{F}^o \mathbf{G}^m, \tag{A.22}$$

With regards to the relations

$$\frac{\partial J}{\partial \mathbf{F}} = J^{-1} \mathbf{F}^{-T}, \tag{A.23}$$

$$\frac{\partial J}{\partial \mathbf{C}} = \frac{J}{2} \mathbf{C}^{-1}, \tag{A.24}$$

$$\frac{\partial C_{ij}^{-1}}{\partial C_{pq}} = -\frac{1}{2} \big(C_{ip}^{-1} C_{jq}^{-1} + C_{iq}^{-1} C_{jp}^{-1} \big), \tag{A.25}$$

it can be shown that

$$\frac{\partial w}{\partial C_{ij}} = M_R^e \frac{\partial \Psi^e}{\partial C_{ij}} + \sum_k M_R^k \frac{\partial \Psi^k}{\partial C_{ij}} + M_R^m \left(\frac{\partial \Psi^m}{\partial C_{ij}} + \frac{\partial \Psi^m_{act}}{\partial C_{ij}}\right) + \big(kJ(J-1)\big) C^{-1}_{ij}, \tag{A.26}$$

$$\begin{aligned}\frac{\partial^2 w}{\partial C_{ij}\partial C_{pq}} &= M_R^e \frac{\partial^2 \Psi^e}{\partial C_{ij}\partial C_{pq}} + \sum_k M_R^k \frac{\partial^2 \Psi^k}{\partial C_{ij}\partial C_{pq}} + M_R^m \left(\frac{\partial^2 \Psi^m}{\partial C_{ij}\partial C_{pq}} + \frac{\partial^2 \Psi^m_{act}}{\partial C_{ij}\partial C_{pq}}\right) \\ &\quad - \frac{1}{2}\big(kJ(J-1)\big)\big(C^{-1}_{ip}C^{-1}_{jq} + C^{-1}_{iq}C^{-1}_{jp}\big) + \frac{1}{2}kJ(2J-1)C^{-1}_{pq}C^{-1}_{ij}\end{aligned} \tag{A.27}$$

The Cauchy stress in the intermediate configuration can be written as

$$\mathbf{T}^o = \frac{2}{J^o}\mathbf{F}^o \frac{\partial w}{\partial \mathbf{C}}\big|_{\mathbf{C}=\mathbf{C}^o} \mathbf{F}^{oT}, \tag{A.28}$$

and, thus, from equation (A.26), we can write

$$\begin{aligned}T^o_{ij} &= \frac{2}{J^o} M_R^e F^o_{i\alpha} F^o_{j\beta} \frac{\partial \Psi^e}{\partial C_{\alpha\beta}}\big|_{\mathbf{C}=\mathbf{C}^o} + \frac{2}{J^o}\sum_k M_R^k F^o_{i\alpha} F^o_{j\beta} \frac{\partial \Psi^k}{\partial C_{\alpha\beta}}\big|_{\mathbf{C}=\mathbf{C}^o} \\ &\quad + \frac{2}{J^o} M_R^m F^o_{i\alpha} F^o_{j\beta} \left(\frac{\partial \Psi^m}{\partial C_{\alpha\beta}}\big|_{\mathbf{C}=\mathbf{C}^o} + \frac{\partial \Psi^m_{act}}{\partial C_{\alpha\beta}}\big|_{\mathbf{C}=\mathbf{C}^o}\right) + 2k(J^o-1)\delta_{ij} \\ &= \hat{T}^o_{ij} + 2k(J^o-1)\delta_{ij}.\end{aligned} \tag{A.29}$$

For the sake of simplicity, we merge the first three terms of Eq. A.29 into $\hat{T}^o_{ij}$, which denotes the internal stress in the artery as a result of deformation. Similarly, Eq. (A.27) can be written as

$$\frac{\partial^2 w}{\partial C_{ij}\partial C_{pq}}\big|_{\mathbf{C}=\mathbf{C}^o} = \hat{\mathcal{C}}_{ijpq} - \frac{1}{2}\big(kJ(J-1)\big)\big(C^{-1}_{ip}C^{-1}_{jq} + C^{-1}_{iq}C^{-1}_{jp}\big) + \frac{1}{2}kJ(2J-1)C^{-1}_{pq}C^{-1}_{ij}, \tag{A.30}$$

$$\hat{\mathcal{C}}_{ijpq} = M_R^e \frac{\partial^2 \Psi^e}{\partial C_{ij}\partial C_{pq}}\big|_{\mathbf{C}=\mathbf{C}^o} + \sum_k M_R^k \frac{\partial^2 \Psi^k}{\partial C_{ij}\partial C_{pq}}\big|_{\mathbf{C}=\mathbf{C}^o} + M_R^m \left(\frac{\partial^2 \Psi^m}{\partial C_{ij}\partial C_{pq}}\big|_{\mathbf{C}=\mathbf{C}^o} + \frac{\partial^2 \Psi^m_{act}}{\partial C_{ij}\partial C_{pq}}\big|_{\mathbf{C}=\mathbf{C}^o}\right) \tag{A.31}$$

Constitutive relations

The strain energy density function for the constituents of the arterial wall are given in Eqs. 2.11-2.13. Using these relations, equations (A.20), (A.22), and (A.29) and the chain rule, we can write the stress components at the intermediate configuration as

$$T^o_{rr} = \frac{c_1}{J^o} M^e_R (G^e_r)^2 \lambda^2_r + 2k(J^o - 1), \tag{A.32}$$

$$T^o_{\theta\theta} = \frac{c_1}{J^o} M^e_R (G^e_\theta)^2 \lambda^2_\theta + \frac{c_2}{J^o} \Big(\sum_k M^k_R (G^k_h)^2 ((\lambda^k)^2 - 1) \exp(c_3(\lambda^k - 1)^2) \sin^2(\alpha^k) \Big) \lambda^2_\theta$$
$$+ \frac{c_4}{J^o} \Big((G^m_h)^2 ((\lambda^m)^2 - 1) \exp(c_5(\lambda^k - 1)^2) \Big) \lambda^2_\theta + \frac{1}{J^o} \frac{S}{\rho} M^m_R \Big(1 + \frac{(\lambda_M - \lambda_\theta)^2}{(\lambda_M - \lambda_0)^2} \Big) \lambda_\theta + 2k(J^o - 1), \tag{A.33}$$

$$T^o_{zz} = \frac{c_1}{J^o} M^e_R (G^e_z)^2 \lambda^2_z + \frac{c_2}{J^o} \Big(\sum_k M^k_R (G^k_h)^2 ((\lambda^k)^2 - 1) \exp(c_3(\lambda^k - 1)^2) \cos^2(\alpha^k) \Big) \lambda^2_z + 2k(J^o - 1). \tag{A.34}$$

For the inflation and extension of an artery, we assume that the rotational part $\Omega^*_{kl} = 0$. Moreover, we assume the arterial wall to be an orthotropic material. Thus, the elasticity tensor in Eq. A.18 can be written in Voight notation and the reference system of principal direction

$$\mathbb{C} = \begin{bmatrix} C_{rrrr} & C_{rr\theta\theta} & C_{rrzz} & 0 & 0 & 0 \\ C_{\theta\theta rr} & C_{\theta\theta\theta\theta} & C_{\theta\theta zz} & 0 & 0 & 0 \\ C_{zzrr} & C_{zz\theta\theta} & C_{zzzz} & 0 & 0 & 0 \\ 0 & 0 & 0 & C_{\theta z\theta z} & 0 & 0 \\ 0 & 0 & 0 & 0 & C_{rzrz} & 0 \\ 0 & 0 & 0 & 0 & 0 & C_{r\theta r\theta} \end{bmatrix} = \begin{bmatrix} \mathbf{C}_1 & \mathbf{0} \\ \mathbf{0} & \mathbf{C}_2 \end{bmatrix}, \tag{A.35}$$

where the components of $\mathbf{C}_1$ can be expressed as

$$
\begin{aligned}
\mathcal{C}_{rrrr} &= T^o_{rr} + 2k, \\
\mathcal{C}_{rr\theta\theta} &= -T^o_{rr} + 2k(2J^o - 1), \\
\mathcal{C}_{rrzz} &= -T^o_{rr} + 2k(2J^o - 1), \\
\mathcal{C}_{\theta\theta rr} &= -T^o_{\theta\theta} + 2k(2J^o - 1), \\
\mathcal{C}_{\theta\theta\theta\theta} &= T^o_{\theta\theta} + 2k + \frac{2}{J^o} A_{\theta\theta} \lambda_\theta^4 \\
\mathcal{C}_{\theta\theta zz} &= -T^o_{\theta\theta} + 2k(2J^o - 1) + \frac{2}{J^o} A_{\theta z} \lambda_\theta^2 \lambda_z^2, \\
\mathcal{C}_{zzrr} &= -T^o_{zz} + 2k(2J^o - 1), \\
\mathcal{C}_{zz\theta\theta} &= -T^o_{zz} + 2k(2J^o - 1) + +2k(2J^o - 1) + \frac{2}{J^o} A_{\theta z} \lambda_\theta^2 \lambda_z^2 \\
\mathcal{C}_{zzzz} &= T^o_{zz} + 2k + \frac{2}{J^o} A_{zz} \lambda_z^4
\end{aligned}
\tag{A.36}
$$

$$
\begin{aligned}
A_{\theta\theta} &= c_2 \sum_k M_R^k (G_h^k)^4 (2c_3((\lambda^k)^2 - 1)^2 + 1) \exp(c_3((\lambda^k)^2 - 1)^2) \sin^4(\alpha^k) \\
&\quad + c_4 \big(M_R^m (G_h^m)^4 (2c_5((\lambda^m)^2 - 1)^2 + 1) \exp(c_5((\lambda^m)^2 - 1)^2) + \frac{S}{\rho} M_R^m \frac{(\lambda_M - \lambda_\theta)}{\lambda_\theta (\lambda_M - \lambda_0)^2} \\
A_{\theta z} &= c_2 \sum_k M_R^k (G_h^k)^4 (2c_3((\lambda^k)^2 - 1)^2 + 1) \exp(c_3((\lambda^k)^2 - 1)^2) \sin^2(\alpha^k) \cos^2(\alpha^k) \\
A_{zz} &= c_2 \sum_k M_R^k (G_h^k)^4 (2c_3((\lambda^k)^2 - 1)^2 + 1) \exp(c_3((\lambda^k)^2 - 1)^2) \cos^4(\alpha^k)
\end{aligned}
\tag{A.37}
$$

For simplicity, the terms related to collagen fibers and passive smooth muscle response in equation A.36 are denoted as $A_{\theta\theta}$, $A_{\theta z}$, and A_{zz}, and the term corresponding the active tone as A_{act}.

The elastic moduli E_i, Poisson ratios ν_{ij}, and shear moduli μ_{ij} can be obtained by finding

the following inverse matrix

$$\mathbb{S} = \begin{bmatrix} \frac{1}{E_r} & -\frac{\nu_{\theta r}}{E_\theta} & -\frac{\nu_{zr}}{E_z} & 0 & 0 & 0 \\ -\frac{\nu_{r\theta}}{E_r} & \frac{1}{E_\theta} & -\frac{\nu_{z\theta}}{E_z} & 0 & 0 & 0 \\ -\frac{\nu_{rz}}{E_r} & -\frac{\nu_{\theta z}}{E_\theta} & \frac{1}{E_z} & 0 & 0 & 0 \\ 0 & 0 & 0 & \frac{1}{2\mu_{\theta z}} & 0 & 0 \\ 0 & 0 & 0 & 0 & \frac{1}{2\mu_{rz}} & 0 \\ 0 & 0 & 0 & 0 & 0 & \frac{1}{2\mu_{r\theta}} \end{bmatrix} = \begin{bmatrix} \mathbf{C}_1^{-1} & \mathbf{0} \\ \mathbf{0} & \mathbf{C}_2^{-1} \end{bmatrix}, \tag{A.38}$$

Specifically, we can derive the following formulas for Young's moduli

$$E_r = \frac{\det(\mathbf{C}_1)}{\mathcal{C}_{\theta\theta\theta\theta}\mathcal{C}_{zzzz} - \mathcal{C}_{\theta\theta zz}\mathcal{C}_{zz\theta\theta}}, \tag{A.39}$$

$$E_\theta = \frac{\det(\mathbf{C}_1)}{\mathcal{C}_{rrrr}\mathcal{C}_{zzzz} - \mathcal{C}_{rrzz}\mathcal{C}_{zzrr}}, \tag{A.40}$$

$$E_z = \frac{\det(\mathbf{C}_1)}{\mathcal{C}_{\theta\theta\theta\theta}\mathcal{C}_{rrrr} - \mathcal{C}_{rr\theta\theta}\mathcal{C}_{\theta\theta rr}}. \tag{A.41}$$

Calculation of elastic modulus with the incompressibility constraint as a limit

Now, let us again consider the inflation and extension of a straight segment of artery. We assume that the artery can be modeled as a thin-walled cylinder, therefore, we approximate $T^o_{rr} \approx -P^o/2$ where P^o is the inside pressure in the intermediate configuration. Moreover, substituting $J^o = \det(\mathbf{F}^o)$ into equation (A.32) gives

$$T^o_{rr} = \frac{c_1}{\lambda_r\lambda_\theta\lambda_z} M^e_R (G^e_r)^2 \lambda_r^2 - 2k(\lambda_r\lambda_\theta\lambda_z - 1) = -\frac{P^o}{2}. \tag{A.42}$$

Solving this equation for λ_r gives

$$\lambda_r = \frac{\lambda_\theta \lambda_z (4k - P^o)}{2(C_1 + 2k\lambda_\theta^2 \lambda_z^2)} \tag{A.43}$$

where $C_1 = c_1 M_R^e (G_r^e)^2$ for the sake of brevity. Equation (A.43), thus, calculates the J^o

$$J^o = \frac{\lambda_\theta^2 \lambda_z^2 (4k - P^o)}{2(C_1 + 2k\lambda_\theta^2 \lambda_z^2)}. \tag{A.44}$$

Components of the elasticity tensor $\mathbb{C}$ show that the expressions for elastic moduli include volume change ratio as well as the pre-stresses and pre-stretches.

The arterial wall is considered an incompressible material. The strain energy function given in Eq. A.21, however, has a compressibility term $k(J-1)^2$ which vanishes when an incompressible material is taken as a limit. In other words, the term $k(J-1)$ can be treated as a penalty term for incompressible material. Clearly from Eq. (A.44), if we write $\lim_{k\to\infty} J^o = 1$, we will achieve the incompressibility. Nevertheless, under such conditions, the term $k(J-1)$ will remain an undetermined term. Specifying the boundary conditions will facilitate finding this parameter. Specifically in the current application, the pressure P^o, and pre-stretches λ_θ and λ_z can be considered as boundary conditions. Thus, we can write

$$\lim_{k\to\infty} k(J^o - 1) = \lim_{k\to\infty} k\left(\frac{\lambda_\theta^2 \lambda_z^2 (4k - P^o)}{2(C_1 + 2k\lambda_\theta^2 \lambda_z^2)} - 1\right), \tag{A.45}$$

which brings an indeterminate form of $\infty \times 0$. Using L'Hospital's rule gives

$$\lim_{k\to\infty} k(J^o - 1) = -\frac{1}{4}\left(\frac{2C_1}{\lambda_\theta^2 \lambda_z^2} + P^o\right), \tag{A.46}$$

which will bring the an undetermined term. Incorporating relation (A.46) into (A.39-A.41), will give the effective elastic moduli and Poisson's ratios in the three principal directions.

$$
\begin{aligned}
E_r = &\Big(2(-A_{\theta z}^2\lambda_\theta^4\lambda_z^4 + (3(2C_1 + \lambda_\theta^2\lambda_z^2P^o)^2)/(4\lambda_\theta^4\lambda_z^4) - 2A_{\theta z}\lambda_\theta^2\lambda_z^2T_{rr}^o + T_{rr}^oT_{\theta\theta}^o \\
&+ A_{zz}\lambda_z^4(T_{rr}^o + T_{\theta\theta}^o) + (T_{rr}^o + T_{\theta\theta}^o)T_{zz}^o + A_{\theta\theta}\lambda_\theta^4(A_{zz}\lambda_z^4 + T_{rr}^o + T_{zz}^o) \\
&+ ((2C_1 + \lambda_\theta^2\lambda_z^2P^o)(A_{\theta\theta}\lambda_\theta^4 - A_{\theta z}\lambda_\theta^2\lambda_z^2 + A_{zz}\lambda_z^4 + T_{rr}^o + T_{\theta\theta}^o + T_{zz}^o))/(\lambda_\theta^2\lambda_z^2))\Big)\Big/ \\
&\Big(A_{\theta\theta}\lambda_\theta^4 + (2C_1)/(\lambda_\theta^2\lambda_z^2) - 2A_{\theta z}\lambda_\theta^2\lambda_z^2 + A_{zz}\lambda_z^4 + P^o + T_{\theta\theta}^o + T_{zz}^o\Big)
\end{aligned} \tag{A.47}
$$

$$
\begin{aligned}
E_\theta = &\Big(2(-A_{\theta z}^2\lambda_\theta^4\lambda_z^4 + (3(2C_1 + \lambda_\theta^2\lambda_z^2P^o)^2)/(4\lambda_\theta^4\lambda_z^4) - 2A_{\theta z}\lambda_\theta^2\lambda_z^2T_{rr}^o + T_{rr}^oT_{\theta\theta}^o \\
&+ A_{zz}\lambda_z^4(T_{rr}^o + T_{\theta\theta}^o) + (T_{rr}^o + T_{\theta\theta}^o)T_{zz}^o + A_{\theta\theta}\lambda_\theta^4(A_{zz}\lambda_z^4 + T_{rr}^o + T_{zz}^o) \\
&+ ((2C_1 + \lambda_\theta^2\lambda_z^2P^o)(A_{\theta\theta}\lambda_\theta^4 - A_{\theta z}\lambda_\theta^2\lambda_z^2 + A_{zz}\lambda_z^4 + T_{rr}^o + T_{\theta\theta}^o + T_{zz}^o))/(\lambda_\theta^2\lambda_z^2))\Big)\Big/ \\
&\Big((2C_1)/(\lambda_\theta^2\lambda_z^2) + A_{zz}\lambda_z^4 + P^o + T_{rr}^o + T_{zz}^o\Big)
\end{aligned} \tag{A.48}
$$

$$
\begin{aligned}
E_z = &\Big(2(-A_{\theta z}^2\lambda_\theta^4\lambda_z^4 + (3(2C_1 + \lambda_\theta^2\lambda_z^2P^o)^2)/(4\lambda_\theta^4\lambda_z^4) - 2A_{\theta z}\lambda_\theta^2\lambda_z^2T_{rr}^o + T_{rr}^oT_{\theta\theta}^o \\
&+ A_{zz}\lambda_z^4(T_{rr}^o + T_{\theta\theta}^o) + (T_{rr}^o + T_{\theta\theta}^o)T_{zz}^o + A_{\theta\theta}\lambda_\theta^4(A_{zz}\lambda_z^4 + T_{rr}^o + T_{zz}^o) \\
&+ ((2C_1 + \lambda_\theta^2\lambda_z^2P^o)(A_{\theta\theta}\lambda_\theta^4 - A_{\theta z}\lambda_\theta^2\lambda_z^2 + A_{zz}\lambda_z^4 + T_{rr}^o + T_{\theta\theta}^o + T_{zz}^o))/(\lambda_\theta^2\lambda_z^2))\Big)\Big/ \\
&\Big((2C_1)/(\lambda_\theta^2\lambda_z^2) + A_{\theta\theta}\lambda_\theta^4 + P^o + T_{rr}^o + T_{\theta\theta}^o\Big)
\end{aligned} \tag{A.49}
$$

$$
\nu_{12} = \frac{2C_1 + \lambda_\theta^2\lambda_z^2(-2A_{\theta z}\lambda_\theta^2\lambda_z^2 + 2A_{zz}\lambda_z^4 + P^o + 2T_{zz}^o)}{(4C_1 + 2\lambda_\theta^2 l3^2(A_{\theta\theta}\lambda_\theta^4 - 2A_{\theta z}\lambda_\theta^2\lambda_z^2 + A_{zz}\lambda_z^4 + P^o + T_{\theta\theta}^o + T_{zz}^o)} \tag{A.50}
$$

$$
\nu_{21} = \frac{2C_1 + \lambda_\theta^2\lambda_z^2(-2A_{\theta z}\lambda_\theta^2\lambda_z^2 + 2A_{zz}\lambda_z^4 + P^o + 2T_{zz}^o)}{4C_1 + 2\lambda_\theta^2\lambda_z^2(A_{zz}\lambda_z^4 + P^o + T_{rr}^o + T_{zz}^o)} \tag{A.51}
$$

$$
\nu_{13} = \frac{2C_1 + \lambda_\theta^2\lambda_z^2(2A_{\theta\theta}\lambda_\theta^4 - 2A_{\theta z}\lambda_\theta^2\lambda_z^2 + P^o + 2T_{\theta\theta}^o)}{4C_1 + 2\lambda_\theta^2\lambda_z^2(A_{\theta\theta}\lambda_\theta^4 - 2A_{\theta z}\lambda_\theta^2\lambda_z^2 + A_{zz}\lambda_z^4 + P^o + T_{\theta\theta}^o + T_{zz}^o)} \tag{A.52}
$$

$$
\nu_{31} = \frac{2C_1 + \lambda_\theta^2\lambda_z^2(2A_{\theta\theta}\lambda_\theta^4 - 2A_{\theta z}\lambda_\theta^2\lambda_z^2 + P^o + 2T_{\theta\theta}^o)}{4C_1 + 2\lambda_\theta^2\lambda_z^2(A_{\theta\theta}\lambda_\theta^4 + P^o + T_{rr}^o + T_{\theta\theta}^o)} \tag{A.53}
$$

$$
\nu_{23} = \frac{2C_1 + \lambda_\theta^2\lambda_z^2(2A_{\theta z}\lambda_\theta^2\lambda_z^2 + P^o + 3T_{rr}^o - T_{\theta\theta}^o)}{4C_1 + 2\lambda_\theta^2\lambda_z^2(A_{zz}\lambda_z^4 + P^o + T_{rr}^o + T_{zz}^o)} \tag{A.54}
$$

$$
\nu_{32} = \frac{2C_1 + \lambda_\theta^2\lambda_z^2(2A_{\theta z}\lambda_\theta^2\lambda_z^2 + P^o + 3T_{rr}^o - T_{\theta\theta}^o)}{4C_1 + 2\lambda_\theta^2\lambda_z^2(A_{\theta\theta}\lambda_\theta^4 + P^o + T_{rr}^o + T_{\theta\theta}^o)} \tag{A.55}
$$

Calculation of elastic modulus with the incompressibility constraint using a Lagrange multiplier

The method described above, expresses the problem using an incompressible material using the $k(J-1)$ term in the constitutive relation. However, this condition could be relaxed by allowing the material to be compressible but prescribing an isochoric motion. In the realm of continuum mechanics, this motion is characterized by $\det(F) = 1$. However, this kinematical constraint is expressed by adding the term $-p\mathbf{I}$ to the stress tensor, where the hydrostatic pressure p is a Lagrange multiplier. Therefore, the Cauchy stress in Eq. A.8 can be written as

$$\mathbf{T} = -p\mathbf{I} + \mathbf{F}\mathbf{S}\mathbf{F}^T, \quad \mathbf{S} = 2\frac{\partial w}{\partial \mathbf{C}}, \tag{A.56}$$

It is convenient to use $\hat{\mathbf{T}} = \mathbf{F}\mathbf{S}\mathbf{F}^T$ representing the stress as a result of deformation in the material. Following Eqs. (A.9 to A.14), the stress can be written as

$$\mathbf{T} = -p\mathbf{I} + (\mathbf{I}+\mathbf{H})\mathbf{F}^o\big(\mathbf{S}^o + \frac{\partial \mathbf{S}}{\partial \mathbf{C}}\Big|_{\mathbf{C}^o}\mathbf{C}^*\big)\mathbf{F}^{oT}(\mathbf{I}+\mathbf{H})^T, \tag{A.57}$$

where $p = p^o + p^*$ are the Lagrange multipliers for the large (p^o) and small (p^*) deformations, respectively. Finally, the incremental stress can be written as

$$\Delta T_{ij} = -p^*\delta_{ij} + H_{ik}\hat{T}^o_{kj} + \hat{T}^o_{ik}H_{jk} + 4F^o_{i\alpha}F^o_{j\beta}F^o_{lp}F^o_{mq}\frac{\partial^2 w}{\partial C_{\alpha\beta}\partial C_{pq}}\Big|_{\mathbf{C}=\mathbf{C}^o}\epsilon^*_{lm}, \tag{A.58}$$

$$= -p^*\delta_{ij} + \bar{\mathcal{C}}_{ijkl}\epsilon^*_{kl} + \bar{\mathcal{D}}_{ijkl}\Omega^*_{kl} \tag{A.59}$$

where

$$\bar{\mathcal{C}}_{ijkl} = \delta_{ik}\hat{T}^o_{lj} + \delta_{jk}\hat{T}^o_{il} + \frac{4}{J^o}F^o_{i\alpha}F^o_{j\beta}F^o_{lp}F^o_{mq}\frac{\partial^2 w}{\partial C_{\alpha\beta}\partial C_{pq}}\Big|_{\mathbf{C}=\mathbf{C}^o}, \tag{A.60}$$

$$\bar{\mathcal{D}}_{ijkl} = \delta_{ik}\hat{T}^o_{lj} + \delta_{jk}\hat{T}^o_{il}. \tag{A.61}$$

Now, we consider the example of inflation and extension of the artery. Following the previous section, we consider the rotation to be negligible $\mathbf{\Omega}^* = 0$. In addition, let us agains assume that the strain energy function is given by Eq. (2.14). By the assumption of orthotropic material, the stress components and the stiffness tensor is given as

$$\hat{T}^o_{rr} = c_1 M^e_R (G^e_r)^2 \lambda_r^2, \tag{A.62}$$

$$\begin{aligned}\hat{T}^o_{\theta\theta} = {} & c_1 M^e_R (G^e_\theta)^2 \lambda_\theta^2 + c_2\Big(\sum_k M^k_R (G^k_h)^2((\lambda^k)^2-1)\exp(c_3(\lambda^k-1)^2)\sin^2(\alpha^k)\Big)\lambda_\theta^2 \\ & + c_4\Big((G^m_h)^2((\lambda^m)^2-1)\exp(c_5(\lambda^k-1)^2)\Big)\lambda_\theta^2 + \frac{S}{\rho}M^m_R\Big(1+\frac{(\lambda_M-\lambda_\theta)^2}{(\lambda_M-\lambda_0)^2}\Big)\lambda_\theta,\end{aligned} \tag{A.63}$$

$$\hat{T}^o_{zz} = c_1 M^e_R (G^e_z)^2 \lambda_z^2 + c_2 J^o\Big(\sum_k M^k_R (G^k_h)^2((\lambda^k)^2-1)\exp(c_3(\lambda^k-1)^2)\cos^2(\alpha^k)\Big)\lambda_z^2. \tag{A.64}$$

$$\begin{aligned}
\bar{\mathcal{C}}_{rrrr} &= 2\hat{T}^o_{rr}, \\
\bar{\mathcal{C}}_{rr\theta\theta} &= 0, \\
\bar{\mathcal{C}}_{rrzz} &= 0, \\
\bar{\mathcal{C}}_{\theta\theta rr} &= 0, \\
\bar{\mathcal{C}}_{\theta\theta\theta\theta} &= 2\hat{T}^o_{\theta\theta} + 2A_{\theta\theta}\lambda_\theta^4 \\
\bar{\mathcal{C}}_{\theta\theta zz} &= 2A_{\theta z}\lambda_\theta^2\lambda_z^2, \\
\bar{\mathcal{C}}_{zzrr} &= 0, \\
\bar{\mathcal{C}}_{zz\theta\theta} &= 2A_{\theta z}\lambda_\theta^2\lambda_z^2, \\
\bar{\mathcal{C}}_{zzzz} &= 2\hat{T}^o_{zz} + 2A_{zz}\lambda_z^4.
\end{aligned} \tag{A.65}$$

Directional Young's modulus can be computed by considering a simple uniaxial stretch in the desired direction. For instance, we consider the pre-stressed artery incurs a circumferential incremental stress. Therefore, the linearized response can be written in the following reduced form

$$\begin{bmatrix} 0 \\ \Delta T \\ 0 \end{bmatrix} = \begin{bmatrix} -p^* \\ -p^* \\ -p^* \end{bmatrix} + \begin{bmatrix} \bar{\mathcal{C}}_{rrrr} & 0 & 0 \\ 0 & \bar{\mathcal{C}}_{\theta\theta\theta\theta} & \bar{\mathcal{C}}_{\theta\theta zz} \\ 0 & \bar{\mathcal{C}}_{zz\theta\theta} & \bar{\mathcal{C}}_{zzzz} \end{bmatrix} \begin{bmatrix} \epsilon_{rr} \\ \epsilon_{\theta\theta} \\ \epsilon_{zz} \end{bmatrix}. \tag{A.66}$$

Reordering the equations for the strains, we can write

$$\begin{aligned} \epsilon_{rr} &= \frac{p^*}{\bar{\mathcal{C}}_{rrrr}}, \\ \epsilon_{zz} &= \frac{p^* - \bar{\mathcal{C}}_{\theta\theta zz}}{\bar{\mathcal{C}}_{zzzz}}, \\ \epsilon_{\theta\theta} &= \big(\bar{\mathcal{C}}_{\theta\theta\theta\theta} - \frac{\bar{\mathcal{C}}^2_{\theta\theta zz}}{\bar{\mathcal{C}}_{zzzz}}\big)^{-1}\big(\Delta T + p^* - \frac{\bar{\mathcal{C}}_{\theta\theta zz}}{\bar{\mathcal{C}}_{zzzz}} p^*\big) \end{aligned} \tag{A.67}$$

Because of incompressibility of the material, we can write $\epsilon_{rr} + \epsilon_{\theta\theta} + \epsilon_{zz} = 0$. Thus, using this condition and the symmetries, the Lagrange multiplier can be computed as

$$p^* = \frac{\bar{\mathcal{C}}_{rrrr}(\bar{\mathcal{C}}_{\theta\theta zz} - \bar{\mathcal{C}}_{zzzz})}{-\bar{\mathcal{C}}^2_{\theta\theta zz} + \bar{\mathcal{C}}_{\theta\theta\theta\theta}\bar{\mathcal{C}}_{zzzz} + \bar{\mathcal{C}}_{rrrr}(\bar{\mathcal{C}}_{\theta\theta\theta\theta} - 2\bar{\mathcal{C}}_{\theta\theta zz} + \bar{\mathcal{C}}_{zzzz})}\Delta T. \tag{A.68}$$

Substituting p^* into equation A.67, gives the following linear relationship between stress and strain

$$\epsilon_{\theta\theta} = \frac{(\bar{\mathcal{C}}_{rrrr} + \bar{\mathcal{C}}_{zzzz})}{-\bar{\mathcal{C}}^2_{\theta\theta zz} + \bar{\mathcal{C}}_{\theta\theta\theta\theta}\bar{\mathcal{C}}_{zzzz} + \bar{\mathcal{C}}_{rrrr}(\bar{\mathcal{C}}_{\theta\theta\theta\theta} - 2\bar{\mathcal{C}}_{\theta\theta zz} + \bar{\mathcal{C}}_{zzzz})}\Delta T. \tag{A.69}$$

Therefore, the effective Young's modulus can be written as

$$\bar{E}_\theta = \frac{-\bar{\mathcal{C}}^2_{\theta\theta zz} + \bar{\mathcal{C}}_{\theta\theta\theta\theta}\bar{\mathcal{C}}_{zzzz} + \bar{\mathcal{C}}_{rrrr}(\bar{\mathcal{C}}_{\theta\theta\theta\theta} - 2\bar{\mathcal{C}}_{\theta\theta zz} + \bar{\mathcal{C}}_{zzzz})}{\bar{\mathcal{C}}_{rrrr} + \bar{\mathcal{C}}_{zzzz}} \tag{A.70}$$

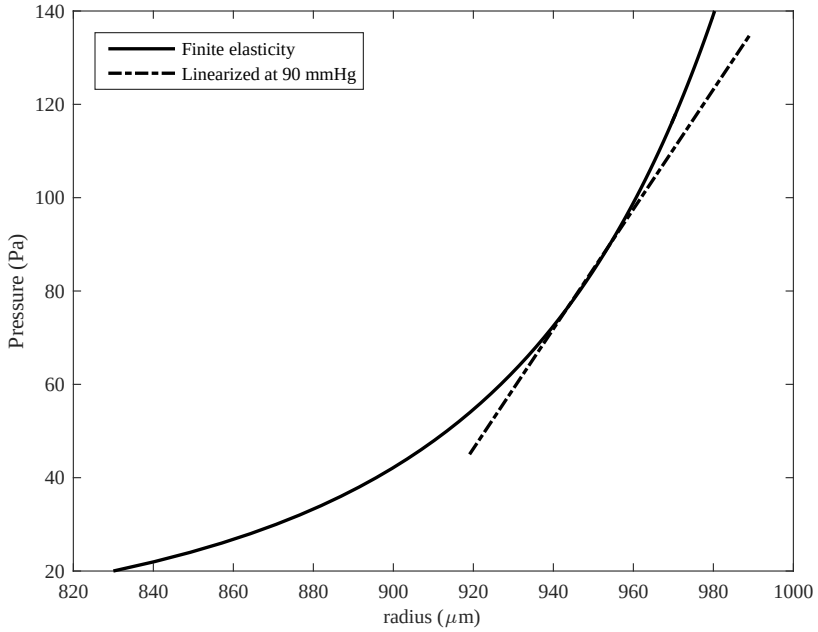

Figure A.1: Pressure versus radius during inflation at a fixed length. The linearized elastic parameters were calculated at 90 mmHg.

Finally, inserting the corresponding terms from Eq. A.65

$$\bar{E}_\theta = \Big(2(-A_{\theta z}^2\lambda_\theta^4\lambda_z^4 - 2A_{\theta z}\lambda_\theta^2\lambda_z^2\hat{T}_{rr}^o + A_{zz}\lambda_z^4\hat{T}_{rr}^o + A_{zz}\lambda_z^4\hat{T}_{\theta\theta}^o + \hat{T}_{rr}^o\hat{T}_{\theta\theta}^o \tag{A.71}$$

$$+ \hat{T}_{rr}^o\hat{T}_{zz}^o + \hat{T}_{\theta\theta}^o\hat{T}_{zz}^o + A_{\theta\theta}\lambda_\theta^4(A_{zz}\lambda_z^4 + \hat{T}_{rr}^o + \hat{T}_{zz}^o))\Big)\Big/\Big(A_{zz}\lambda_z^4 + \hat{T}_{rr}^o + \hat{T}_{zz}^o\Big) \tag{A.72}$$

Similarly, other directional Young's moduli and Poisson's ratios can be computed.

Computation of arterial modulus in vivo

For the purpose of illustration and validation of the presented linearization, the inflation at a fixed length of an arterial segment from rabbit's basilar artery is presented. The parameters are directly obtained from [160]. First, the finite elasticity solution to the inflation

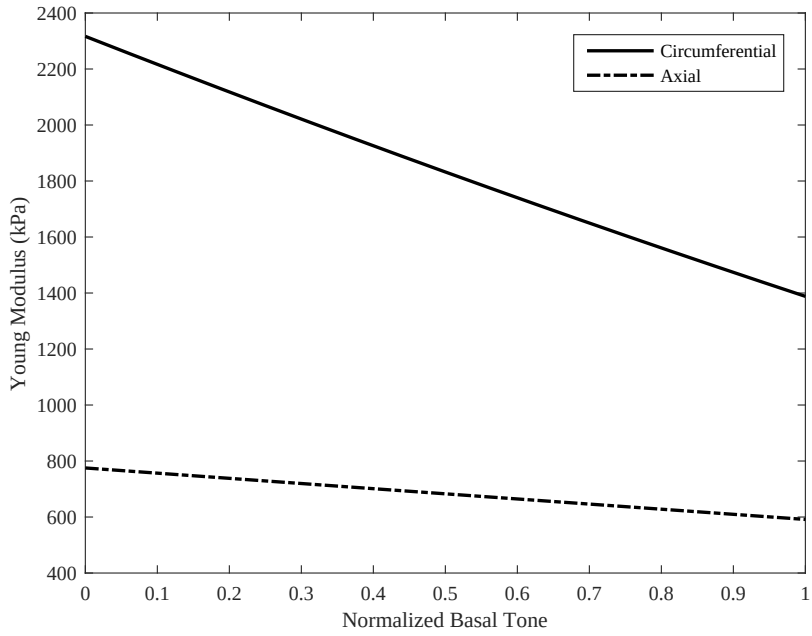

Figure A.2: Linearized parameters for different degrees of smooth muscle tone.

problem is found using the equilibrium for large deformations. Then, using the linearization, pressure-radius relationship over approximately one cardiac cycle is computed based on an intermediate state (at $p^o = 90$mmHg). Figure A.1 shows the discrepancy between the linearization and the hyperelastic response of the artery.

Despite early advances in solving coupled fluid-solid problems [208], large scale computational problems remain challenging because of nonlinear material properties, the complex wall geometry, and the pulsatility of the blood flow in large arteries. The proposed formulation for the theory of small on large shows that by choosing an appropriate intermediate configuration, the linearization gives the error in radius within $\pm 1.32\%$. The stiffness of the wall however can change due to alterations in pressure, smooth muscle tone, or microstructure (from growth and remodeling) [160]. To illustrate this point, the value basal tone (S) in Eq. 2.18 is changed from 0 to 80 kPa. The circumferential and axial Young's moduli are plotted against normalized value of the basal tone in Fig. A.2.

The calculations show that as the vasoconstriction increases, Young's modulus decreases. A similar prediction was made in [209] were this increase was attributed to transfer of the load to more rigid elements (like collagen) in the arterial wall. Nevertheless, as mentioned the estimation of *in-vivo* stiffness of the artery highly depends on the contents of the elastic wall (mass fractions) as well as their deposition stretches and the artery's homeostatic condition.

APPENDIX B: Optimization and Steady state hemodynamics of the arterial tree

In the present model, the whole arterial tree is assumed to have a binary tree structure. Each vessel in the tree is modeled as a straight segment with steady laminar blood flow. Thus, using Poiseuille flow in each segment, the pressure drop along the blood vessel can be calculated as

$$\Delta p^s = \frac{8\mu l}{\pi R^4} q^s = Z_0(R) q^s, \tag{B.73}$$

where μ is the viscosity of blood, l is the length of the artery, and $Z_0(R)$ is the hydraulic resistance. Note that the assumption of Poiseuille flow was used once in formulating C_{drag}. The bifurcation is assumed to occur at one point. The conservation of mass at the bifurcation requires

$$q_p^s = q_{d_1}^s + q_{d_2}^s, \tag{B.74}$$

and assuming that pressure is continuous over the bifurcation

$$p_p^s = p_{d_1}^s = p_{d_2}^s, \tag{B.75}$$

where subscripts p, d_1, and d_2 show the quantity at a parent and its daughter vessels, respectively.

Before constructing the system of equations to solve the hemodynamics of the problem, we need to index every bifurcation point in the arterial tree.

Figure B.3 shows a bifurcation point in the arterial tree structure. Index k defines the

generation number of the parent vessel ranging from 1 to previous to last generation number $N-1$. Alternatively, value of s shows the index of the bifurcation point across one generation, therefore, ranging between 1 to the number of bifurcations in the kth generation. The arrows on figure show the direction of the numbering. In addition, the segments are counted successively, in accord with the fashion used for k and s. Therefore, the block of matrix related to the bifurcation point $[k, s]$ can be constructed as

$$
\begin{array}{c}
\\
3(2^{k-1}+s-2)+1 \\
3(2^{k-1}+s-2)+2 \\
3(2^{k-1}+s-2)+3
\end{array}
\begin{array}{c}
\begin{array}{cccccc}
2^k+2s-3 & 2^k+2s-2 & 2^{k+1}+4s-5 & 2^{k+1}+4s-4 & 2^{k+1}+4s-3 & 2^{k+1}+4s-2
\end{array} \\
\begin{bmatrix}
1 & 0 & -1 & 0 & -1 & 0 \\
0 & 1 & -Z_0(R_{j+1}) & -1 & 0 & 0 \\
0 & 1 & 0 & 0 & -Z_0(R_j) & -1
\end{bmatrix}
\end{array}
\times
\begin{bmatrix}
q^s_{(k,s)} \\
p^s_{(k,s)} \\
q^s_{(k+1,2s-1)} \\
p^s_{(k+1,2s-1)} \\
q^s_{(k+1,2s)} \\
p^s_{(k+1,2s)}
\end{bmatrix}
= \begin{bmatrix} 0 \\ 0 \\ 0 \end{bmatrix}
\tag{B.76}
$$

where $q^s_{(k,s)}$ is essentially the flow rate in the parent vessel at the bifurcation. The system of equations (B.76) calculates flow rate and pressure at every location in the arterial tree with prescription of appropriate boundary conditions (pressure and flow rate at the inlet and outlets).

The cost function minimization, $\min C(R; \bar{p}^s, q^s)$ in Eq. 2.30, at each individual vessel $[k, s]$ is solved together with the steady state hemodynamics acting on the entire tree (B.76). Such minimization is implemented in the nested loop. At the external loop, for a current tree geometry (i.e., given R and L) the tree hemodynamics p^s and q^s is resolved. Then for current hemodynamics state (i.e., given p^s and q^s) in the internal loop, Newton-Raphson

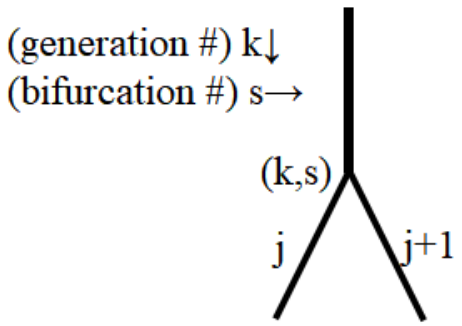

Figure B.3: Schematic of the bifurcation point $[k, s]$ in the arterial tree.

method solved the optimization problem to update R at each vessel sequentially.

APPENDIX C: Axisymmetric solution to pulsatile hemodynamics in one vessel

Here we demonstrate the solution to the fast time (cardiac cycle) hemodynamics (velocity $\mathbf{v}$ and pressure p) for axisymmetric in cylindrical coordinates (r, z, θ). Consider a cylindrical, straight, long vessel with a wall described as elastic membrane with no torsion and rotation: $h << R << L$ with wall thickness h, lumen radius R, and vessel length L. The velocity field can be decomposed to

$$\begin{aligned} \mathbf{v}^s &= [0, v_z^s(z), 0], \\ \mathbf{v}^f &= [v_r^f(r,z), v_z^f(r,z), 0], \end{aligned} \tag{C.77}$$

where superscripts s and f denote the slow and fast time-scales, respectively. The boundary conditions and constraints are

1. no-slip boundary condition near the wall: at $r = R$

$$\begin{aligned} v_z^s &= 0, \\ v_r^f &= \partial u_r^f / \partial t, \\ v_z^f &= \partial u_z^f / \partial t. \end{aligned} \tag{C.78}$$

2. finite velocity at $r = 0$.

The steady-state solution of the slow-time system can be described by Poiseuille velocity and flow rate under linear pressure

$$\begin{aligned} v_z^s &= \frac{1}{4\mu}\left(r^2 - R^2\right)\frac{\partial p^s}{\partial z}, \\ q^s &= -\frac{\pi R^4}{8\mu}\frac{\partial p^s}{\partial z} = \frac{\pi R^4 \Delta p^s}{8\mu L}, \quad \Delta p^s = p^s(0) - p^s(L). \end{aligned} \tag{C.79}$$

Next, we first consider the long wave approximation for pulsatile flow: $c/\omega >> R$ and $c >> v_z^f >> v_r^f$, where c is the pulse wave propagation speed and ω is angular frequency. Second, we consider the artery to be longitudinally constrained with the pressure and wall shear stress acting as fast-time body forces, as proposed by [210]. Finally, we use an orthotropic relation for the membrane stiffness. Therefore, using the analytical solution presented in [208, 210], we can drive the hemodynamics solution of perturbation fields at each given frequency ω

$$\begin{aligned} p^f &= Pe^{i\omega(t-z/c)}, \quad q^f = Qe^{i\omega(t-z/c)} \quad Q = \frac{\pi R^2 P}{c\rho_{fluid}}\left(1-g\right), \\ v_r^f &= \frac{iP\omega R}{2c^2\rho_{fluid}}\left(\frac{r}{R} - \frac{J_1\left(\Lambda r/R\right)}{\Lambda J_0\left(\Lambda\right)}\right)e^{i\omega(t-z/c)}, \\ v_z^f &= \frac{P}{c\rho_{fluid}}\left(1 - \frac{J_0\left(\Lambda r/R\right)}{\Lambda J_0\left(\Lambda\right)}\right)e^{i\omega(t-z/c)}, \\ u_r^f &= \frac{PR}{2c^2\rho_{fluid}}\left(1-g\right)e^{i\omega(t-z/c)}, \quad u_z^f = 0, \end{aligned} \tag{C.80}$$

with the Bessel functions of the first kind J_0, J_1, $g = 2J_1(\Lambda)/(\Lambda J_0(\Lambda))$, $\Lambda = i^{3/2}\alpha$, and the Womersley number

$$\alpha = R\sqrt{\omega\rho_{fluid}/\mu}. \tag{C.81}$$

The wave propagation speed c (i.e., pulse wave velocity) is a clinically important cardiovascular metric, used to infer the vascular wall stiffness [165]. The pulse wave velocity for the longitudinally tethered vessel wall motion can be expressed as

$$c = \sqrt{\frac{(1-g)h\,\mathcal{A}_{\theta\theta}|_{p^s}}{2R\rho_{fluid}}}. \tag{C.82}$$

Since the vessel wall is longitudinally constrained, the main stiffness contribution to the wave propagation equations comes from the circumferential component of the stiffness matrix, $A_{\theta\theta}$ which is linearized at current steady pressure p^s (see Chapter 2 for more detail). The total pressure and flow rate at time domain are obtained by applying Fourier series for solution

(C.80) with P_n and Q_n at multiple frequencies $\omega_n = 2\pi n/T$, and using slow-time solution (C.79) at zero-frequency

$$p = p^s + \mathrm{Re}\left(\sum_{n=1}^{\infty} P_n e^{i\omega_n(t-z/c_n)}\right), \quad q = q^s + \mathrm{Re}\left(\sum_{n=1}^{\infty} Q_n e^{i\omega_n(t-z/c_n)}\right), \tag{C.83}$$

where real values of oscillatory pressure and flow rate are taken. Furthermore, we compute the characteristic impedance $Z^c(\omega)$ [165] in frequency domain, using Womersley's solution (C.80), and hydraulic resistance using Poiseuille flow (C.79)

$$Z^c(\omega) = \frac{P}{Q} = \frac{c\rho_{fluid}}{\pi R^2\,(1-g)} = \frac{1}{\pi R^2}\sqrt{\frac{h\rho_{fluid}\,\mathcal{A}_{\theta\theta}|_{p^s}}{2R(1-g)}}. \tag{C.84}$$

Similarly we also compute the input impedance $Z^{inp}(\omega) = P/Q|_{z=0}$ and terminal impedance $Z^T(\omega) = P/Q|_{z=L}$. The pressure-flow relation in time domain (here at vessel end) can be expressed via convolution integral of terminal impedance and flow as

$$p(L,t) = \frac{1}{T}\int_{t-T}^{t} q(L,t_1)z^T(L,t-t_1)dt_1, \tag{C.85}$$

which can be used as outflow impedance boundary condition for patient-specific geometries [211].

APPENDIX D: Recursive algorithms: fast-time hemodynamics

Here we present the recursive algorithm that for a given tree geometry and discrete frequency computes the impedance at each bifurcation from the bottom to the top for using equations (3.3-3.6).

Algorithm 1

Fast-time: Step I (backward):

Given: $\rho_{fluid}, \mu, h, T,$

$R[k,s], L[k,s], \mathcal{A}_{\theta\theta}[k,s] = \mathcal{A}_{\theta\theta}|_{p^s[k,s]}, \quad s = 1, ..2^{k-1},$

$Z_n^{inp}[N,s], \quad s = 1, \cdots 2^{N-1}$

Find $Z_n^{inp}[k,s]$ for $k < N$ and $s = 1, \cdots 2^{k-1}$

for $k = (N-1) : -1 : 1$

for $s = 1 : 2^{k-1}$

$\{g_n, c_n\}[k,s]$= WomersleyOneVessel($\rho_{fluid}, \mu, h, T, R[k,s]$,$\mathcal{A}_{\theta\theta}[k,s]$)

$$Z_n^T[k,s] = \frac{Z_n^{inp}[k+1,2s] \cdot Z_n^{inp}[k+1,2s-1]}{Z_n^{inp}[k+1,2s] + Z_n^{inp}[k+1,2s-1]} \qquad \text{terminal impedance)}$$

$$Z_n^c[k,s] = \frac{\rho_{fluid} c_n[k,s]}{\pi R^2[k,s]\,(1 - g_n[k,s])} \qquad \text{(characteristic impedance)}$$

$$\Gamma_n[k,s] = \frac{Z_n^T[k,s] - Z_n^c[k,s]}{Z_n^T[k,s] + Z_n^c[k,s]} \qquad \text{(reflection coefficient)}$$

$$Z_n^{inp}[k,s] = Z_n^c[k,s] \frac{1 + \Gamma_n[k,s] e^{-i\omega_n 2L[k,s]/c_n[k,s]}}{1 - \Gamma_n[k,s] e^{-i\omega_n 2L[k,s]/c_n[k,s]}} \qquad \text{(input impedance)}$$

end

end

The pulsatile hemodynamics can be reconstructed from the top to the bottom. The components of the fast-time terminal pressure P_T^n and input flow Q_{inp}^n in frequency domain are found using Eq. 3.4. Without loss of generality, here the input pressure is given

---

Algorithm 2:

Fast - time: Step II (forward)

Given $P^n_{inp}[1,1]$

at vessel $[k,s]:$ $R, L, c_n, \Gamma_n, Z^c_n, Z^{inp}_n$

Find $P^n_T[k,s], Q^n_{inp}[k,s]$

for$k = 1 : N$

for $s = 1 : 2^{k-1}$

$\bar{s} = \text{round}(s/2)$

$P^n_{inp}[k,s] = P^n_T[k-1,\bar{s}]$ for $k > 1$

$Q^n_{inp}[k,s] = P^n_{inp}[k,s] \big/ Z^{inp}_n[k,s]$

$H^n_{forw} = P^n_{inp}[k,s] \big/ \left(1 + \Gamma_n[k,s] e^{-i2\omega_n L[k,s]/c_n[k,s]}\right)$

$P^n_T[k,s] = H^n_{forw} e^{-i\omega_n L/c_n[k,s]} \left(1 + \Gamma_n[k,s]\right)$

end

end

BIBLIOGRAPHY

BIBLIOGRAPHY

[1] GBD Mortality and Causes of Death Collaborators , "Global, regional, and national life expectancy, all-cause mortality, and cause-specific mortality for 249 causes of death, 1980-2015: a systematic analysis for the Global Burden of Disease Study 2015.," *Lancet (London, England)*, vol. 388, pp. 1459–1544, oct 2016.

[2] World Heart Federation-Champion Advocates Programme, "The cost of CVD," 2019. [Online]. Available: `http://www.championadvocates.org/en/champion-advocates-programme/the-costs-of-cvd`.

[3] J. D. Humphrey and K. R. Rajagopal, "A constrained mixture model for growth and remodeling of soft tissues," *Mathematical Models and Methods in Applied Sciences*, vol. 12, pp. 407–430, mar 2002.

[4] S. Baek, A. Valentín, and J. D. Humphrey, "Biochemomechanics of Cerebral Vasospasm and its Resolution: II. Constitutive Relations and Model Simulations," *Ann Biomed Eng*, vol. 35, p. 1498, Sept. 2007.

[5] C. A. Figueroa, S. Baek, C. A. Taylor, and J. D. Humphrey, "A computational framework for fluid–solid-growth modeling in cardiovascular simulations," *Computer Methods in Applied Mechanics and Engineering*, vol. 198, pp. 3583–3602, Sept. 2009.

[6] H. Getachew Tilahun, *Cardiovascular System Modeling: Arterial Growth and Remodeling*. Ph.D., Michigan State University, United States – Michigan, 2017.

[7] C. D. Murray, "The Physiological Principle of Minimum Work," *Proc Natl Acad Sci U S A*, vol. 12, pp. 207–214, Mar. 1926.

[8] A. J. H. M. Houben, R. J. H. Martens, and C. D. A. Stehouwer, "Assessing Microvascular Function in Humans from a Chronic Disease Perspective.," *Journal of the American Society of Nephrology : JASN*, vol. 28, pp. 3461–3472, dec 2017.

[9] V. V. McLaughlin, S. L. Archer, D. B. Badesch, R. J. Barst, H. W. Farber, J. R. Lindner, M. A. Mathier, M. D. McGoon, M. H. Park, R. S. Rosenson, L. J. Rubin, V. F. Tapson, and J. Varga, "ACCF/AHA 2009 Expert Consensus Document on Pulmonary Hypertension: A Report of the American College of Cardiology Foundation Task Force on Expert Consensus Documents and the American Heart Association: Developed in Collaboration With the American College of Chest Physicians, American Thoracic Society, Inc., and the Pulmonary Hypertension Association," *Circulation*, vol. 119, pp. 2250–2294, Apr. 2009.

[10] M. Humbert, O. Sitbon, A. Chaouat, M. Bertocchi, G. Habib, V. Gressin, A. Yaici, E. Weitzenblum, J.-F. Cordier, F. Chabot, C. Dromer, C. Pison, M. Reynaud-Gaubert,

A. Haloun, M. Laurent, E. Hachulla, and G. Simonneau, "Pulmonary arterial hypertension in France: results from a national registry," *Am. J. Respir. Crit. Care Med.*, vol. 173, pp. 1023–1030, May 2006.

[11] A. Mehari, O. Valle, and R. F. Gillum, "Trends in Pulmonary Hypertension Mortality and Morbidity," 2014.

[12] M. M. Hoeper, T. Kramer, Z. Pan, C. A. Eichstaedt, J. Spiesshoefer, N. Benjamin, K. M. Olsson, K. Meyer, C. D. Vizza, A. Vonk-Noordegraaf, O. Distler, C. Opitz, J. S. R. Gibbs, M. Delcroix, H. Ghofrani, D. Huscher, D. Pittrow, S. Rosenkranz, and E. Grünig, "Mortality in pulmonary arterial hypertension: prediction by the 2015 European pulmonary hypertension guidelines risk stratification model," *European Respiratory Journal*, vol. 50, p. 1700740, aug 2017.

[13] R. T. Zamanian, F. Haddad, R. L. Doyle, and A. B. Weinacker, "Management strategies for patients with pulmonary hypertension in the intensive care unit*," *Critical Care Medicine*, vol. 35, p. 2037, Sept. 2007.

[14] N. Galiè, M. Humbert, J.-L. Vachiery, S. Gibbs, I. Lang, A. Torbicki, G. Simonneau, A. Peacock, A. Vonk Noordegraaf, M. Beghetti, A. Ghofrani, G. Sanchez, M. Angel, G. Hansmann, W. Klepetko, P. Lancellotti, M. Matucci, T. McDonagh, L. A. Pierard, P. T. Trindade, M. Zompatori, M. Hoeper, V. Aboyans, A. Vaz Carneiro, S. Achenbach, S. Agewall, Y. Allanore, R. Asteggiano, L. P. Badano, J. A. Barberá, H. Bouvaist, H. Bueno, R. A. Byrne, S. Carerj, G. Castro, Ç. Erol, V. Falk, C. Funck-Brentano, M. Gorenflo, J. Granton, B. Iung, D. G. Kiely, P. Kirchhof, B. Kjellstrom, U. Landmesser, J. Lekakis, C. Lionis, G. Y. H. Lip, S. E. Orfanos, M. H. Park, M. F. Piepoli, P. Ponikowski, M.-P. Revel, D. Rigau, S. Rosenkranz, H. Völler, J. L. Zamorano, J. L. Zamorano, V. Aboyans, S. Achenbach, S. Agewall, L. Badimon, G. Barón-Esquivias, H. Baumgartner, J. J. Bax, H. Bueno, S. Carerj, V. Dean, Ç. Erol, D. Fitzsimons, O. Gaemperli, P. Kirchhof, P. Kolh, P. Lancellotti, G. Y. H. Lip, P. Nihoyannopoulos, M. F. Piepoli, P. Ponikowski, M. Roffi, A. Torbicki, A. Vaz Carneiro, S. Windecker, S. Myftiu, D. Bonderman, I. Firdovsi, I. Lazareva, M. De Pauw, Š. Sokolovic, V. Velchev, M. Cikeš, J. A. Moutiris, P. Jansa, J. E. Nielsen-Kudsk, L. Anton, P. Jääskeläinen, F. Bauer, A. Chukhrukidze, C. Opitz, G. Giannakoulas, K. Karlócai, H. Oddsson, S. Gaine, D. Menachemi, M. Emdin, T. Sooronbaev, T. A. Rudzitis, L. Gumbiene, F. Lebrun, J. Micallef, V. Botnaru, L. Oukerraj, A. K. Andreassen, M. Kurzyna, L. Baptista, M. J. Ribeiro, I. M. Coman, O. Moiseeva, B. S. Stefanovic, I. Šimková, G. Wikström, M. Schwerzmann, E. Srbinovska-Kostovska, V. Dijk, A. P. J, A. Mahdhaoui, C. Kaymaz, G. Coghlan, and Y. Sirenko, "2015 ESC/ERS Guidelines for the diagnosis and treatment of pulmonary hypertensionThe Joint Task Force for the Diagnosis and Treatment of Pulmonary Hypertension of the European Society of Cardiology (ESC) and the European Respiratory Society (ERS): Endorse," *European Heart Journal*, vol. 37, pp. 67–119, feb 2016.

[15] G. Simonneau, M. A. Gatzoulis, I. Adatia, D. Celermajer, C. Denton, A. Ghofrani, M. A. Gomez Sanchez, R. Krishna Kumar, M. Landzberg, R. F. Machado,

H. Olschewski, I. M. Robbins, and R. Souza, "Updated clinical classification of pulmonary hypertension," *J. Am. Coll. Cardiol.*, vol. 62, pp. D34–41, Dec. 2013.

[16] C. T.-J. Gan, S. Holverda, J. T. Marcus, W. J. Paulus, K. M. Marques, J. G. F. Bronzwaer, J. W. Twisk, A. Boonstra, P. E. Postmus, and A. Vonk-Noordegraaf, "Right Ventricular Diastolic Dysfunction and the Acute Effects of Sildenafil in Pulmonary Hypertension Patients," *Chest*, vol. 132, pp. 11–17, July 2007.

[17] B. B. Stojnic, S. J. D. Brecker, H. B. Xiao, S. M. Helmy, M. Mbaissouroum, and D. G. Gibson, "Left ventricular filling characteristics in pulmonary hypertension: a new mode of ventricular interaction," *Br Heart J*, vol. 68, pp. 16–20, July 1992.

[18] R. F. McLaughlin, W. S. Tyler, and R. O. Canada, "Subgross Pulmonary Anatomy in Various Mammals and Man," *JAMA*, vol. 175, pp. 694–697, Feb. 1961.

[19] E. R. Weibel, "Introduction," in *Morphometry of the Human Lung*, pp. 1–4, Springer, Berlin, Heidelberg, 1963.

[20] S. Singhal, R. Henderson, K. Horsfield, K. Harding, and G. Cumming, "Morphometry of the Human Pulmonary Arterial Tree," *Circulation Research*, vol. 33, pp. 190–197, Aug. 1973.

[21] A. N. Strahler, "Quantitative analysis of watershed geomorphology," *Eos Trans. AGU*, vol. 38, pp. 913–920, Dec. 1957.

[22] R. T. Yen and S. S. Sobin, "Elasticity of arterioles and venules in postmortem human lungs," *J. Appl. Physiol.*, vol. 64, pp. 611–619, Feb. 1988.

[23] W. Huang, R. T. Yen, M. McLaurine, and G. Bledsoe, "Morphometry of the human pulmonary vasculature," *Journal of Applied Physiology*, vol. 81, pp. 2123–2133, Nov. 1996.

[24] G. S. Kassab, C. A. Rider, N. J. Tang, and Y. C. Fung, "Morphometry of pig coronary arterial trees," *American Journal of Physiology-Heart and Circulatory Physiology*, vol. 265, pp. H350–H365, July 1993.

[25] G. S. Kassab, D. H. Lin, and Y. C. Fung, "Morphometry of pig coronary venous system," *Am. J. Physiol.*, vol. 267, pp. H2100–2113, Dec. 1994.

[26] R. L. Spilker, J. A. Feinstein, D. W. Parker, V. M. Reddy, and C. A. Taylor, "Morphometry-Based Impedance Boundary Conditions for Patient-Specific Modeling of Blood Flow in Pulmonary Arteries," *Ann Biomed Eng*, vol. 35, pp. 546–559, Apr. 2007.

[27] H. Tamaddon, M. Behnia, M. Behnia, and L. Kritharides, "A new approach to blood flow simulation in vascular networks," *Comput Methods Biomech Biomed Engin*, vol. 19, no. 6, pp. 673–685, 2016.

[28] M. I. Townsley, "Structure and Composition of Pulmonary Arteries, Capillaries, and Veins," *Comprehensive Physiology*, Jan. 2011.

[29] A. Hislop and L. Reid, "Normal structure and dimensions of the pulmonary arteries in the rat.," *J Anat*, vol. 125, pp. 71–83, Jan. 1978.

[30] R. S. Jaenke and A. F. Alexander, "Fine structural alterations of bovine peripheral pulmonary arteries in hypoxia-induced hypertension," *Am. J. Pathol.*, vol. 73, pp. 377–398, Nov. 1973.

[31] L. M. Reid, "Structure and Function in Pulmonary Hypertension: New Perceptions," *Chest*, vol. 89, pp. 279–288, Feb. 1986.

[32] C. S. P. Lam, B. A. Borlaug, G. C. Kane, F. T. Enders, R. J. Rodeheffer, and M. M. Redfield, "Age-Associated Increases in Pulmonary Artery Systolic Pressure in the General Population," *Circulation*, vol. 119, pp. 2663–2670, May 2009.

[33] D. Heath, J. W. DuShane, E. H. Wood, and J. E. Edwards, "The structure of the pulmonary trunk at different ages and in cases of pulmonary hypertension and pulmonary stenosis," *J. Pathol.*, vol. 77, pp. 443–456, Apr. 1959.

[34] E. H. Mackay, J. Banks, B. Sykes, and G. Lee, "Structural basis for the changing physical properties of human pulmonary vessels with age.," *Thorax*, vol. 33, pp. 335–344, June 1978.

[35] G. G. Pietra, W. D. Edwards, J. M. Kay, S. Rich, J. Kernis, B. Schloo, S. M. Ayres, E. H. Bergofsky, B. H. Brundage, and K. M. Detre, "Histopathology of primary pulmonary hypertension. A qualitative and quantitative study of pulmonary blood vessels from 58 patients in the National Heart, Lung, and Blood Institute, Primary Pulmonary Hypertension Registry.," *Circulation*, vol. 80, pp. 1198–1206, Nov. 1989.

[36] D. Heath and P. Smith, "Plexiform lesions with giant cells.," *Thorax*, vol. 37, pp. 394–5, may 1982.

[37] P. M. Hassoun, "Deciphering the "matrix" in pulmonary vascular remodelling," *European Respiratory Journal*, vol. 25, pp. 778–779, May 2005.

[38] D. Jonigk, H. Golpon, C. L. Bockmeyer, L. Maegel, M. M. Hoeper, J. Gottlieb, N. Nickel, K. Hussein, U. Maus, U. Lehmann, S. Janciauskiene, T. Welte, A. Haverich, J. Rische, H. Kreipe, and F. Laenger, "Plexiform Lesions in Pulmonary Arterial Hypertension," *Am J Pathol*, vol. 179, pp. 167–179, July 2011.

[39] J. E. Wagenseil and R. P. Mecham, "Elastin in Large Artery Stiffness and Hypertension," *J. of Cardiovasc. Trans. Res.*, vol. 5, pp. 264–273, June 2012.

[40] M. E. Blaauboer, F. R. Boeijen, C. L. Emson, S. M. Turner, B. Zandieh-Doulabi, R. Hanemaaijer, T. H. Smit, R. Stoop, and V. Everts, "Extracellular matrix proteins: a positive feedback loop in lung fibrosis?," *Matrix Biol.*, vol. 34, pp. 170–178, Feb. 2014.

[41] I. Chazova, J. E. Loyd, V. S. Zhdanov, J. H. Newman, Y. Belenkov, and B. Meyrick, "Pulmonary artery adventitial changes and venous involvement in primary pulmonary hypertension.," *Am J Pathol*, vol. 146, pp. 389–397, Feb. 1995.

[42] L. Tian, S. R. Lammers, P. H. Kao, J. A. Albietz, K. R. Stenmark, H. J. Qi, R. Shandas, and K. S. Hunter, "Impact of Residual Stretch and Remodeling on Collagen Engagement in Healthy and Pulmonary Hypertensive Calf Pulmonary Arteries at Physiological Pressures," *Annals of Biomedical Engineering*, vol. 40, pp. 1419–1433, July 2012.

[43] R. M. Tuder, J. C. Marecki, A. Richter, I. Fijalkowska, and S. Flores, "Pathology of Pulmonary Hypertension," *Clin Chest Med*, vol. 28, pp. 23–vii, Mar. 2007.

[44] L. A. Shimoda and S. S. Laurie, "Vascular Remodeling in Pulmonary Hypertension," *J Mol Med (Berl)*, vol. 91, pp. 297–309, Mar. 2013.

[45] M. Rabinovitch, C. Guignabert, M. Humbert, and M. R. Nicolls, "Inflammation and Immunity in the Pathogenesis of Pulmonary Arterial Hypertension," *Circulation Research*, vol. 115, pp. 165–175, June 2014.

[46] R. Paulin and E. D. Michelakis, "The Metabolic Theory of Pulmonary Arterial Hypertension," *Circulation Research*, vol. 115, pp. 148–164, June 2014.

[47] R. Budhiraja, R. M. Tuder, and P. M. Hassoun, "Endothelial dysfunction in pulmonary hypertension," *Circulation*, vol. 109, pp. 159–165, Jan. 2004.

[48] E. Stacher, B. B. Graham, H. J. M., A. Gandjeva, S. D. Groshong, V. V. McLaughlin, M. Jessup, G. W. E., M. A. Aldred, C. D. Cool, and R. M. Tuder, "Modern Age Pathology of Pulmonary Arterial Hypertension," *Am J Respir Crit Care Med.*, vol. 186, pp. 261–272, Jan. 2012.

[49] S. H. E. Zaidi, X.-M. You, S. Ciura, M. Husain, and M. Rabinovitch, "Overexpression of the serine elastase inhibitor elafin protects transgenic mice from hypoxic pulmonary hypertension," *Circulation*, vol. 105, pp. 516–521, Jan. 2002.

[50] S. Sakao, K. Tatsumi, and N. F. Voelkel, "Reversible or Irreversible Remodeling in Pulmonary Arterial Hypertension," *Am J Respir Cell Mol Biol*, vol. 43, pp. 629–634, Dec. 2010.

[51] K. S. Hunter, J. A. Albietz, P.-F. Lee, C. J. Lanning, S. R. Lammers, S. H. Hofmeister, P. H. Kao, H. J. Qi, K. R. Stenmark, and R. Shandas, "In vivo measurement of proximal pulmonary artery elastic modulus in the neonatal calf model of pulmonary hypertension: development and ex vivo validation," *Journal of Applied Physiology*, vol. 108, pp. 968–975, Jan. 2010.

[52] K. G. Blyth, R. Syyed, J. Chalmers, J. E. Foster, T. Saba, R. Naeije, C. Melot, and A. J. Peacock, "Pulmonary arterial pulse pressure and mortality in pulmonary arterial hypertension," *Respiratory Medicine*, vol. 101, pp. 2495–2501, dec 2007.

[53] B. Ha, C. L. Lucas, G. W. Henry, E. G. Frantz, J. I. Ferreiro, and B. R. Wilcox, "Effects of chronically elevated pulmonary arterial pressure and flow on right ventricular afterload.," *The American journal of physiology*, vol. 267, pp. H155–65, jul 1994.

[54] E. O. Attinger, "Pressure transmission in pulmonary arteries related to frequency and geometry," *Circulation research*, vol. 12, pp. 623–641, 1963.

[55] E. H. Hollander, J. J. Wang, G. M. Dobson, K. H. Parker, and J. V. Tyberg, "Negative wave reflections in pulmonary arteries.," *American journal of physiology. Heart and circulatory physiology*, vol. 281, no. 2, pp. H895–902, 2001.

[56] M. A. Quail, D. S. Knight, J. A. Steeden, L. Taelman, S. Moledina, A. M. Taylor, P. Segers, G. J. Coghlan, and V. Muthurangu, "Noninvasive pulmonary artery wave intensity analysis in pulmonary hypertension," *American Journal of Physiology-Heart and Circulatory Physiology*, vol. 308, pp. H1603–H1611, jun 2015.

[57] T. Thacher, R. F. da Silva, and N. Stergiopulos, "Differential Effects of Reduced Cyclic Stretch and Perturbed Shear Stress Within the Arterial Wall and on Smooth Muscle Function," *American Journal of Hypertension*, vol. 22, pp. 1250–1257, dec 2009.

[58] W. Durante, L. Liao, S. V. Reyna, K. J. Peyton, and A. I. Schafer, "Physiological cyclic stretch directs L-arginine transport and metabolism to collagen synthesis in vascular smooth muscle.," *FASEB journal : official publication of the Federation of American Societies for Experimental Biology*, vol. 14, pp. 1775–83, sep 2000.

[59] S. Reyna, D. Ensenat, F. K. Johnson, H. Wang, A. I. Schafer, and W. Durante, "Cyclic strain stimulates -proline transport in vascular smooth muscle cells*1," *American Journal of Hypertension*, vol. 17, pp. 712–717, aug 2004.

[60] A. M. Briones, M. Salaices, and E. Vila, "Mechanisms underlying hypertrophic remodeling and increased stiffness of mesenteric resistance arteries from aged rats.," *The journals of gerontology. Series A, Biological sciences and medical sciences*, vol. 62, pp. 696–706, jul 2007.

[61] P. F. Davies, "Flow-mediated endothelial mechanotransduction.," *Physiological reviews*, vol. 75, pp. 519–60, jul 1995.

[62] P. Lacolley, "Mechanical influence of cyclic stretch on vascular endothelial cells," *Cardiovascular Research*, vol. 63, pp. 577–579, sep 2004.

[63] D. Scott, Y. Tan, R. Shandas, K. R. Stenmark, and W. Tan, "High pulsatility flow stimulates smooth muscle cell hypertrophy and contractile protein expression.," *American journal of physiology. Lung cellular and molecular physiology*, vol. 304, pp. L70–81, jan 2013.

[64] J. D. Humphrey, "Mechanisms of Arterial Remodeling in Hypertension," *Hypertension*, vol. 52, pp. 195–200, aug 2008.

[65] J. Blacher and M. E. Safar, "Large-artery stiffness, hypertension and cardiovascular risk in older patients," *Nature Clinical Practice Cardiovascular Medicine*, vol. 2, pp. 450–455, sep 2005.

[66] S. Laurent, A.-I. Tropeano, and P. Boutouyrie, "Pulse pressure reduction and cardiovascular protection," *Journal of Hypertension*, vol. 24, pp. S13–S18, may 2006.

[67] B. A. Zambrano, N. A. McLean, X. Zhao, J.-L. Tan, L. Zhong, C. A. Figueroa, L. C. Lee, and S. Baek, "Image-based computational assessment of vascular wall mechanics and hemodynamics in pulmonary arterial hypertension patients," *Journal of Biomechanics*, vol. 68, pp. 84–92, Feb. 2018.

[68] K. S. Burrowes, P. J. Hunter, M. H. Tawhai, and S. Kelly, "Anatomically based finite element models of the human pulmonary arterial and venous trees including supernumerary vessels," *Journal of applied physiology*, vol. 99, no. 2, pp. 731–738, 2005.

[69] M. S. Olufsen, C. S. Peskin, W. Y. Kim, E. M. Pedersen, A. Nadim, and J. Larsen, "Numerical Simulation and Experimental Validation of Blood Flow in Arteries with Structured-Tree Outflow Conditions," *Annals of Biomedical Engineering*, vol. 28, pp. 1281–1299, Nov. 2000.

[70] Y. Huo and G. S. Kassab, "Pulsatile blood flow in the entire coronary arterial tree: theory and experiment," *American Journal of Physiology. Heart and Circulatory Physiology*, vol. 291, no. 3, pp. H1074–1087, 2006.

[71] J. P. Mynard, D. J. Penny, and J. J. Smolich, "Scalability and in vivo validation of a multiscale numerical model of the left coronary circulation," *American Journal of Physiology-Heart and Circulatory Physiology*, vol. 306, pp. H517–H528, feb 2014.

[72] J. Alastruey, K. H. Parker, J. Peiró, S. M. Byrd, and S. J. Sherwin, "Modelling the circle of Willis to assess the effects of anatomical variations and occlusions on cerebral flows," *Journal of Biomechanics*, vol. 40, no. 8, pp. 1794–1805, 2007.

[73] M. S. Olufsen, N. A. Hill, G. D. A. Vaughan, C. Sainsbury, and M. Johnson, "Rarefaction and blood pressure in systemic and pulmonary arteries," *J Fluid Mech*, vol. 705, pp. 280–305, Aug. 2012.

[74] M. U. Qureshi, G. D. A. Vaughan, C. Sainsbury, M. Johnson, C. S. Peskin, M. S. Olufsen, and N. A. Hill, "Numerical simulation of blood flow and pressure drop in the pulmonary arterial and venous circulation," *Biomech Model Mechanobiol*, vol. 13, pp. 1137–1154, Oct. 2014.

[75] M. U. Qureshi, M. J. Colebank, L. M. Paun, L. Ellwein Fix, N. Chesler, M. A. Haider, N. A. Hill, D. Husmeier, and M. S. Olufsen, "Hemodynamic assessment of pulmonary hypertension in mice: a model-based analysis of the disease mechanism," *Biomechanics and Modeling in Mechanobiology*, vol. 18, pp. 219–243, feb 2019.

[76] B. Mandelbrot, *Fractals and the Geometry of Nature*. New York: W.H. Freeman, 1983.

[77] Centers of Disease Control and Prevention, "Underlying Cause of Death, 1999-2017," 2019. [Online]. Available: `https://wonder.cdc.gov/ucd-icd10.html`.

[78] J. D. Sara, R. J. Widmer, Y. Matsuzawa, R. J. Lennon, L. O. Lerman, and A. Lerman, "Prevalence of Coronary Microvascular Dysfunction Among Patients With Chest Pain and Nonobstructive Coronary Artery Disease," *JACC: Cardiovascular Interventions*, vol. 8, pp. 1445–1453, sep 2015.

[79] L. Jespersen, A. Hvelplund, S. Z. Abildstrom, F. Pedersen, S. Galatius, J. K. Madsen, E. Jorgensen, H. Kelbaek, and E. Prescott, "Stable angina pectoris with no obstructive coronary artery disease is associated with increased risks of major adverse cardiovascular events," *European Heart Journal*, vol. 33, pp. 734–744, mar 2012.

[80] S. Vijayan, D. S. Barmby, I. R. Pearson, A. G. Davies, S. B. Wheatcroft, and M. Sivananthan, "Assessing Coronary Blood Flow Physiology in the Cardiac Catheterisation Laboratory.," *Current cardiology reviews*, vol. 13, no. 3, pp. 232–243, 2017.

[81] C. Zhang, P. A Rogers, D. Merkus, J. M Muller-Delp, C. P Tiefenbacher, B. Potter, J. D Knudson, P. Rocic, and W. M Chilian, "Regulation of Coronary Microvascular Resistance in Health and Disease," *Microcirculation*, pp. 521–549, jan 2008.

[82] J. D. Tune, "Coronary Circulation," *Colloquium Series on Integrated Systems Physiology: From Molecule to Function*, vol. 6, pp. 1–189, jul 2014.

[83] I. Ogobuiro and F. Tuma, *Anatomy, Thorax, Heart Coronary Arteries*. StatPearls Publishing, dec 2019.

[84] M. D. Cerqueira, N. J. Weissman, V. Dilsizian, A. K. Jacobs, S. Kaul, W. K. Laskey, D. J. Pennell, J. A. Rumberger, T. Ryan, M. S. Verani, and M. S. Verani, "Standardized Myocardial Segmentation and Nomenclature for Tomographic Imaging of the Heart," *Circulation*, vol. 105, pp. 539–542, jan 2002.

[85] G. S. Kassab and Y. C. Fung, "The pattern of coronary arteriolar bifurcations and the uniform shear hypothesis," *Ann Biomed Eng*, vol. 23, pp. 13–20, Feb. 1995.

[86] N. Mittal, Y. Zhou, S. Ung, C. Linares, S. Molloi, and G. S. Kassab, "A Computer Reconstruction of the Entire Coronary Arterial Tree Based on Detailed Morphometric Data," *Annals of Biomedical Engineering*, vol. 33, pp. 1015–1026, aug 2005.

[87] Y. Zhou, G. S. Kassab, and S. Molloi, "On the design of the coronary arterial tree: a generalization of Murray's law," *Phys. Med. Biol.*, vol. 44, no. 12, p. 2929, 1999.

[88] D. Algranati, G. S. Kassab, and Y. Lanir, "Mechanisms of myocardium-coronary vessel interaction," *American Journal of Physiology-Heart and Circulatory Physiology*, vol. 298, pp. H861–H873, mar 2010.

[89] J. Dankelman, I. Vergroesen, Y. Han, and J. A. Spaan, "Dynamic response of coronary regulation to heart rate and perfusion changes in dogs.," *The American journal of physiology*, vol. 263, pp. H447–52, aug 1992.

[90] H. Chen and G. S. Kassab, "Microstructure-based biomechanics of coronary arteries in health and disease," *Journal of Biomechanics*, vol. 49, pp. 2548–2559, aug 2016.

[91] H. Chen, Y. Liu, M. Slipchenko, X. Zhao, J.-X. Cheng, and G. Kassab, "The Layered Structure of Coronary Adventitia under Mechanical Load," *Biophysical Journal*, vol. 101, pp. 2555–2562, dec 2011.

[92] A. Zoumi, X. Lu, G. S. Kassab, and B. J. Tromberg, "Imaging Coronary Artery Microstructure Using Second-Harmonic and Two-Photon Fluorescence Microscopy," *Biophysical Journal*, vol. 87, pp. 2778–2786, oct 2004.

[93] H. Chen, T. Luo, X. Zhao, X. Lu, Y. Huo, and G. S. Kassab, "Microstructural constitutive model of active coronary media," *Biomaterials*, vol. 34, pp. 7575–7583, oct 2013.

[94] G. A. Holzapfel, G. Sommer, C. T. Gasser, and P. Regitnig, "Determination of layer-specific mechanical properties of human coronary arteries with nonatherosclerotic intimal thickening and related constitutive modeling Determination of layer-specific mechanical prop-erties of human coronary arteries with nonatherosclerotic intimal thickening and related constitutive modeling," *Am J Physiol Heart Circ Physiol*, vol. 289, pp. 2048–2058, 2005.

[95] T. P. van de Hoef, M. Echavarría-Pinto, J. Escaned, and J. J. Piek, "Coronary flow capacity: concept, promises, and challenges.," *The international journal of cardiovascular imaging*, vol. 33, pp. 1033–1039, jul 2017.

[96] S.-Y. Park, J. R. Gifford, R. H. I. Andtbacka, J. D. Trinity, J. R. Hyngstrom, R. S. Garten, N. A. Diakos, S. J. Ives, F. Dela, S. Larsen, S. Drakos, and R. S. Richardson, "Cardiac, skeletal, and smooth muscle mitochondrial respiration: are all mitochondria created equal?," *American journal of physiology. Heart and circulatory physiology*, vol. 307, pp. H346–52, aug 2014.

[97] D. J. Duncker and R. J. Bache, "Regulation of Coronary Blood Flow During Exercise," *Physiological Reviews*, vol. 88, pp. 1009–1086, jul 2008.

[98] P. A. Murray and S. F. Vatner, "alpha-Adrenoceptor attenuation of the coronary vascular response to severe exercise in the conscious dog.," *Circulation Research*, vol. 45, pp. 654–660, nov 1979.

[99] R. K. Pradhan, E. O. Feigl, M. W. Gorman, G. L. Brengelmann, and D. A. Beard, "Open-loop (feed-forward) and feedback control of coronary blood flow during exercise, cardiac pacing, and pressure changes," *American Journal of Physiology-Heart and Circulatory Physiology*, vol. 310, pp. H1683–H1694, jun 2016.

[100] B. J. Hart, X. Bian, P. A. Gwirtz, S. Setty, and H. F. Downey, "Right ventricular oxygen supply/demand balance in exercising dogs," *American Journal of Physiology-Heart and Circulatory Physiology*, vol. 281, pp. H823–H830, aug 2001.

[101] M. W. Gorman, G. A. Rooke, M. V. Savage, M. P. S. Jayasekara, K. A. Jacobson, and E. O. Feigl, "Adenine nucleotide control of coronary blood flow during exercise," *American Journal of Physiology-Heart and Circulatory Physiology*, vol. 299, pp. H1981–H1989, dec 2010.

[102] J. C. Liao and L. Kuo, "Interaction between adenosine and flow-induced dilation in coronary microvascular network.," *The American journal of physiology*, vol. 272, pp. H1571–81, apr 1997.

[103] G. M. Dick, R. Namani, B. Patel, and G. S. Kassab, "Role of Coronary Myogenic Response in Pressure-Flow Autoregulation in Swine: A Meta-Analysis With Coronary Flow Modeling," *Frontiers in Physiology*, vol. 9, p. 580, may 2018.

[104] D. V. DeFily and W. M. Chilian, "Coronary microcirculation: autoregulation and metabolic control," *Basic Research in Cardiology*, vol. 90, no. 2, pp. 112–118, 1995.

[105] D. J. Duncker, R. Stubenitsky, and P. D. Verdouw, "Autonomic control of vasomotion in the porcine coronary circulation during treadmill exercise: evidence for feed-forward beta-adrenergic control.," *Circulation research*, vol. 82, pp. 1312–22, jun 1998.

[106] G. Heusch, "The paradox of α-adrenergic coronary vasoconstriction revisited," *Journal of Molecular and Cellular Cardiology*, vol. 51, pp. 16–23, jul 2011.

[107] M. Farias, M. W. Gorman, M. V. Savage, and E. O. Feigl, "Plasma ATP during exercise: possible role in regulation of coronary blood flow," *American Journal of Physiology-Heart and Circulatory Physiology*, vol. 288, pp. H1586–H1590, apr 2005.

[108] M. J. Davis, M. A. Hill, and L. Kuo, "Local Regulation of Microvascular Perfusion," *Microcirculation*, pp. 161–284, jan 2008.

[109] B. E. Carlson, J. C. Arciero, and T. W. Secomb, "Theoretical model of blood flow autoregulation: roles of myogenic, shear-dependent, and metabolic responses," *American Journal of Physiology-Heart and Circulatory Physiology*, vol. 295, pp. H1572–H1579, oct 2008.

[110] T. V. Murphy, B. E. Spurrell, and M. A. Hill, "Cellular signalling in arteriolar myogenic constriction: involvement of tyrosine phosphorylation pathways.," *Clinical and experimental pharmacology & physiology*, vol. 29, pp. 612–9, jul 2002.

[111] A. H. Amin, Z. Y. Abd Elmageed, M. Partyka, and K. Matrougui, "Mechanisms of myogenic tone of coronary arteriole: Role of down stream signaling of the EGFR tyrosine kinase," *Microvascular Research*, vol. 81, pp. 135–142, jan 2011.

[112] L. A. Martinez-Lemus, "The dynamic structure of arterioles.," *Basic & clinical pharmacology & toxicology*, vol. 110, pp. 5–11, jan 2012.

[113] L. Kuo, M. J. Davis, and W. M. Chilian, "Myogenic activity in isolated subepicardial and subendocardial coronary arterioles.," *The American journal of physiology*, vol. 255, pp. H1558–62, dec 1988.

[114] H. Kanatsuka, K. G. Lamping, C. L. Eastham, and M. L. Marcus, "Heterogeneous changes in epimyocardial microvascular size during graded coronary stenosis. Evidence of the microvascular site for autoregulation.," *Circulation research*, vol. 66, pp. 389–96, feb 1990.

[115] D. J. Duncker, A. Koller, D. Merkus, and J. M. Canty, "Regulation of Coronary Blood Flow in Health and Ischemic Heart Disease," *Progress in Cardiovascular Diseases*, vol. 57, pp. 409–422, mar 2015.

[116] R. Namani, G. S. Kassab, and Y. Lanir, "Integrative model of coronary flow in anatomically based vasculature under myogenic, shear, and metabolic regulation," *The Journal of General Physiology*, vol. 150, pp. 145–168, jan 2018.

[117] L. Kuo, M. J. Davis, and W. M. Chilian, "Longitudinal Gradients for Endothelium-Dependent and -Independent Vascular Responses in the Coronary Microcirculation," *Circulation*, vol. 92, pp. 518–525, aug 1995.

[118] D. W. Stepp, Y. Nishikawa, and W. M. Chilian, "Regulation of Shear Stress in the Canine Coronary Microcirculation," tech. rep., 1999.

[119] M. H. Laughlin, S. C. Newcomer, and S. B. Bender, "Importance of hemodynamic forces as signals for exercise-induced changes in endothelial cell phenotype.," *Journal of applied physiology (Bethesda, Md. : 1985)*, vol. 104, pp. 588–600, mar 2008.

[120] M. H. Laughlin, D. K. Bowles, and D. J. Duncker, "The coronary circulation in exercise training," *American Journal of Physiology-Heart and Circulatory Physiology*, vol. 302, pp. H10–H23, jan 2012.

[121] D. A. Beard and J. B. Bassingthwaighte, "The Fractal Nature of Myocardial Blood Flow Emerges from a Whole-Organ Model of Arterial Network," *Journal of Vascular Research*, vol. 37, no. 4, pp. 282–296, 2000.

[122] N. P. Smith, A. J. Pullan, and P. J. Hunter, "Generation of an Anatomically Based Geometric Coronary Model," *Annals of Biomedical Engineering*, vol. 28, pp. 14–25, jan 2000.

[123] M. Zamir, "The role of shear forces in arterial branching.," *The Journal of General Physiology*, vol. 67, pp. 213–222, Feb. 1976.

[124] R. Karch, F. Neumann, M. Neumann, and W. Schreiner, "Staged Growth of Optimized Arterial Model Trees," *Annals of Biomedical Engineering*, vol. 28, pp. 495–511, may 2000.

[125] C. Jaquet, L. Najman, H. Talbot, L. Grady, M. Schaap, B. Spain, H. J. Kim, I. Vignon-Clementel, and C. A. Taylor, "Generation of Patient-Specific Cardiac Vascular Networks: A Hybrid Image-Based and Synthetic Geometric Model," *IEEE Transactions on Biomedical Engineering*, vol. 66, pp. 946–955, apr 2019.

[126] B. Kaimovitz, Y. Lanir, and G. S. Kassab, "Large-Scale 3-D Geometric Reconstruction of the Porcine Coronary Arterial Vasculature Based on Detailed Anatomical Data," *Annals of Biomedical Engineering*, vol. 33, pp. 1517–1535, nov 2005.

[127] B. Kaimovitz, Y. Lanir, and G. S. Kassab, "A full 3-D reconstruction of the entire porcine coronary vasculature," *American Journal of Physiology-Heart and Circulatory Physiology*, vol. 299, pp. H1064–H1076, oct 2010.

[128] R. Namani, G. S. Kassab, and Y. Lanir, "Morphometric Reconstruction of Coronary Vasculature Incorporating Uniformity of Flow Dispersion," *Frontiers in Physiology*, vol. 9, p. 1069, aug 2018.

[129] A. C. Guyton, T. G. Coleman, and H. J. Granger, "Circulation: Overall Regulation," *Annual Review of Physiology*, vol. 34, pp. 13–44, mar 1972.

[130] A. C. Guyton, T. G. Coleman, A. W. Cowley, K. W. Scheel, R. Manning, and R. A. Norman, "Arterial pressure regulation," *The American Journal of Medicine*, vol. 52, pp. 584–594, may 1972.

[131] A. C. Guyton, T. G. Coleman, A. W. Cowley, J.-F. Liard, R. A. Norman, and R. D. Manning, "Systems analysis of arterial pressure regulation and hypertension," *Annals of Biomedical Engineering*, vol. 1, pp. 254–281, dec 1972.

[132] J. C. Arciero, B. E. Carlson, and T. W. Secomb, "Theoretical model of metabolic blood flow regulation: roles of ATP release by red blood cells and conducted responses," *American Journal of Physiology-Heart and Circulatory Physiology*, vol. 295, pp. H1562–H1571, oct 2008.

[133] J. I. Hoffman and J. A. Spaan, "Pressure-flow relations in coronary circulation," *Physiological Reviews*, vol. 70, pp. 331–390, apr 1990.

[134] B. Teng, S. L. Tilley, C. Ledent, and S. J. Mustafa, "In vivo assessment of coronary flow and cardiac function after bolus adenosine injection in adenosine receptor knockout mice.," *Physiological reports*, vol. 4, jun 2016.

[135] A. J. M. Cornelissen, J. Dankelman, E. VanBavel, and J. A. E. Spaan, "Balance between myogenic, flow-dependent, and metabolic flow control in coronary arterial tree: a model study," *American Journal of Physiology-Heart and Circulatory Physiology*, vol. 282, pp. H2224–H2237, jun 2002.

[136] R. Skalak, "Growth as A Finite Displacement Field," in *Proceedings of the IUTAM Symposium on Finite Elasticity*, pp. 347–355, Springer, Dordrecht, 1981.

[137] R. Skalak, G. Dasgupta, M. Moss, E. Otten, P. Dullemeijer, and H. Vilmann, "Analytical description of growth," *Journal of Theoretical Biology*, vol. 94, pp. 555–577, Feb. 1982.

[138] S. Baek, K. R. Rajagopal, and J. D. Humphrey, "A Theoretical Model of Enlarging Intracranial Fusiform Aneurysms," *J Biomech Eng*, vol. 128, pp. 142–149, Sept. 2005.

[139] A. Valentín, L. Cardamone, S. Baek, and J. D. Humphrey, "Complementary vasoactivity and matrix remodelling in arterial adaptations to altered flow and pressure," *Journal of The Royal Society Interface*, vol. 6, pp. 293–306, Mar. 2009.

[140] S. Zeinali-Davarani, A. Sheidaei, and S. Baek, "A finite element model of stress-mediated vascular adaptation: application to abdominal aortic aneurysms," *Computer Methods in Biomechanics and Biomedical Engineering*, vol. 14, pp. 803–817, Sept. 2011.

[141] M. Farsad, S. Zeinali-Davarani, J. Choi, and S. Baek, "Computational Growth and Remodeling of Abdominal Aortic Aneurysms Constrained by the Spine," *J Biomech Eng*, vol. 137, pp. 091008–091008–12, July 2015.

[142] J. D. Humphrey, S. Baek, and L. E. Niklason, "Biochemomechanics of Cerebral Vasospasm and its Resolution: I. A New Hypothesis and Theoretical Framework," *Ann Biomed Eng*, vol. 35, pp. 1485–1497, Sept. 2007.

[143] A. Sheidaei, S. C. Hunley, S. Zeinali-Davarani, L. G. Raguin, and S. Baek, "Simulation of abdominal aortic aneurysm growth with updating hemodynamic loads using a realistic geometry," *Medical Engineering & Physics*, vol. 33, pp. 80–88, Jan. 2011.

[144] X. Guo and G. S. Kassab, "Distribution of stress and strain along the porcine aorta and coronary arterial tree," *American Journal of Physiology-Heart and Circulatory Physiology*, vol. 286, pp. H2361–H2368, jun 2004.

[145] J. S. Choy and G. S. Kassab, "Wall thickness of coronary vessels varies transmurally in the LV but not the RV: implications for local stress distribution," *American Journal of Physiology-Heart and Circulatory Physiology*, vol. 297, pp. H750–H758, aug 2009.

[146] A. R. Pries, B. Reglin, and T. W. Secomb, "Structural adaptation of vascular networks: role of the pressure response.," *Hypertension (Dallas, Tex. : 1979)*, vol. 38, pp. 1476–9, dec 2001.

[147] Y. Liu and G. S. Kassab, "Vascular metabolic dissipation in Murray's law," *Am. J. Physiol. Heart Circ. Physiol.*, vol. 292, pp. H1336–1339, Mar. 2007.

[148] A. Kamiya, R. Bukhari, and T. Togawa, "Adaptive regulation of wall shear stress optimizing vascular tree function," *Bulletin of Mathematical Biology*, vol. 46, pp. 127–137, jan 1984.

[149] A. R. Pries, T. W. Secomb, T. Gessner, M. B. Sperandio, J. F. Gross, and P. Gaehtgens, "Resistance to blood flow in microvessels in vivo.," *Circulation Research*, vol. 75, pp. 904–915, nov 1994.

[150] A. Klarbring, J. Petersson, B. Torstenfelt, and M. Karlsson, "Topology optimization of flow networks," *Computer Methods in Applied Mechanics and Engineering*, vol. 192, pp. 3909–3932, jul 2003.

[151] G. S. Kassab, "Scaling laws of vascular trees: of form and function," *American Journal of Physiology-Heart and Circulatory Physiology*, vol. 290, pp. H894–H903, feb 2006.

[152] L. A. Taber, "An optimization principle for vascular radius including the effects of smooth muscle tone.," *Biophys J*, vol. 74, pp. 109–114, Jan. 1998.

[153] S. B. Lindström, G. Satha, and A. Klarbring, "Extension of Murray's law including nonlinear mechanics of a composite artery wall," *Biomech Model Mechanobiol*, vol. 14, pp. 83–91, Jan. 2015.

[154] A. R. Pries, B. Reglin, and T. W. Secomb, "Remodeling of Blood Vessels," *Hypertension*, vol. 46, pp. 725–731, oct 2005.

[155] G. S. Kassab, "Mechanical Homeostasis of Cardiovascular Tissue," in *Bioengineering in Cell and Tissue Research*, pp. 371–391, Berlin, Heidelberg: Springer Berlin Heidelberg, 2008.

[156] M. Zamir, "On Fractal Properties of Arterial Trees," *Journal of Theoretical Biology*, vol. 197, pp. 517–526, apr 1999.

[157] S. Baek, K. Rajagopal, and J. Humphrey, "A theoretical model of enlarging intracranial fusiform aneurysms," *ASME Journal of Biomedical Engineering*, vol. 128, pp. 142–149, 2006.

[158] J. D. Humphrey, *Cardiovascular Solid Mechanics: Cells, Tissues, and Organs*. New York: Springer-Verlag, 2002.

[159] S. Baek, K. R. Rajagopal, and J. D. Humphrey, "Competition between radial expansion and thickening in the enlargement of an intracranial saccular aneurysm," *Journal of Elasticity*, vol. 80, pp. 13–31, 2005.

[160] S. Baek, R. L. Gleason, K. R. Rajagopal, and J. D. Humphrey, "Theory of small on large: Potential utility in computations of fluid-solid interactions in arteries," *Computer Methods in Applied Mechanics and Engineering*, vol. 196, pp. 3070–3078, 2007.

[161] M. Li, D. E. Scott, R. Shandas, K. R. Stenmark, and W. Tan, "High Pulsatility Flow Induces Adhesion Molecule and Cytokine mRNA Expression in Distal Pulmonary Artery Endothelial Cells," *Annals of Biomedical Engineering*, vol. 37, pp. 1082–1092, jun 2009.

[162] F. N. van de Vosse and N. Stergiopulos, "Pulse Wave Propagation in the Arterial Tree," *Annual Review of Fluid Mechanics*, vol. 43, no. 1, pp. 467–499, 2011.

[163] M. G. Taylor, "An approach to an analysis of the Arterial Pulse Wave I. Oscillations in an Attenuating Line," *Phys. Med. Biol.*, vol. 1, no. 3, pp. 258–269, 1957.

[164] A. Avolio, "Multi-branched model of the human arterial system," *Medical and Biological Engineering and Computing*, vol. 18, no. 6, pp. 709–718, 1980.

[165] W. W. Nichols, M. F. O'Rourke, and C. Vlachopoulos, *McDonald's Blood Flow in Arteries: Theoretical, Experimental and Clinical Principles*. Hodder Arnold, sixth ed., 2011.

[166] R. Paul, "Chemical energetics of vascular smooth muscle," *Comprehensive Physiology*, vol. 2007, pp. 1–16, 1980.

[167] R. J. Paul, "Coordination of metabolism and contractility in vascular smooth muscle.," *Federation proceedings*, vol. 42, pp. 62–6, jan 1983.

[168] D. Liu, N. B. Wood, N. Witt, A. D. Hughes, S. A. Thom, and X. Y. Xu, "Assessment of Energy Requirement for the Retinal Arterial Network in Normal and Hypertensive Subjects," *Journal of Biomechanical Engineering*, vol. 134, pp. 14501–14507, apr 2012.

[169] S. Baek, A. Rao, Y. Wang, L. Alison, and S. Roccabianca, "Pressure induced damage of pulmonary artery," (Tucson, AZ), Summer Biomechanics, Bioengineering and Biotransport Conference (SB3C), 2017.

[170] N. Li, S. Zhang, J. Hou, I.-K. Jang, and B. Yu, "Assessment of Pulmonary Artery Morphology by Optical Coherence Tomography," *Heart, Lung and Circulation*, vol. 21, pp. 778–781, dec 2012.

[171] N. Rol, E. M. Timmer, T. J. Faes, A. Vonk Noordegraaf, K. Grünberg, H.-J. Bogaard, and N. Westerhof, "Vascular narrowing in pulmonary arterial hypertension is heterogeneous: rethinking resistance," *Physiological Reports*, vol. 5, p. e13159, mar 2017.

[172] F. Elliott and L. Reid, "Some new facts about the pulmonary artery and its branching pattern," *Clinical Radiology*, vol. 16, pp. 193–198, jan 1965.

[173] M. Zamir, "The role of shear forces in arterial branching.," *The Journal of General Physiology*, vol. 67, pp. 213–222, apr 1976.

[174] A. R. Pries, T. W. Secomb, and P. Gaehtgens, "Biophysical aspects of blood flow in the microvasculature.," *Cardiovascular research*, vol. 32, pp. 654–67, oct 1996.

[175] M. Bernal, M. W. Urban, D. Rosario, W. Aquino, and J. F. Greenleaf, "Measurement of biaxial mechanical properties of soft tubes and arteries using piezoelectric elements and sonometry," *Physics in Medicine and Biology*, vol. 56, pp. 3371–3386, jun 2011.

[176] R. Yen, D. Tai, Z. Rong, and B. Zhang, "Elasticity of Pulmonary Blood Vessels in Human Lungs," in *Respiratory Biomechanics: Engineering Analysis of Structure and Function* (M. A. Epstein and J. R. Ligas, eds.), Springer-Verlag New York, 1990.

[177] G. S. Krenz and C. A. Dawson, "Flow and pressure distributions in vascular networks consisting of distensible vessels," *American Journal of Physiology-Heart and Circulatory Physiology*, vol. 284, pp. H2192–H2203, June 2003.

[178] J. Banks, F. V. Booth, E. H. MacKay, B. Rajagopalan, and G. D. Lee, "The physcial properties of human pulmonary arteries and veins," *Clinical Science and Molecular Medicine*, vol. 55, no. 5, pp. 477–484, 1978.

[179] W. R. Milnor, C. R. Conti, K. B. Lewis, and M. F. O'Rourke, "Pulmonary Arterial Pulse Wave Velocity and Impedance in Man," *Circulation research*, vol. 25, no. 6, pp. 637–649, 1969.

[180] C. Jaquet, L. Najman, H. Talbot, L. J. Grady, M. Schaap, B. Spain, H. J. Kim, I. Vignon-Clementel, and C. A. Taylor, "Generation of patient-specific cardiac vascular networks: a hybrid image-based and synthetic geometric model," *IEEE Transactions on Biomedical Engineering*, pp. 1–1, aug 2018.

[181] A. R. Pries and T. W. Secomb, "Microvascular blood viscosity in vivo and the endothelial surface layer," *American Journal of Physiology-Heart and Circulatory Physiology*, vol. 289, pp. H2657–H2664, dec 2005.

[182] T. Arts and R. S. Reneman, "Interaction Between Intramyocardial Pressure (IMP) and Myocardial Circulation," *Journal of Biomechanical Engineering*, vol. 107, p. 51, feb 1985.

[183] E. S. Kirk and C. R. Honig, "An experimental and theoretical analysis of myocardial tissue pressure," *American Journal of Physiology-Legacy Content*, vol. 207, pp. 361–367, aug 1964.

[184] A. G. Goodwill, G. M. Dick, A. M. Kiel, and J. D. Tune, "Regulation of Coronary Blood Flow," in *Comprehensive Physiology*, vol. 7, pp. 321–382, Hoboken, NJ, USA: John Wiley & Sons, Inc., mar 2017.

[185] L. A. Martinez-Lemus, X. Wu, E. Wilson, M. A. Hill, G. E. Davis, M. J. Davis, and G. A. Meininger, "Integrins as Unique Receptors for Vascular Control," *Journal of Vascular Research*, vol. 40, no. 3, pp. 211–233, 2003.

[186] A. R. Pries, T. W. Secomb, and P. Gaehtgens, "Design Principles of Vascular Beds," *Circulation Research*, vol. 77, pp. 1017–1023, nov 1995.

[187] H. Tillmanns, S. Ikeda, H. Hansen, J. S. Sarma, J. M. Fauvel, and R. J. Bing, "Microcirculation in the ventricle of the dog and turtle.," *Circulation research*, vol. 34, pp. 561–9, apr 1974.

[188] J. A. Rhodin, "The ultrastructure of mammalian arterioles and precapillary sphincters," *Journal of Ultrastructure Research*, vol. 18, pp. 181–223, apr 1967.

[189] H. N. Mayrovitz and J. Roy, "Microvascular blood flow: evidence indicating a cubic dependence on arteriolar diameter," *American Journal of Physiology-Heart and Circulatory Physiology*, vol. 245, pp. H1031–H1038, dec 1983.

[190] N. Suwa, T. Niwa, H. Fukasawa, and Y. Sasaki, "Estimation of Intravascular Blood Pressure Gradient by Mathematical Analysis of Arterial Casts," *The Tohoku Journal of Experimental Medicine*, vol. 79, pp. 168–198, mar 1963.

[191] E. VanBavel and J. A. Spaan, "Branching patterns in the porcine coronary arterial tree. Estimation of flow heterogeneity.," *Circulation research*, vol. 71, pp. 1200–12, nov 1992.

[192] K. Fronek and B. Zweifach, "Microvascular pressure distribution in skeletal muscle and the effect of vasodilation," *American Journal of Physiology-Legacy Content*, vol. 228, pp. 791–796, mar 1975.

[193] D. Richardson and B. Zweifach, "Pressure relationships in the macro- and microcirculation of the mesentery," *Microvascular Research*, vol. 2, pp. 474–488, oct 1970.

[194] G. S. Kassab and Y.-C. B. Fung, "The pattern of coronary arteriolar bifurcations and the uniform shear hypothesis," *Annals of Biomedical Engineering*, vol. 23, pp. 13–20, jan 1995.

[195] G. A. Meininger, C. A. Mack, K. L. Fehr, and H. G. Bohlen, "Myogenic vasoregulation overrides local metabolic control in resting rat skeletal muscle.," *Circulation research*, vol. 60, pp. 861–70, jun 1987.

[196] P. S. Clifford, "Local control of blood flow," *Advances in Physiology Education*, vol. 35, pp. 5–15, mar 2011.

[197] J. M. Canty, "Coronary pressure-function and steady-state pressure-flow relations during autoregulation in the unanesthetized dog.," *Circulation Research*, vol. 63, pp. 821–836, oct 1988.

[198] R. M. Ball and R. J. Bache, "Distribution of myocardial blood flow in the exercising dog with restricted coronary artery inflow.," *Circulation research*, vol. 38, pp. 60–6, feb 1976.

[199] C. J. H. Jones, L. Kuo, M. J. Davis, D. V. DeFily, and W. M. Chilian, "Role of Nitric Oxide in the Coronary Microvascular Responses to Adenosine and Increased Metabolic Demand," *Circulation*, vol. 91, pp. 1807–1813, mar 1995.

[200] J. M. Young, J. S. Choy, G. S. Kassab, and Y. Lanir, "Slackness between vessel and myocardium is necessary for coronary flow reserve," *American Journal of Physiology-Heart and Circulatory Physiology*, vol. 302, pp. H2230–H2242, jun 2012.

[201] S. H. Abman, "Inhaled nitric oxide for the treatment of pulmonary arterial hypertension," *Handb Exp Pharmacol*, vol. 218, pp. 257–276, 2013.

[202] N. P. Nickel, E. Spiekerkoetter, M. Gu, C. G. Li, H. Li, M. Kaschwich, I. Diebold, J. K. Hennigs, K.-Y. Kim, K. Miyagawa, L. Wang, A. Cao, S. Sa, X. Jiang, R. W. Stockstill, M. R. Nicolls, R. T. Zamanian, R. D. Bland, and M. Rabinovitch, "Elafin Reverses Pulmonary Hypertension via Caveolin-1–Dependent Bone Morphogenetic Protein Signaling," *Am J Respir Crit Care Med*, vol. 191, pp. 1273–1286, Apr. 2015.

[203] A. E. Green, R. S. Rivlin, and R. T. Shield, "General theory of small elastic deformations superposed on finite elastic deformations," *Proceedings of the Royal Society A*, vol. 211, pp. 128–154, 1952.

[204] M. A. Biot, "General theory of three-dimensional consolidation," *Journal of Applied Physics*, vol. 12, pp. 155–164, 1941.

[205] C. Truesdell and W. Noll, "Non-linear field theories of mechanics," *Handbuch des Physik, Springer, Berlin*, pp. 537–541, 1965.

[206] S. Baek and A. R. Srinivasa, "Thermomechanical constraints and constitutive formulations in thermoelasticity," 2003.

[207] M. Destrade, P. A. Martin, and T. C. T. Ting, "The incompressible limit in linear anisotropic elasticity, with applications to surface waves and elastostatics," *Journal of the Mechanics and Physics of Solids*, vol. 50, pp. 1453–1468, July 2002.

[208] J. R. Womersley, *An elastic tube theory of pulse transmission and oscillatory flow in mammalian arteries*. Wright Air Development Center, 1957.

[209] B. Kelly and P. Chowienczyk, *in: An Introduction to Vascular Biology: From Basic Science to Clinical Practice*. Cambridge University Press, 2 ed., 2002.

[210] J. Womersley, "Oscillatory motion of a viscous liquid in a thin-walled elastic tube—I: The linear approximation for long waves," *The London, Edinburgh, and Dublin Philosophical Magazine and Journal of Science*, vol. 46, no. 373, pp. 199–221, 1955.

[211] I. E. Vignon-Clementel, C. Alberto Figueroa, K. E. Jansen, and C. A. Taylor, "Outflow boundary conditions for three-dimensional finite element modeling of blood flow and pressure in arteries," *Computer Methods in Applied Mechanics and Engineering*, vol. 195, pp. 3776–3796, jun 2006.